NTNU

Norwegian University of
Science and Technology

Adjustable Speed of Synchronous Machine for Hydro Power Application

Erik Hildre Bjørkhaug

Master of Energy and Environmental Engineering
Submission date: June 2017
Supervisor: Trond Toftevaag, IEL

Norwegian University of Science and Technology
Department of Electric Power Engineering

Problem Formulation

Development, implementation, testing and assessment of control of series connected power electronic converter solution for adjustable speed operation of synchronous machine for hydropower plant applications.

- Determination of synchronous machine parameters, by testing of the machine, including realisation of preliminary lab set-up for this purpose.
- Estimation of synchronous machine parameter values not covered by the laboratory experiments.
- Clarification of control strategy and criteria for variable speed control of 3-phase synchronous machine.
- Development of a simulation model of a converter fed synchronous machine, including identification of suitable control system and associated parameter values.
- Further modelling of the lab system, and identification of suitable control system and associated parameter values, including analysis of the simulation results.
- Preparation of compatibility between software/hardware in the lab system. If time permits, order new hardware/software which enables operation with a newer version of Matlab.
- Implement Simulink model of the control system in the lab setup, if time permits.
- Realisation and test of adjustable speed drive of the synchronous machine in lab, if time permits.

Preface

This master thesis was carried out during spring 2017, in my 5th year of studying Energy and Environment. The supervisor for the project has been Trond Toftevaag. The thesis is also linked to the Norwegian Hydropower Center (NVKS), which has variable speed of hydro turbines as an important area of research.

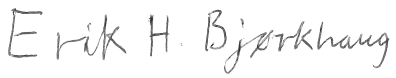

Erik Hildre Bjørkhaug

Trondheim, 2017-06-13

Acknowledgments

I would first like to thank Abel Taffese, who has helped me a lot in my work, both with the understanding of the theory, and with the development of the simulation models. Second, I will thank Brage Iversen, who used of his spare time to help me with the lab setup. I would also like to thank my supervisor Trond Toftevaag, as well as Kjell Ljøkelsøy, Roy Nilsen, Mostafa Valavi, and the personnel at the service lab at the Department of Electrical Engineering, for help and guidance during my work.

E.H.B

Summary

When Europe is transitioning from fossil fuels to renewables, hydropower plants will have an important role in the integration of large quantities of fluctuating sources in the power system, such as wind and solar. With the development of variable speed of hydrogenerators, the objective is to further improve the flexibility and efficiency of the plants. If applying this technology in hydropower plants, Norway can be a green battery in the European power system.

This thesis focuses on the development and preparation of a lab set-up with a converter fed synchronous machine, for research on variable speed of hydrogenerators. This includes testing and documentation of the synchronous machine, modelling and simulation of the lab set-up, development and simulations of possible operating scenarios which later can be tested in lab.

A large part of the work covers determination of parameter values of the 8kVA synchronous machine. Several tests have been conducted in lab, to determine its most important parameter values, while other parameters were estimated based on typical values. Those were needed for modelling of the machine, and tuning of the control system.

A simulation model has been developed to simulate variable speed control of the lab machine, where the machine is fed by a two-level voltage source converter. The objective has been to make the simulation model representative to the lab set-up so that it can be relevant for further lab research. The simulations show that the converter set-up is suitable for adjustable speed control of the synchronous machine.

Synthetic inertia contribution by a converter fed synchronous machine has been simulated, by implementing a control loop that deaccelerates the machine in case of a frequency drop in the grid. This was done by letting the frequency signal pass through a derivative controller, which either affects the torque or the speed reference in case of a frequency drop. Highest impact was achieved by letting the derivative controller affect the speed reference, where the power boost lasted 0.7s and peaked at 18% increase in the presented simulation. A significant impact was also achieved by affecting the torque reference for the inner control loop. However, this impact only lasted 0.1s, since the speed controller quickly compensated for the injection from

the derivative controller. For further work, these operating scenarios can be tested in the lab set-up.

Samandrag

Vasskraftverk, som fleksible kraftprodusentar, vil spele ei viktig rolle for framtidig integrering av sol- og vindkraft i nettet, som kjem med overgangen frå fossile brensler til fornybare kjelder i Europa. Med utvikling av vasskraftverk med variabelt turtal, er målet at fleksibiliteten og verknadsgraden kan bli endå betre, samanlikna med dagens kraftverk. På denne måten kan Norge, med sine vasskraftverk, vere eit grønt batteri i det europeiske kraftsystemet.

Oppgåva fokuserer hovudsakleg på utvikling og førebuing av eit laboppsett med ein omformar-mata synkronmaskin, som kan brukast til vidare arbeid mot variabelt turtal av vasskraftgeneratorar. Dette inkluderer blant anna testing og dokumentasjon av synkronmaskina, modellering og simulering av laboppsettet, og utforming og simuleringar av enkelte vasskraftrelevante scenario som seinare kan testast med laboppsettet.

Ein stor del av arbeidet har vore å fastslå parameterverdiar for den 8kVA synkronmaskina som er brukt i laboppsettet. Fleire testar er blitt utførte for å fastslå dei viktigaste parameterverdiane, medan andre parameter vart estimerte basert på typiske verdiar. Dette var nødvendig for modellering av maskina, samt for å tune regulatorane i systemet.

Turtalsstyring av labmaskina er simulert ved å utvikle ein simuleringsmodell, der synkronmaskina er mata av ein omformar som i laboppsettet. Det er forsøkt å lage simuleringsmodellen så likt laboppsettet som mulig. Simuleringa tyder på at omformarsettet er godt egna for å kunne turtalsstyre synkronmaskina.

Kunstig tregheit frå ein omformar-mata vasskraftgenerator er blitt simulert ved å legge til ein ekstra regulatorstruktur. Ein derivatregulator som har nettfrekvensen som input, vart satt opp slik at den sendte inn ei forstyrring enten på moment- eller turtalsreferansen til maskina, for å bremse generatoren under eit frekvensfall. Størst effekt vart observert ved å sende inn forstyrringa på turtalsreferansen, der effektauken varte i 0.7s, og hadde på det meste 18% effektauke i den presenterte simuleringa. Ein betydeleg effekt vart også observert ved å sende inn forstyrringa på momentreferansen for den indre regulatoren. Denne effekten varte berre 0.1s, sidan den ytre turtalsregulatoren nokså raskt kompenserer for forstyrringa. I vidare arbeid kan dette testast

med laboppsettet.

Contents

List of Tables

List of Figures

Abbreviations

2L-VSC 2-level voltage source converter

CFSM Converter fed synchronous machine

CVS Controllable voltage source

DFIG Double fed induction generator

GSC Grid side converter

IGBT Insulated gate bipolar transistor

MSC Machine side converter

MO Modulus Optimum

SVPWM Space Vector pulse with modulation

SO Symmetrical Optimum

PM Permanent magnet

PWM Pulse with modulation

VSC Voltage source converter

Subscripts

abc Three phase stator variables

$dq0$ Park $dq0$ variables

$base$ Base value

ref Reference

t terminal

a magnetising (reactance, inductance)

d d-axis

q q-axis

0 zero sequence

D d-axis damper winding

Q q-axis damper winding

f d-axis field winding

el electrical

$m, mech$ mechanical

s stator, speed

ss short circuit

sc short circuit

σ leackage (reactance)

sat Saturated

$unsat$ Unsaturated

$inner$ Inner control loop

$outer$ Outer control loop

c Converter

Superscripts

$'$ Transient

$''$ Subransient

$*$ Reference

List of Symbols

x, X Reactance

v, V Voltage

r, R Resistance

l, L Inductance

Ψ Flux linkage

τ Torque

T Time constant

pp Pole pairs

J Inertia

r Radius

H Inertia time constant

n Speed

ω Angular speed

θ Angular position

p, P Active power

pp Pole pairs

S Apparent power

PI PI controller

h_0 Open loop transfer function

K_p Proportional gain

T_i Integral time constant

K_i Integral gain

Chapter 1

Introduction

1.1 Background

New renewable energy, such as wind and solar power, has the potential to provide a huge part of the European energy demand. However, as the power production from wind and solar can not be controlled, there will be a huge demand for controllable power, to maintain stable power supply. When the power from wind and solar is fluctuating, hydropower plants can easily adjust power production to maintain grid stability. Pumped hydro will also play a more important role in future power systems. Then, surplus electricity in periods of high production from wind and solar sources can be stored, and used later when it is more needed.

Hydropower plants, as a flexible source, is playing an important role in this context. This role can be further improved through variable speed control. Some of these benefits are listed below.

- Possibility of pumping with adjustable power in pumped storage plants. [1]
- The flywheel effect of the rotating mass in the rotor/turbine, can be utilised to deliver short power fluctuations to support grid frequency stability. [2][3]
- The turbines can be operated at a high efficiency over a larger range of power output,

including in pumping mode.

- Variable speed of turbines is a prioritised area of research by NVKS/HydroCen, including development of turbines which are specialised for variable speed operation.[4]

1.2 Objective

- Lay a good foundation for further development of a lab set-up for variable speed operation of a synchronous machine, for hydropower applications.
- Contribute with knowledge necessary for realising variable speed operation for hydropower plants, considering the ongoing research linked to NVKS/HydroCen.

1.3 Scope of work

1. Preparation of the lab set up, to perform tests of the synchronous machine, and preparation for converter fed operation.
2. Testing and measurements of synchronous machine in lab.
3. Analysis of the results, and determination of parameter values based on the test.
4. Estimation and calculations of parameter values which were not directly found from measurement from tests.
5. Modelling and simulations of the lab set-up.
6. Simulations of possible applications for variable speed hydro.

1.4 Limitations

The following limitations are applied:

- No studies of efficiency and losses, neither in hydropower turbines nor in the machine/converter, are included.
- Power system dynamics is not included in the simulations.

1.5 Software

MATLAB_R2016b is used for processing of data from the lab tests. The modelling and simulations are also done using MATLAB_R2016b, in the Simulink environment. Components from the Simscape library are used to model the machine and the electrical system, while the rest of the control system is modelled with Simulink blocks. Simulink in MATLAB_R2010b is used in the lab set-up.

1.6 Lab Instruments

The main equipment in the lab is described in chapter 2. Equipment used for logging and measurements are listed in the instrument list in Appendix C.

1.7 Structure of the Report

An overview of, and preparations done on the lab set-up is given in chapter 2

Synchronous machine parameter determination by testing in lab, is described in chapter 3.

Chapter 4 contains estimation of parameter values which are not covered by determination tests in lab. Some parameters are also calculated from a combination of estimated and lab determined parameter values.

General aspects and control strategy for speed control of a synchronous machine are described

in chapter 5

Chapter 6 describes the development of simulation models, for simulations of the lab set up. It also contains simulation results of variable speed using those models.

Chapter 7 contains simulations with a proposed control method, where the rotating mass can contribute with synthetic inertia during a frequency drop. It also contains simulations of variable load pumping.

The synchronous machine is mostly referred to as a machine, as it can be used both for production and pumping in hydropower applications. In general, capital letters are used for physical values, while lower case letters are used for per unit values. The report is written in latex, block diagrams are drawn using the tikz package in latex, while the electrical circuit figures are drawn in Visio.

Chapter 2

Lab Equipment

2.1 An overview of the lab equipment

The lab system consists of the following main equipment:

- 8 kVA synchronous machine (NTNU ID A02-021).
- 20 kVA back to back converter.
- 15 kW asynchronous motor, with an attached motor drive for speed and torque control capabilities.
- Speedgoat real-time target machine, for controlling the 20 kVA converter.

The set-up was formerly used to control a double fed induction machine (NTNU ID: A03-0070), in the spring of 2016 [5]. The modifications done in this project is replacing the DFIG with the synchronous machine. The 15 kW asynchronous machine is coupled to the same shaft, and can be controlled in terms of speed or torque in all four quadrants, by an attached motor drive [6]. It can be used as a controllable mechanical load when operating the synchronous machine.

A diagram of the back to back converter set is given in Figure 2.1. One side is coupled to the 400 V AC grid, while the other side is coupled to the synchronous machine, as shown in Figure 2.2. In the present set-up, the grid side converter controls the DC link voltage, which is kept at 600V.

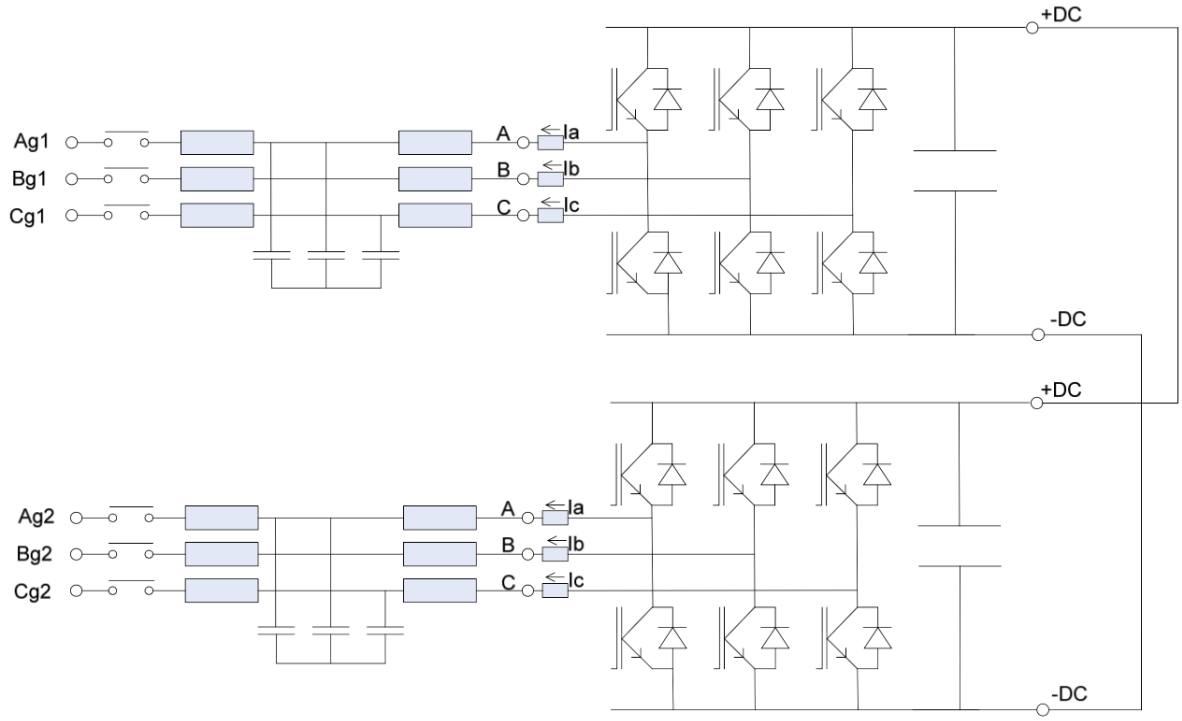

Figure 2.1: Diagram of the 20 kVA back to back converter. One side is coupled to the 400 V AC grid, while the other side is coupled to the synchronous machine

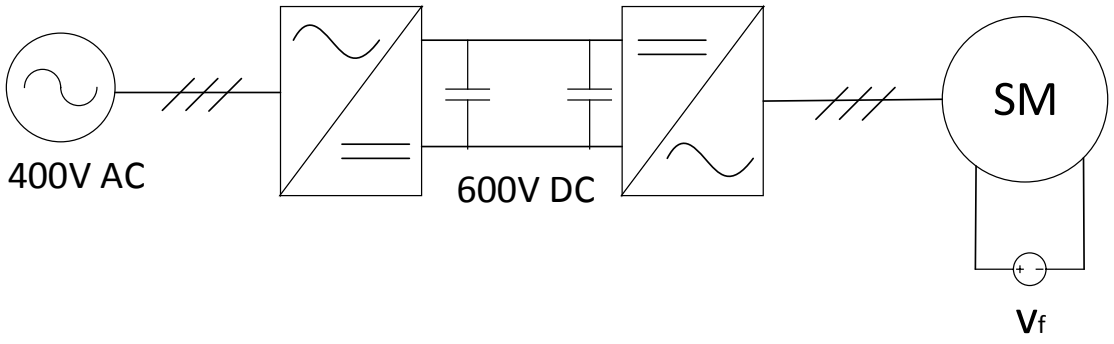

Figure 2.2: One line diagram of the converter set-up

2.1.1 Control system

In the present lab system, the Speedgoat is controlled with a Simulink model, which can be uploaded to the Speedgoat system. The Matlab version used is 2010b, which is compatible with the Speedgoat software. A control system is present, which was developed by Brage Iversen in 2016 [5] for variable speed control of a DFIG, by feeding the rotor circuit.

2.2 Preparation of the Lab Setup

2.2.1 Software on Speedgoat Target Machine

The possibility of upgrading the software on the lab PC was considered and discussed with the personnel at the Service Lab at the Department of Electrical Engineering at NTNU. To be able to make the Speedgoat system compatible with Matlab 2016b, the drivers on the Speedgoat target machine needed to be upgraded. An inquiry to the Speedgoat company was sent, via a staff member at the Service Lab. An offer for upgrading the drivers of all Speedgoat equipment was received from the provider, which is shown in Appendix B.

The total cost for upgrading the Speedgoat software, and maintain a maintenance and support contract for one year, was 2 451.40 EUR. After further discussions, it was decided not to upgrade the Speedgoat system. As there is a process of standardising the equipment and software platform used for similar lab projects at the Department of Electric Power Engineering, the Speedgoat system will most likely be replaced for later projects. The benefits of the upgrades were thereby not considered to be satisfactory, relative to the prise. Hence, Matlab 2010b is still used in the lab set-up for this project.

2.2.2 Decoder for speed and position determination

As the control system in the lab set-up needs speed and position measurements, a decoder coupled to the rotor of the machine is needed, to give feedback to the control system.

The decoder which was attached to the synchronous machine was another type than used in the previous DFIG project, and was not compatible with the rest of the lab system. The decoder used on the DFIG was a digital encoder of the type Hydenhain ROD 420, which sends out 2048 pulses per rotation. As there were no equal decoders available, it was decided to take the decoder from the DFIG used in the previous project, and install it on the synchronous machine.

The original decoder on the synchronous machine was installed to a sleeve, shown in Figure 2.3. The outer sleeve covers the spinning rotor, while fixed to the stator by two screws. The inner tap was coupled to the rotor through an inner sleeve. The Hydenhain decoder had other mechanical measures, and did not fit with the setup on the synchronous machine.

By help from the mechanical work shop, the sleeves were turned in a turning lathe to fit the new decoder. However, it failed because of run-out between the inner and outer sleeve. Since it was a metal to metal coupling, the vibrations caused by the run-out was transferred to the decoder, and could potentially harm it. A new solution was made, where the decoder was installed to a bracket, as shown in Figure 2.4. A flexible hose is used to transfer the rotation of the shaft to the decoder. This dampens the vibrations so that the decoder is less sensitive to run-out.

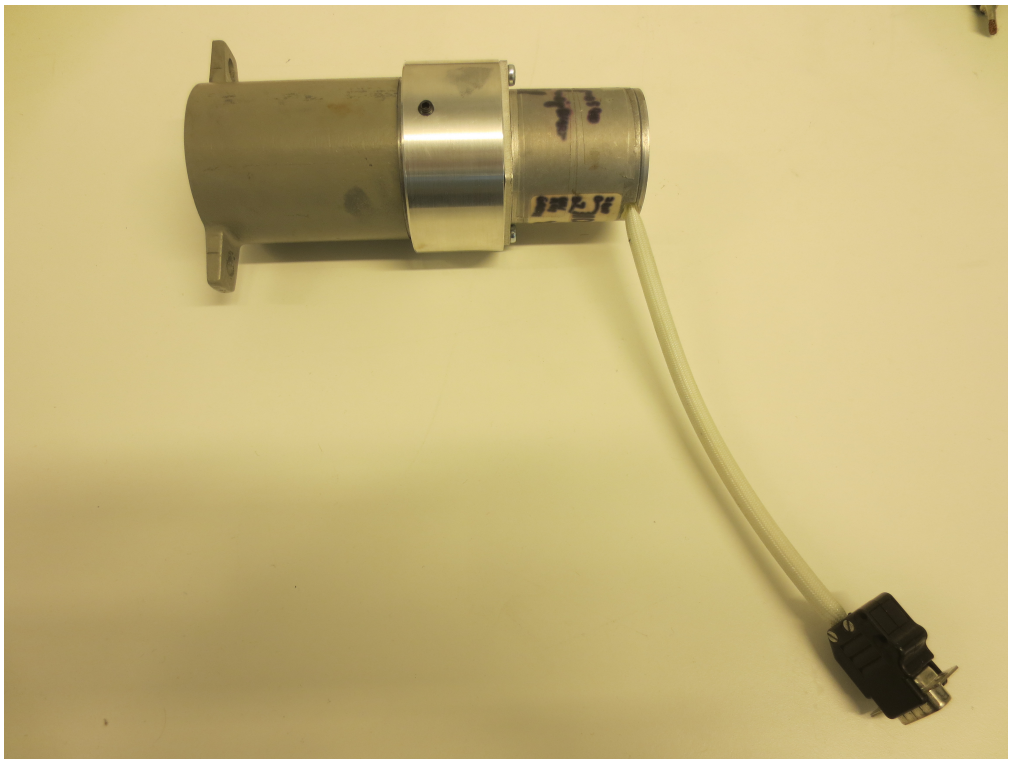

Figure 2.3: Original decoder setup on the synchronous machine

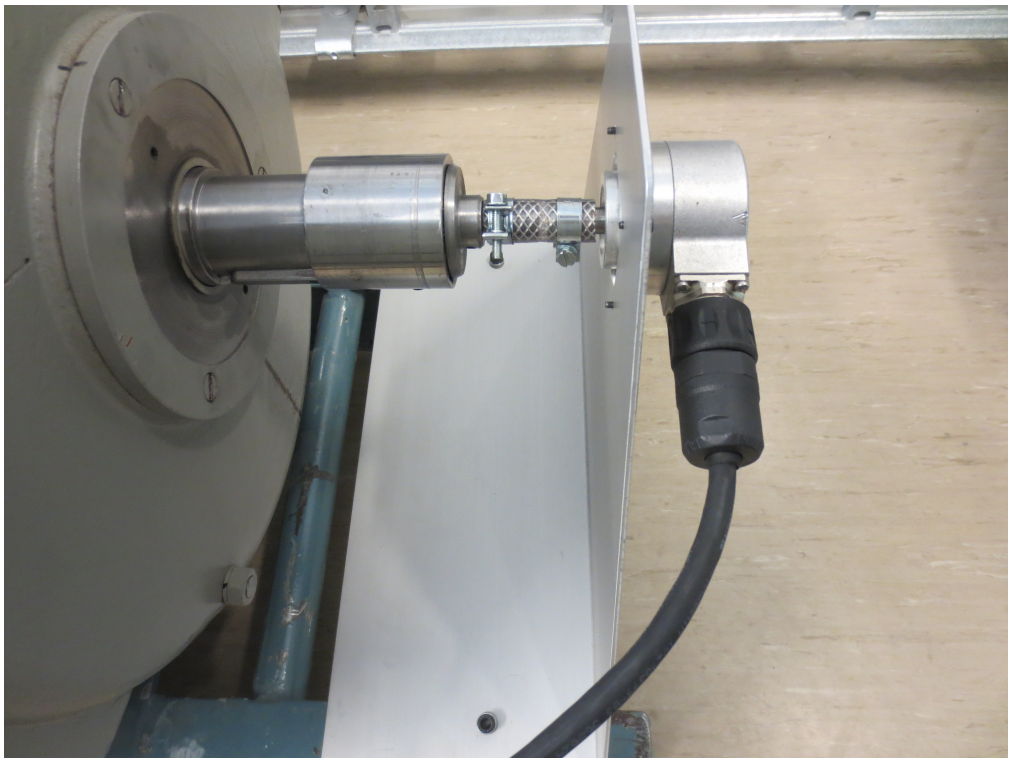

Figure 2.4: New decoder setup made with a bracket and a flexible hose

Chapter 3

Determination tests of Synchronous Machine in Lab

This chapter presents theory, method and results from parameter determination tests in laboratory. Short circuit tests, a slip test and an open circuit saturation test was performed, as well as measurements of resistance. A detailed instrument list of equipment used for measuring and logging, is given in Appendix C. The armature resistance is neglected in all the calculations of stator reactances.

3.1 Synchronous Machine

The 8 kVA synchronous machine is from 1989, is produced by Rudolf Dietze, and has the type number 2GA1320-1FZ. The only available information of the machine was the rated values based on the nameplate. These are listed in Table 3.1. As no other documentation was present regarding the machine's reactances and time constants, parameter determination through physical tests was considered to be necessary.

Using the rated voltage and power, the base values were calculated, and is given in Table 3.2. The per unit quantities are calculated in Appendix A, and are presented in Table 3.2, based on

the generator ratings.

Table 3.1: Synchronous machine rated values as generator/motor as with star connected

Machine parameter	Symbol	Nameplate Values as Generator/Motor
Power	S_n / P_n	8 kVA / 8 kW
Stator voltage (star connected)	V_n	220 V
Stator line current	I_n	21 A / 26.1 A
cos ϕ	-	0.8-1.0 / 0.95
Frequency	f_n	50 Hz
Excitation voltage	-	110-140 V
Excitation current	-	3.5-4.6 A
Speed	n_n	1000 rpm
Maximum speed	-	1500 rpm
Pole pairs	pp	3

Table 3.2: Stator resistance and inductance in physical units

Symbol	Explanation	Value
$S_{s,base}$	Base stator power	8 kVA
$V_{s,base}$	Base stator voltage	179.62 V
$I_{s,base}$	Base stator current	29.7 A
$Z_{s,base}$	Base stator impedance	6.05 Ω
$\omega_{el,base}$	Base electrical speed	100π rad/s
$L_{s,base}$	Base stator inductance	0.01925 H
$\omega_{m,base}$	Base mechanical speed	104.72 rad/s
τ_{base}	Base torque	0.01925 H

3.2 Theory behind a short circuit test

In the event of a three phase short circuit, the armature current will rise significantly in a very short time, which in turn will increase the flux through the rotor. However, the increasing flux will induce currents in the damper and field windings, which will prevent more flux entering the rotor core. This screening effect forces the flux to go through the air around the rotor, where the reluctance is much higher. This lasts until the energy of the induced currents is dissipated in

the rotor winding resistances. The first time period after the short circuit, with screening effect from both the field and the damper windings, is called the subtransient state. Subsequently, the machine will enter the transient state, where there is screening effect from the field winding only, and the flux path is only partly through air. Eventually, the machine reaches steady state again. [7]

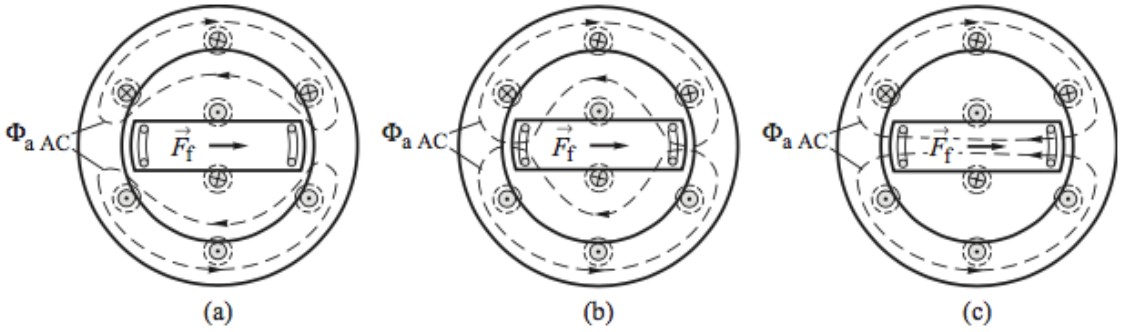

Figure 3.1: The armature flux path in the subtransient state (a), transient state (b) and steady state (c). [7]

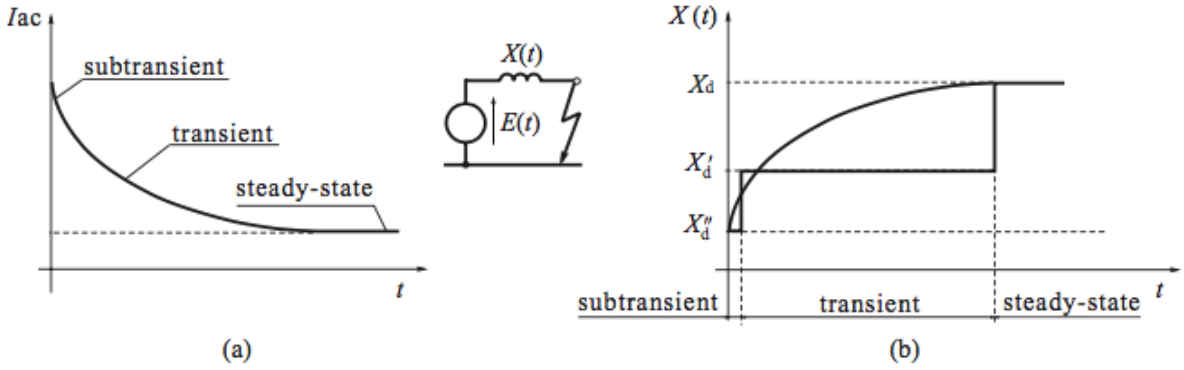

Figure 3.2: AC short circuit current in the different states, and the time dependency of the stator reactance [7]

As the damper windings normally have much higher resistance than the field winding, the machine will typically enter the transient state after some milliseconds, when the energy of the induced damper currents is dissipated. After the transient state, the machine reaches steady state, and the armature flux is allowed to pass the iron rotor.

The induced voltage is the q-axis, meaning that currents will be in the d-axis, since armature impedance is mainly reactive. The equation for the AC short circuit is given in Equation (3.1) [8]. This can be rewritten, using the reactance given in Table 3.3, and the induced voltage at the time of the short circuit, as showed in Equation (3.2).

$$I_{SC,AC}(t) = (I'' - I')e^{-t/T''_d} + (I' - Iss)e^{-t/T'_d} + I_{ss} \tag{3.1}$$

$$I_{SC,AC}(t) = E * [(\frac{1}{X''_d} - \frac{1}{X'_d})e^{-t/T''_d} + (\frac{1}{X'_d} - \frac{1}{X_d})e^{-t/T'_d} + \frac{1}{X_d}] \tag{3.2}$$

Table 3.3: Synchronous machine parameters which determines AC short circuit current

Machine parameter	Symbol	Physical explanation
d-axis subtransient reactance,	X''_d	d-axis reactance with full rotor screening
d-axis transient reactance	X'_d	d-axis reactance with partly rotor screening
d-axis reactance,	X_d	Steady state reactance with no screening
d-axis subtransient time constant,	T''_d	Time used for subtransient component of short circuit current to be reduced to $1/e = 0.368$ of its initial value
d-axis transient time constant	T'_d	Time used for transient component of short circuit current to be reduced to $1/e = 0.368$ of its initial value

3.2.1 DC component of a short circuit

As can be seen in Figure 3.3, the short circuit current consists of a DC component in addition to the AC current. The size of the DC component will be dependent of the rotor position at the instant of the short circuit. Figure 3.4 shows the rotor position γ using phase A as the reference. A fault may occur at any rotor position $\gamma = \gamma_0$. If a fault occurs at $\gamma_0 = 0 \pm \pi$, the instantaneous value of the induced phase voltage will be zero, while flux from the rotor will induce maximum

DC component, referring to phase A. The opposite will be the case for $\gamma_0 = \pi/2 \pm \pi$. Then, the induced voltage will be at the top/bottom of its sine wave, while the DC component of the short circuit will be zero. Thus, the DC component will be proportional to $cos(\gamma_0)$ [7]. The DC current will exponentially decay to zero, as it is dissipated in the armature resistance, according to the time constant of the armature circuit, T_a. The equation is shown in (3.3) [7].

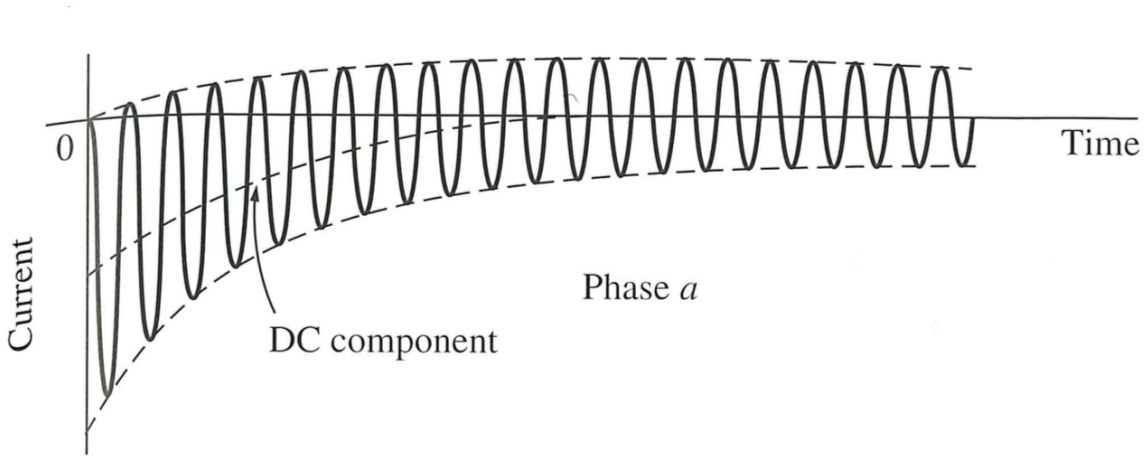

Figure 3.3: Short circuit current with DC component [9]

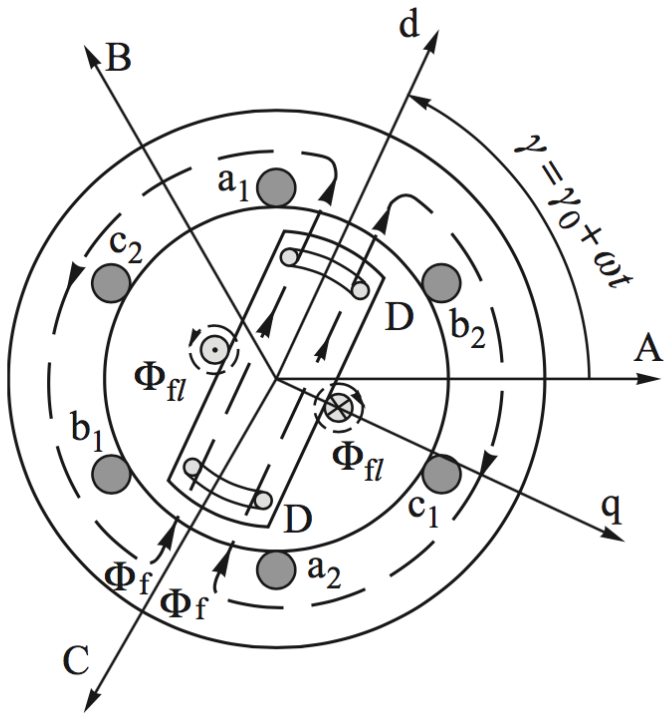

Figure 3.4: Rotor position after time t [7]

$$i_{A,DC}(t) = i_{A,DC}(0) * e^{-t/T_a} \tag{3.3}$$

3.3 Analysis of Short Circuit Test

The performance of the short circuit tests is based on the IEEE Standard 115-1983 [8]. The procedure of finding the transient current and time constants, is by subtracting the steady state value of the short circuit current, and thereby plotting it on a natural logarithmic scale, as shown in Figure 3.5 (curve B). A straight line can then be drawn from the transient state back to zero time (curve C), to find the transient current (I'). The time constant is found where the transient part (line C) has reached $1/e = 0.3678$ of its original value. The subtransient part of the current is found by subtracting line C from line B, and the same process can be repeated. For analysis of

the results, Matlab was used, as further described in section 3.5.

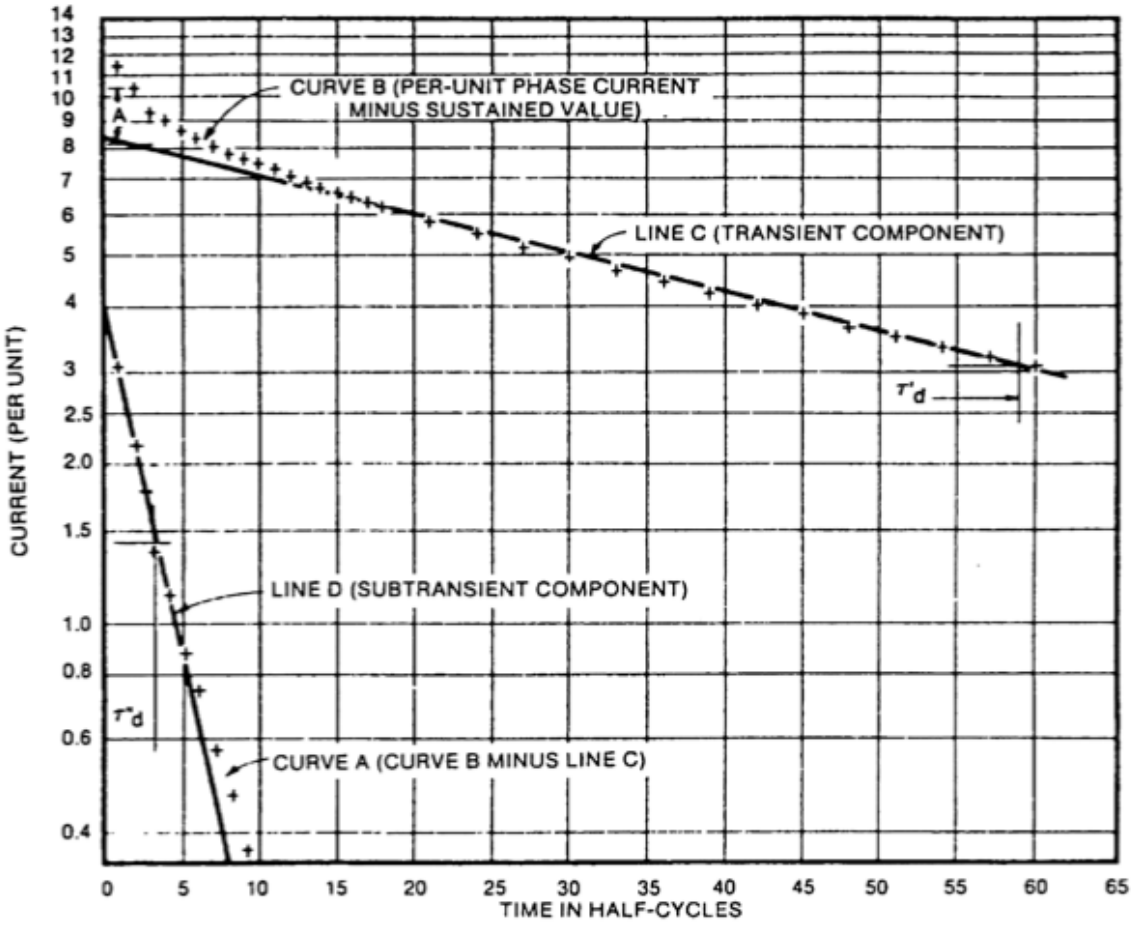

Figure 3.5: Semi-logarithmic plotting of the transient and subtransient part of the short circuit current, according to IEEE standard 115-1983 [8]

3.4 Short circuit test in laboratory

The electrical machine lab consists of a set up for both magnetising and a three phase short circuit of a synchronous machine. This set-up has earlier been used in a lab assignment at NTNU, and can be seen in Figure 3.6. The synchronous machine is coupled to the field excitation unit and the short-circuiter the same way as this circuit diagram. However, the induction motor mentioned in chapter 2 was used to operate the system at nominal speed, which was controlled manually at the motor drive display.

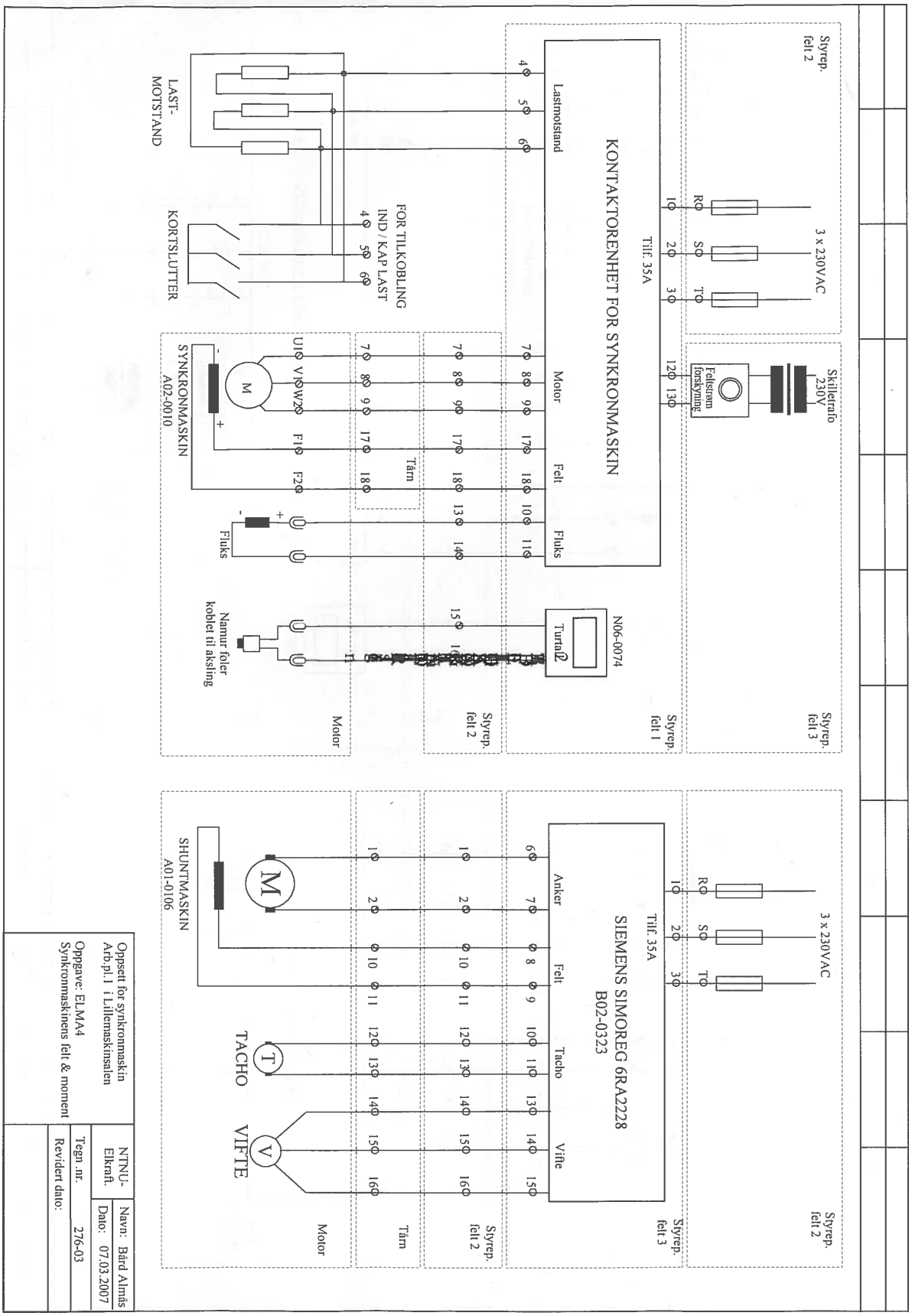

Figure 3.6: Set up for running short circuit tests of the synchronous machine

An oscilloscope was used for measuring and logging of the phase current of one of the phases, the phase voltage of the same phase, and the field current. Current meter tongs was used to measure the currents, while a differential probe was used to measure the phase voltage. The tests were logged using the single shot function on the oscilloscope. It was set to trig when the phase current was rising. In this way, the short circuit and the following cycles could be logged and saved to a CSV file, for each short circuit test.

During the short circuit tests, the induction motor was controlled to run at 1000 rpm, while the field winding was magnetised so that induced voltage reaches the nominal value at open-circuited terminals. A multimeter was used to monitor that the line voltage of the machine was 220 V, while the phase voltage can be measured to be 127 V_{rms} at the oscilloscope. The field current was measured to be 2.6 A at the oscilloscope, while the field voltage was measured to be 82 V during these conditions.

3.5 Results of short circuit tests

As it was not possible to control the rotor angle at the instant of the short circuit, it was a challenge to get test results without a DC component. Over hundred tests were conducted and examined considering the phase voltage prior to the short circuit, and DC component in the following current. The four tests with the lowest DC component were analysed as described in section 3.3, while another with a high DC component was analysed to find the armature time constant.

By plotting the short circuit current and the phase voltage together, it is possible to see exactly where on the phase voltage waveform the short current occurred. The tests where it occurred close to either top or bottom of the voltage, was taken further. The DC component was examined by looking at the absolute value of the first half cycles of the current. If the current does not decrease from one half cycle to the next during the transient state, it indicates that there is a DC component. The tests with the lowest DC component were selected for further research. The four tests, #64, #75, #90 and #102, were analysed further, because of their low DC component,

while test #99 was analysed to find the armature time constant. The current of each half cycle, as well as the time relative to the short circuit, was manually read for each of the tests. Their measured time of occurrence relative to the sinusoidal phase voltage, is presented in Table 3.4. Common for the presented tests is that they were measured to occur slightly before a peak value of the phase voltage. Although there were tests that hit more directly on top or bottom, a slightly higher DC component was seen. This may indicate that the current measurement tong has a small time delay.

The tests were analysed using Matlab, as well as linear regression, as described in section 3.3. Matlab's curve fitting toolbox was also used. In this way, exponential expressions could be approximated directly. In the analysis, the envelope of the AC current was found, meaning the peak values are used. This was taken into account when the reactances were calculated. Plots from test #75 and #102 are presented in this section, as they had the lowest DC component. Test $64 and #90 are presented in Appendix D. Plots of the field currents during the short circuit is also presented in this appendix.

Table 3.4: Measured time of occurrence relative to phase voltage

Test	Time of occurrence
#64	1 ms before top
#75	1 ms before top
#90	2.5 ms before top
#102	1.5 ms before top

3.5.1 The steady state and transient component

Figure 3.7 shows the short current of test #102. From the steady state region, it can be seen that the peak value of the steady state current is $I_{ss,peak} = 46A.$, a similar value is found from the other tests, which gives the steady state reactance:

$$X_d = \frac{E}{I} = \frac{127V * \sqrt{2}}{46} = 3.90\Omega \tag{3.4}$$

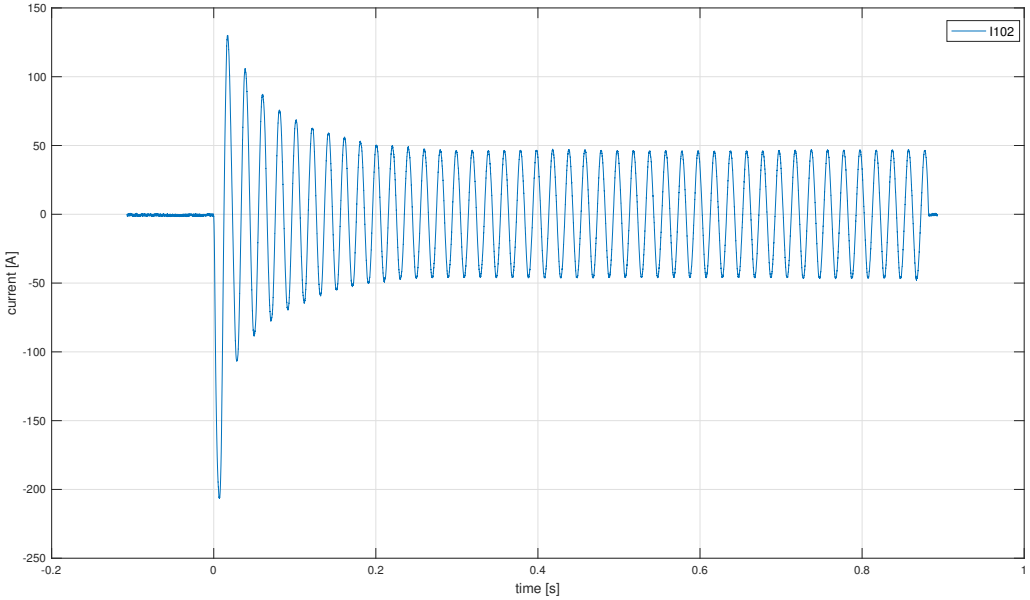

Figure 3.7: The short circuit current from test #102

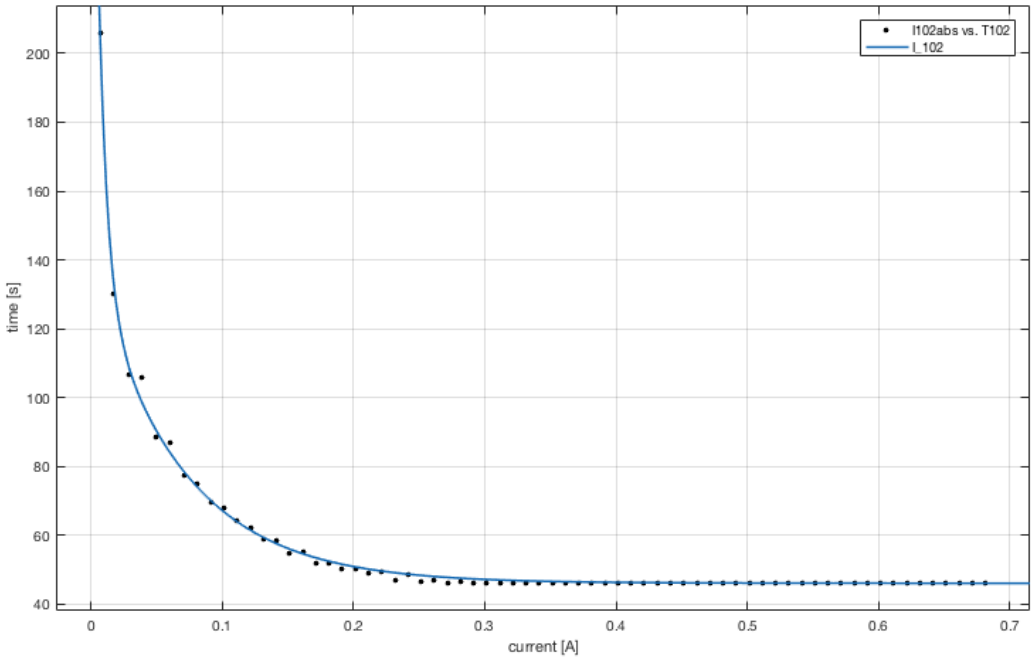

Figure 3.8: Curve fitting test #102

Using the custom equation function in the curve fitting toolbox in Matlab, Equation 3.1 was fitted to short circuit current, which recorded for every half cycle, as shown in Figure 3.8. Results from the curve fitting suggest that the transient component $I' - I''$ is in the range 88-93 A, while the transient time constant is in the range 65-75 ms. By plotting the natural logarithm of the transient and subtransient component (subtracting the steady state value), a straight line can be drawn from the transient state, following the IEEE standard. In Figure 3.10 and Figure 3.9, the straight line $\ln(90) + t/0.069$ is shown to fit well for both tests.

The logarithm of the transient part of the short circuit current, $(I' - Iss)e^{-t/T'_d}$, from Equation (3.1), can be rewritten as shown below in (3.5). This shows that the found line $\ln(90) + t/0.069$ corresponds to $(I' - I_{ss}) = 90A$, and $T'_d = 0.069$. The transient reactance is thereby calculated in (3.6).

$$\ln(I' - I_{ss}) - 1/T'_d = \ln(I' - I_{ss}) * e^{-t/T'_d} = \ln(90) * e^{-t/0.069} \tag{3.5}$$

$$X'_d = \frac{E}{I'} = \frac{127V * \sqrt{2}}{(46+90)A} = 1.32\Omega \tag{3.6}$$

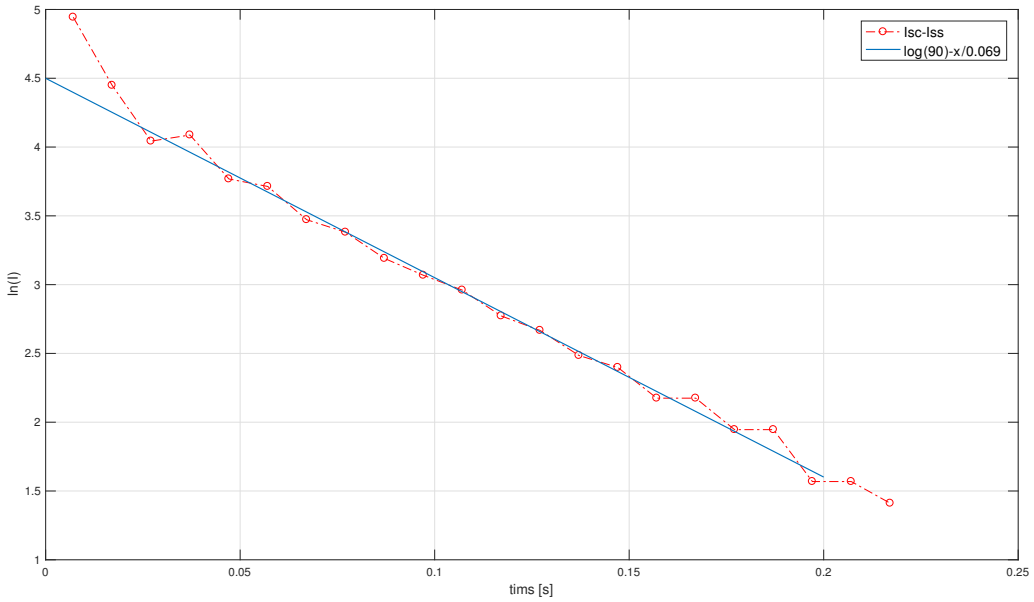

Figure 3.9: Semi-logarithmic plot of the transient and subtransient part of the short circuit current of test #75, plotted with its linearised function $\ln(90) + t/0.069$

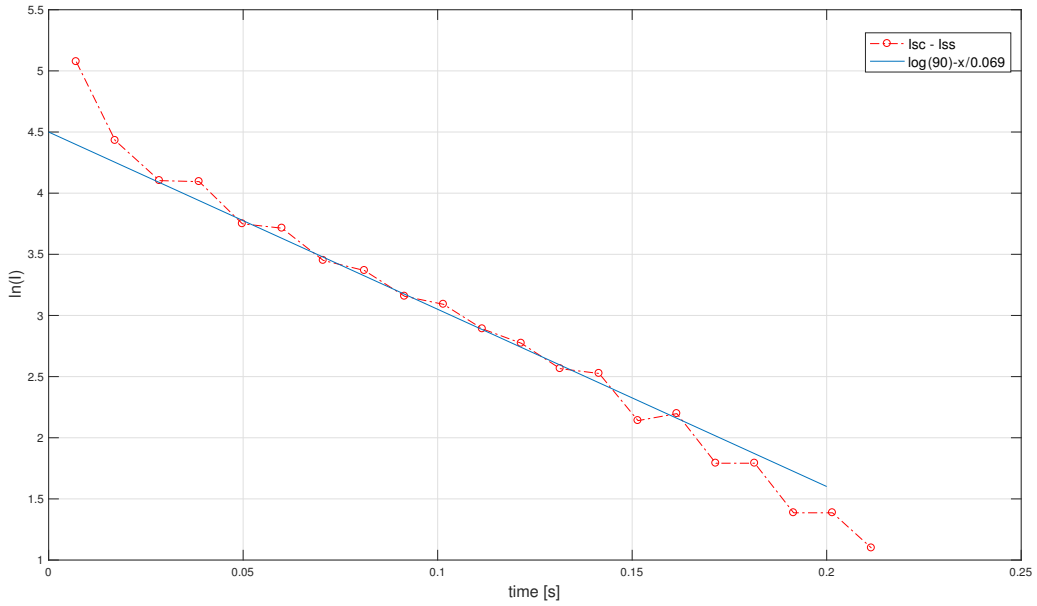

Figure 3.10: Semi-logarithmic plot of the transient and subtransient part of the short circuit current of test #102, plotted with its linearised function $\ln(90) + t/0.069$

3.5.2 The subtransient component

Since the subtransient time constant of this machine is very small, it is difficult to separate the transient and subtransient component from each other. To plot the subtransient component, the transient function, found in the previous subsection, and the steady state current, is subtracted from the short circuit current. In some cases, like in test #75, this leads to a negative value for the third half cycle. A small DC component or measurement error can lead to such results. Semi-logarithmic plotting is thereby only done for the two first half cycles, as shown in the two following figures. The curve fitting tool in Matlab was also used, to fit the first half cycles with an envelope according to (3.1). The steady state and transient variables were fixed, according to the values that were previously calculated. Then the subtransient values were calculated to fit the defined curve to the measured test. The results are presented in Table 3.5 and Table 3.6.

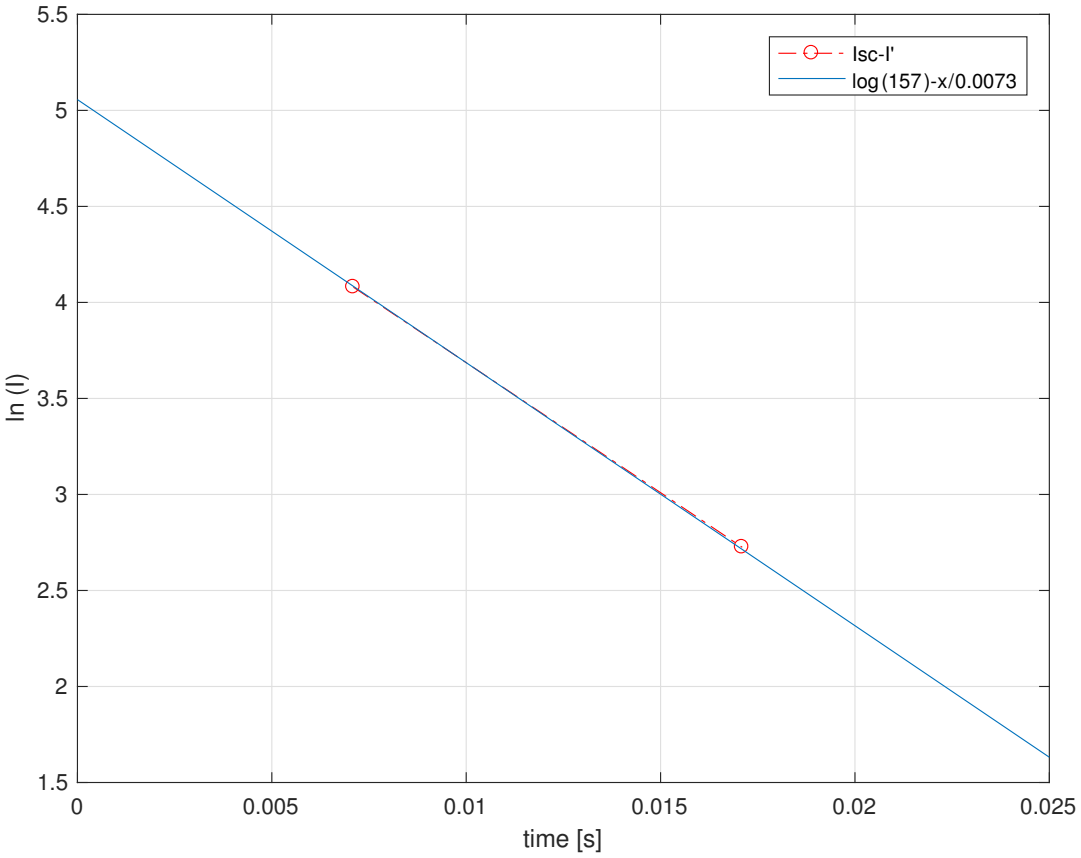

Figure 3.11: Semi-logarithmic plot of the subtransient part of the short circuit current of test #75. $ln(I) = log(157) - x/0.0073$ fitting the two first half cycles

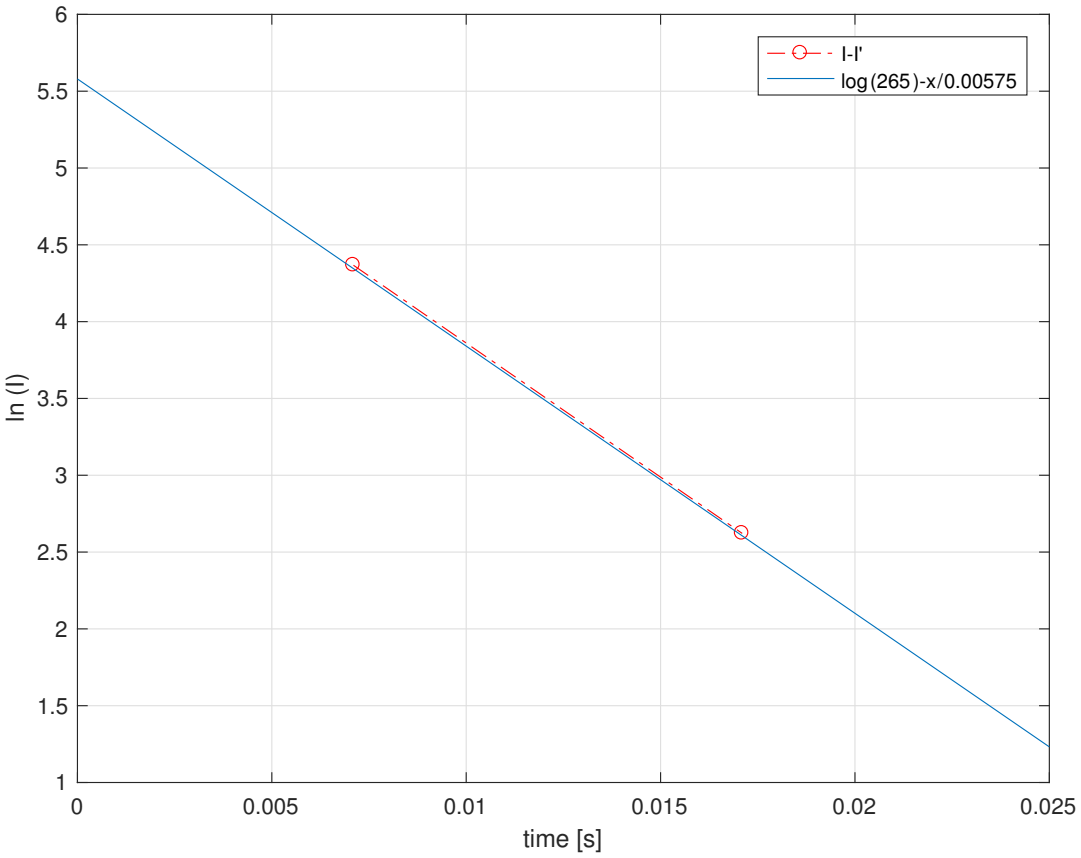

Figure 3.12: Semi-logarithmic plot of the subtransient part of the short circuit current of test #102. $ln(I) = ln(265) - x/0.00575$ fitting the two first half cycles

Table 3.5: Results from semi-logarithmic plotting of the subtransient component

Test	Subtransient component $(I' - I'')$	Subtransient time constant, T''_d
#75	157 A	7.3 ms
#102	265 A	5.75 ms

Table 3.6: Results using the curve fitting in Matlab

Test	Subtransient component $(I' - I'')$	Subtransient time constant, T''_d
#75	172 A	6.64 ms
#102	267 A	5.81 ms

From looking at figure Figure 3.9 and Figure 3.10, it seems like test #75 has small DC component which is lowering half cycle 1 and 3, and raising half cycle 2 and 4. The opposite is happening for test #102. Thereby test #75 gives a too low subtransient component, and too high time constant, and vice versa for $102. A good approximation can be to take the mean values found by curve fitting. The calculation of the subtransient reactance is shown in (3.9).

$$(I'' - I') = \frac{172A + 267A}{2} = 220A \tag{3.7}$$

$$T''_d = \frac{6.6ms + 5.8ms}{2} = 6.2ms \tag{3.8}$$

$$X''_d = \frac{E}{I''} = \frac{127V * \sqrt{2}}{(46 + 90 + 220)A} = 0.505\Omega \tag{3.9}$$

3.5.3 Envelope of short circuit current

The envelope of the AC short circuit current was from the prior results found to be:

$$I_{SC,AC}(t) = 220e^{-t/0.0062} + 90e^{-t/0.069} + 46 \qquad [A] \tag{3.10}$$

The envelope was plotted together with the short circuit currents in Figure 3.13 and Figure 3.14. It fits good for both test, although small differences can be observed. For example, it can be seen that the first half cycle is slightly bigger than the envelope for test #102. For test #75, half cycle 1 and 3 are slightly lower than the envelope. This strengthens the hypotheses that the two tests

have a small DC component in each direction.

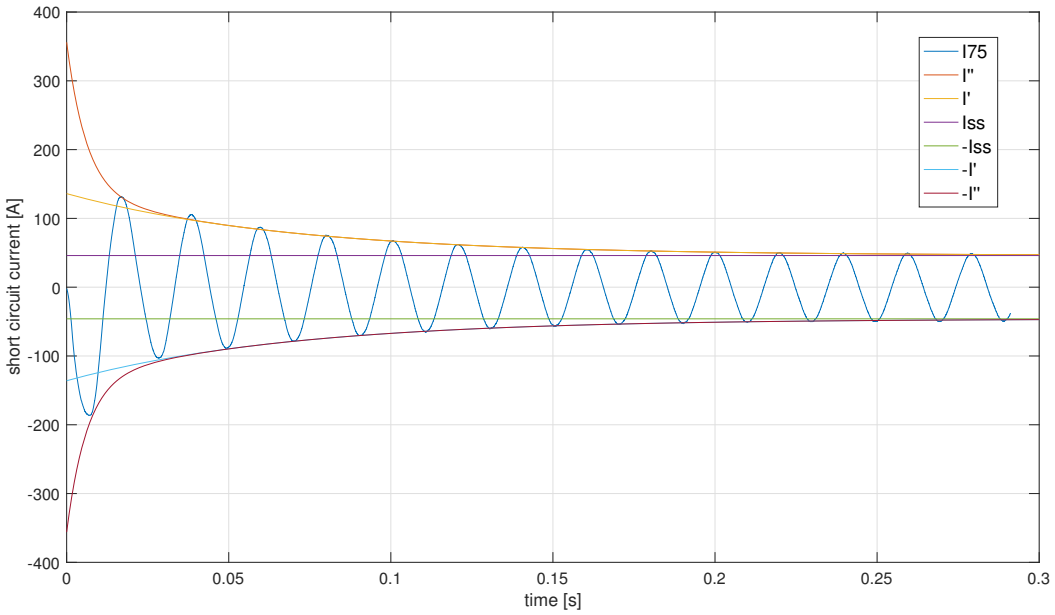

Figure 3.13: The developed envelope plotted together with the results from short circuit test #75

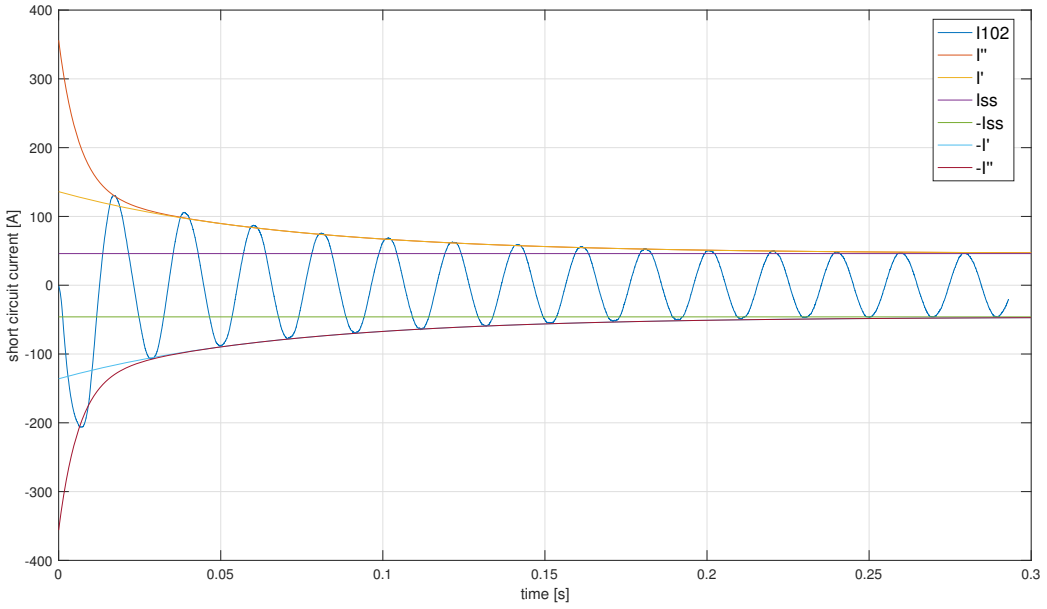

Figure 3.14: The developed envelope plotted together with the results from short circuit test #102

3.5.4 Armature time constant

To estimate the armature time constant, test #99 was used, which occurred at the zero crossing of the sine wave of the phase voltage. This means the DC component of the current is close to its maximum value. The armature time constant T_a can be found by analysing how fast the DC current was decreasing, according to Equation (3.3). The DC component from a short circuit can be isolated by comparing the envelope of short circuit test #99 with the calculated AC envelope (3.10). The values in (3.3) was found by adding it to (3.10), like showed in (3.11). The values were thereby found by the Matlab curve fitting tool.

$$I_{SC,AC}(t) = 220e^{-t/0.0062} + 90e^{-t/0.069} + 46 + I_{DC}e^{-t/T_a} \tag{3.11}$$

The fitted line in Figure 3.15 is equal to the expression (3.12) below, meaning the armature resistance was found to be $T_a = 14ms$.

$$I_{SC,AC}(t) = 220e^{-t/0.0062} + 90e^{-t/0.069} + 46 + 173 * e^{-t/0.014} \tag{3.12}$$

$$T_a = 0.014s \tag{3.13}$$

In Figure 3.16, the DC component was plotted, as well as $I_{DC}(t) + I_{SC,AC}(t)$ and $I_{DC}(t) - I_{SC,AC}(t)$, together with short circuit test #99.

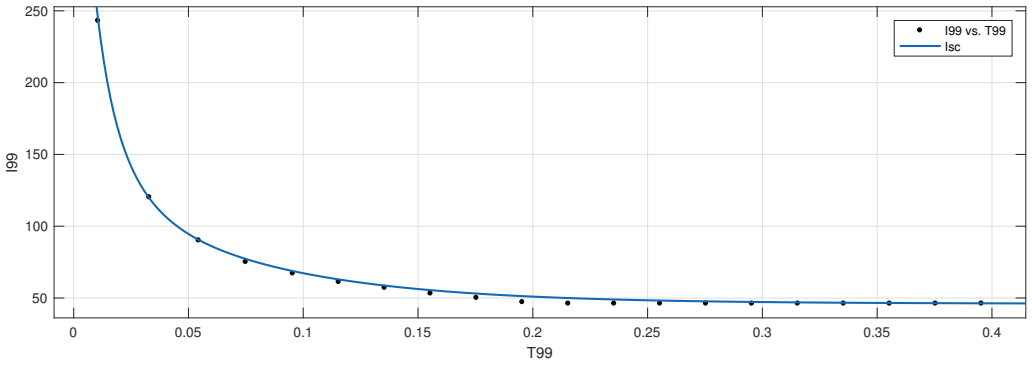

Figure 3.15: Curve fitting of the positive half cycles of test #99

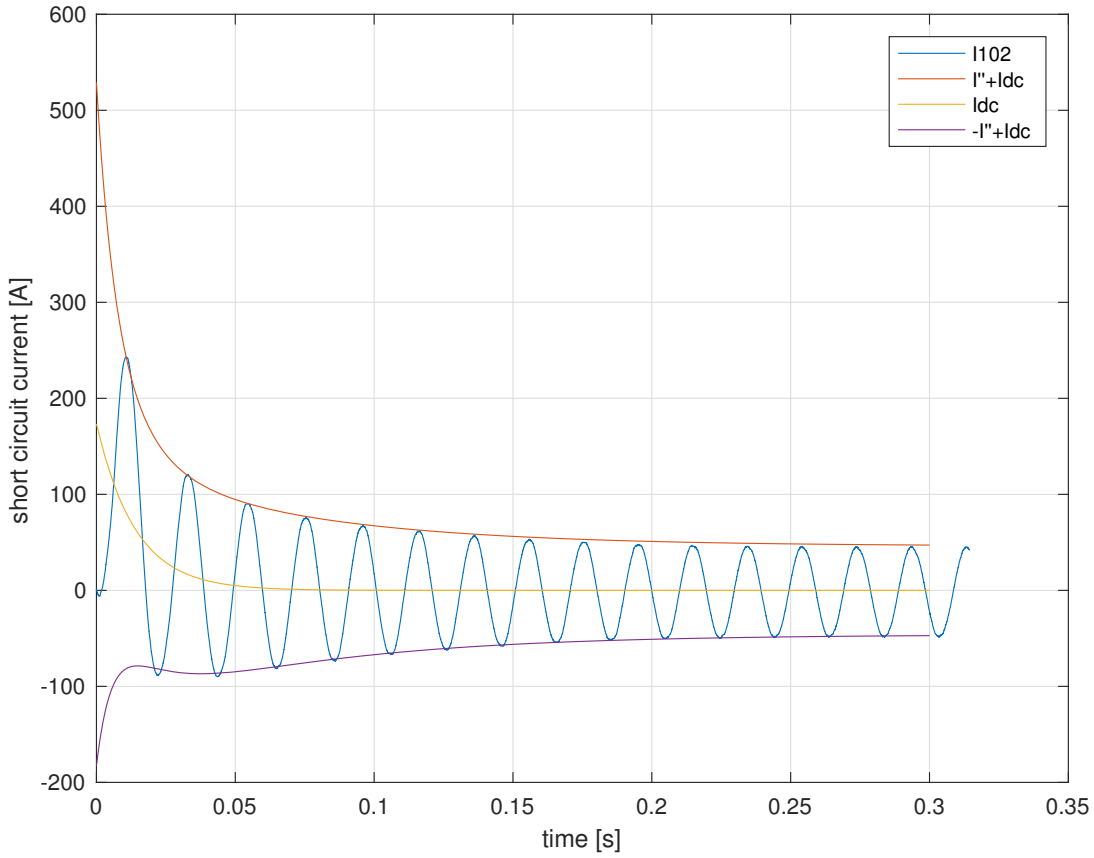

Figure 3.16: Envelope of short circuit current with maximum DC component, together with the results from short circuit test #99

3.6 Slip test

A slip test, also according to the IEEE standard [8], was performed. The test was done by spinning the rotor with a slip, relative to synchronous speed, with the field open circuited, fed by a low voltage at nominal frequency.

The test was done by feeding the machine from the converter, as shown in Figure 2.2. The present lab control system in Matlab 2010b, was modified, so that it could deliver the desired voltage and frequency. This was done by disconnecting the current and speed controllers, so that the voltage and frequency could be controlled manually in open loop. The frequency was set to 50 Hz, while it was tried with voltages in the range 30-40 V and slips from 1-5%. The voltage and currents contained some ripple and noise, and had to be filtered using the filter function in Matlab when plotting the currents from the CSV files.

On of the tests is shown in Figure 3.17, which is done at 5% slip and a line voltage of 33.9V. $I_{min,peak}$ = 6.975A and $I_{max,peak}$ = 10.927A is read from the plot, which is used to calculate the d- and q- axis reactance.

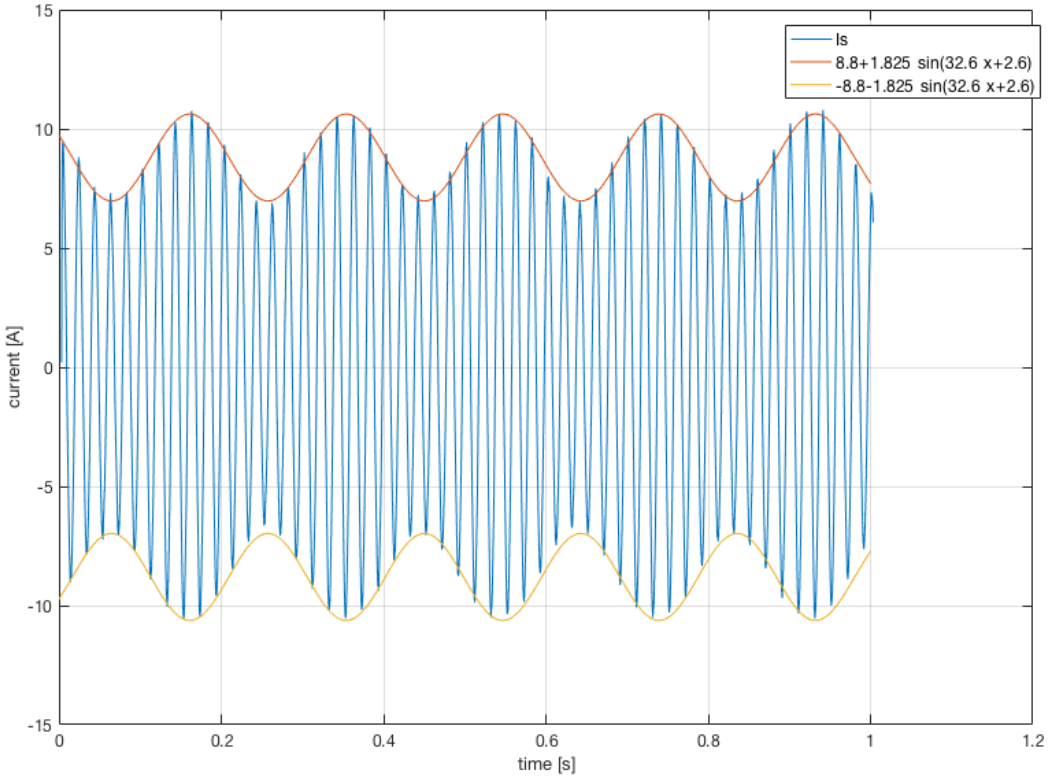

Figure 3.17: Slip test at 5% slip

$$I_{min,rms} = \frac{6.975A}{\sqrt{2}} = 4.93A \tag{3.14}$$

$$I_{max,rms} = \frac{10.927A}{\sqrt{2}} = 7.51A \tag{3.15}$$

$$X_{d,slip} = \frac{V_t}{I_{min}} = \frac{33.9V}{\sqrt{3} * 4.92} = 3.97\Omega \tag{3.16}$$

$$X_{q,slip} = \frac{V_t}{I_{max}} = \frac{33.9V}{\sqrt{3} * 7.51} = 2.61\Omega \tag{3.17}$$

$$ratio_{X,dq} = \frac{X_{q,slip}\Omega}{X_{d,slip}\Omega} = \frac{2.61}{3.97} = 0.657 \tag{3.18}$$

The results for the d-axis reactance varies slightly from the short circuit test. As the short circuit test is considered to be more precise, the q-axis reactance is calculated using the found ratio.

$$X_q = X_d * ratio_{dq} = 3.90\Omega * 0.657 = 2.56\Omega = 0.423pu \tag{3.19}$$

3.7 Field and armature resistance

The armature resistance was measured using a milliohm meter, type Instek GOM - 802. All three phases were measured between the neutral point and the terminals. The resistance was found to be $R_a = 0.2185\Omega$ per phase at approximately 25 °C.

The field resistance was measured with a multimeter, and was found to be $R_f = 31.1\Omega$ at 20-25 °C. It was found to be slightly higher during operation, as a slightly higher field voltage was needed to induce the same terminal voltage, compared to the initial conditions when the cold machine was started. This is most likely caused by the heat generated by the losses in the field windings. Measurements taken right after operating the machine was in the range 31.5-32Ω.

3.8 Open Circuit Test

An open circuit test was performed to evaluate the saturation properties of the machine. The terminal voltage was measured while applied field voltage was varied from 20-150V. The machine was running at nominal speed with open circuited terminals.

The results are presented in Figure 3.18. An air gap line is extrapolated from the lowest field voltages, showing the unsaturated induced voltage, which can be used to calculate the unsaturated

synchronous reactance. At rated terminal voltage, 220V, the field voltage is 84.5V, while the extrapolated air gap voltage is 230.5V.

The unsaturated synchronous reactance can be calculated by dividing the air gap value of the voltage by the short circuit current, for a particular field current, as shown in 3.20. [10]

$$X_{s(unsat)} = \frac{E_{air-gap-value}}{I_{sc}} \tag{3.20}$$

A modified air gap line can be drawn from the operation point $E = V_n$, which will be valid for operation at the nominal terminal voltage at rated speed. The saturated reactance will be $X_{s(sat)} = E/I_{sc}$ [10].

The reactances previously calculated was found when $E = V_n$, meaning they are saturated according to the modified air gap line. The unsaturated values can be found by comparing the air gap line voltage with the induced voltage, at the operation point of the short circuit tests.

$$X_{s(unsat)} = \frac{230.5V}{220V} * X_{s(sat)} = 1.048 * X_{s(sat)} \tag{3.21}$$

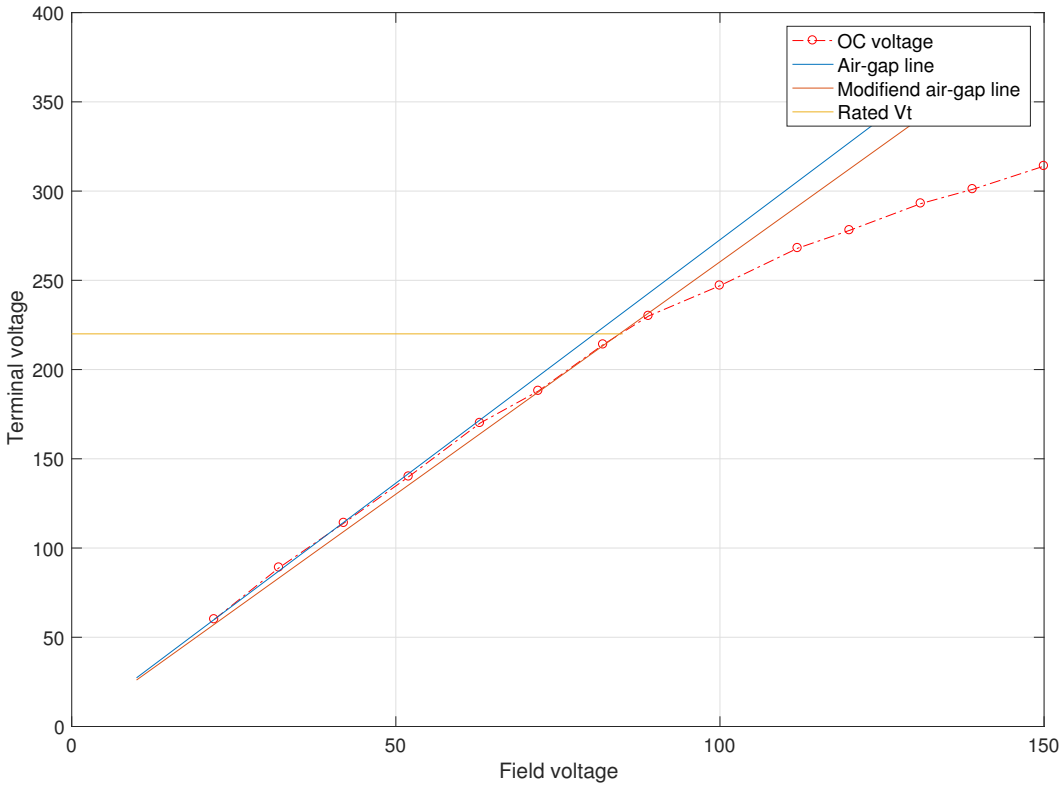

Figure 3.18: Open circuit voltages plotted against extrapolated air gap line

The measurements were done using two multimeters. One for field voltage measurements, and another to measure the terminal voltage. The test was conducted after running the machine with excited rotor for a few minutes, so that a steady state value of the field winding resistance was reached.

3.9 Results from testing

Table 3.7: Synchronous machine impedances found from direct measurements and tests

Explanation	Symbol	Physical Value	Per Unit Value
Stator resistance	R_s / r_s	0.2185Ω	0.036
Field winding resistance	R_f	31.5Ω	-
d-axis synchronous reactance	X_d / x_d	3.9Ω	0.644
q-axis synchronous reactance	X_q / x_q	2.56 Ω	0.423
d-axis transient reactance	X'_d / x'_d	1.32 Ω	0.218
d-axis subtransient reactance,	X''_d / x''_d	0.505 Ω	0.083

Table 3.8: Synchronous machine time constants from testing

Explanation	Symbol	Value
d-axis transient short-circuit time constant	T'_d	0.069 s
d-axis subtransient short-circuit time constant	T''_d	0.0062 s
Armature time constant	T''_a	0.014 s

3.10 Discussion of the lab results

The found steady state and transient values, can be considered to be quite accurate. There are several half cycles in both the steady state and the transient state, and several of the short circuit tests gives similar values. However, d-axis subtransient values are more uncertain, as there are only a two or three half cycles for doing extrapolation. Also, the two best test result give quite different results. The found ratio between d and q-axis synchronous reactances, was according to the expectations for a salient pole machine. Typical ratios for such machines are in the area 0.6-0.7 [11] [12]. which is very similar to the result from the slip test.

The reactances, and especially the subtransient reactance, are smaller than typical per unit values for salient pole synchronous machine [11] [12]. One choice that affects the per unit values is the calculation of base quantities. As discussed in Appendix A, choosing to calculate the base

impedance using the rated current in motor mode, would give a smaller base impedance. This would make the per unit values 25% higher, without affecting the physical units. The resistance is neglected in the calculation of reactances. Including it would reduce the smallest reactances slightly.

Compared to larger machines, the per unit armature resistance is higher, while the time constants is shorter [11] [12]. The armature time constant will be low when the armature resistance is higher, which is correct for this case. The per unit resistance in the field and damper winding are also most likely larger for this small lab machine, then in bigger machines. This will make the transient and subtransien time constants shorter.

Assuming equal saturation for the d and q-axis, all the found reactances are saturated according to the saturation level found in section 3.8. During converter fed operation, it is planned that the machine will be run at the same, or close to, the field current used during the short circuit tests. It will thereby be operated at the same saturation condition as in the short circuit test. Therefore, it was decided to use the saturated values in the further work. According to the open circuit test, the unsaturated values are only 4.8% higher than the saturated, which is probably within the accuracy range of the short circuit test.

The stator resistance is measured at cold conditions. The machine has not been run with high stator current for long continuous periods. Therefore it is not certain which temperature and resistance the stator will have, when it is run for long time periods under loaded conditions. In the first step, the measured resistance is used. However, it can be adjusted upwards for later work.

The measurement of the field circuit resistance, can be validated, by using the specifications from the nameplate. According to the nameplate, a field voltage of 110-140V will make field current of 3.5-4.6A. By using the lowest or highest values, an approximate value can be calculated. The measured value corresponds well to the calculated value in (3.22), and can thereby be assumed to be quite accurate.

$$R_{f,nameplate} = \frac{U_{f,nameplate}}{I_{f,nameplate}} = \frac{110V}{3.5A} = 31.42\Omega \tag{3.22}$$

Chapter 4

Estimations and calculations of parameter values

In this chapter, relevant synchronous machine parameter values are estimated based on typical values for similar machines. By combining these with the values found in the previous chapter, per unit values of the rotor circuits can be calculated. Some of the parameter values are needed for modelling of the machine, while others are required for tuning of the controllers in the simulation model. Some parameter values are also calculated to compare with the lab results, to evaluate the reliability of the found parameter values.

4.1 Leakage and magnetising reactance

The leakage reactance must be lower than the subtransient reactance, and is typically around 10% of the d-axis synchronous reactance [11]. According to this assumption, the leakage reactance is 0.064 pu, which is 77% of the subtransient reactance. This should be a reasonable approximation, although the ration to the subtransient value is slightly higher than typical salient pole values [11].

$$x_{s\sigma} = 0.1 * x_d = 0.064pu = 0.77 * x''_d \tag{4.1}$$

From this, the magnetizing reactances can be calculated, which is the mutual reactance between stator and rotor windings:

$$x_{ad} = x_d - x_{s\sigma} = 0.644pu - 0.064pu = 0.58pu \tag{4.2}$$

$$x_{aq} = x_q - x_{s\sigma} = 0.423pu - 0.064pu = 0.36pu \tag{4.3}$$

4.2 q-axis parameters

For salient pole machine, x'_q, equals x_q, since there is no field winding. The subtransient reactance x''_q had to be guessed based on the machine design, and typical values for synchronous machines. By looking into the machine, one can observe that it has full damper windings in the d-axis only, which is linked with a complete copper ring. For a machine with complete damper windings, x''_q equals x''_d; if not, x''_q will be higher [7]. In the case of a linking copper ring, the screening effect will be slightly weaker in the q-axis, and x''_q was estimated to be $1.5 * x''_d$.

The subtransient time constant is typically in the same range as in the d-axis [12], and is assumed to be equal.

$$x'_q = x_q = 0.423pu \tag{4.4}$$

$$x''_q \approx 1.5 * x''_d = 1.5 * 0.083pu = 0.125pu \tag{4.5}$$

$$T''_q \approx T''_d = 0.0062s \tag{4.6}$$

4.2.1 Open-circuit time constants

The open circuit time constants were calculated based on approximated relationships [7], as shown below.

$$T'_{d0} \approx \frac{x_d}{x'_d} * T'_d = \frac{0.644}{0.218} * 0.069s = 0.20s \tag{4.7}$$

$$T''_{d0} \approx \frac{x'_d}{x''_d} * T''_d = \frac{0.218}{0.083} * 0.0062s = 0.016s \tag{4.8}$$

$$T''_{q0} \approx \frac{x'_q}{x''_q} * T''_q = \frac{0.423}{0.125} * 0.0062s = 0.021s \tag{4.9}$$

4.3 Field and damper winding leakage reactance and resistance

The transient and subtransient reactances consist in reality of several reactances in series and parallel. They are determined of the magnetising reactance, as well as the leakage reactances in stator and rotor windings, as shown in Figure 4.1, 4.2 and 4.3

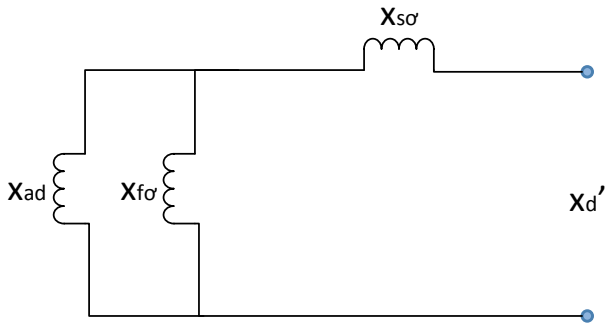

Figure 4.1: Equivalent scheme of the d-axis transient reactance

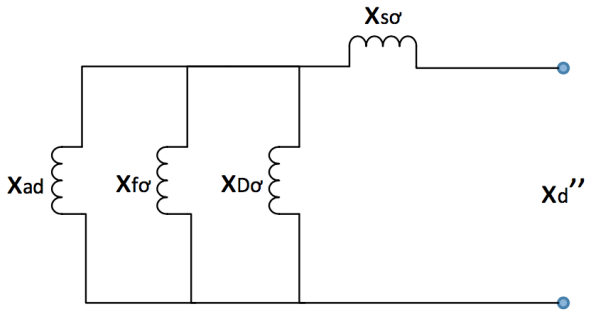

Figure 4.2: Equivalent scheme of the d-axis subtransient reactance

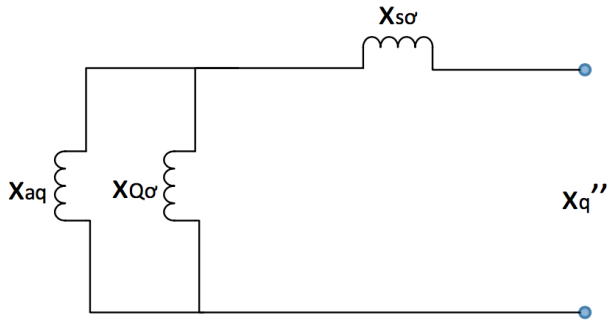

Figure 4.3: Equivalent scheme of the q-axis subtransient reactance

By using the equivalent schemes above, the leakage reactances in the field and damper windings can be calculated:

$$x_{f\sigma} = \frac{1}{\frac{1}{x'_d - x_s\sigma} - \frac{1}{x_{ad}}} = \frac{1}{\frac{1}{0.218-0.064} - \frac{1}{0.58}} = 0.21 \tag{4.10}$$

$$x_{D\sigma} = \frac{1}{\frac{1}{x''_d - x_{s\sigma}} - \frac{1}{x_{ad}} - \frac{1}{x_{f\sigma}}} = \frac{1}{\frac{1}{0.083-0.064} - \frac{1}{0.58} - \frac{1}{0.209}} = 0.022 \tag{4.11}$$

$$x_{Q\sigma} = \frac{1}{\frac{1}{x''_q - x_{s\sigma}} - \frac{1}{x_{aq}}} = \frac{1}{\frac{1}{0.125-0.064} - \frac{1}{0.36}} = 0.073 \tag{4.12}$$

The per unit value of the field and damper winding resistances can be calculated by using the the classical expression for the time constants T''_d, T''_q and T'_d [13] [11], and the previously found values. The formulas for $T_6 \approx T''_d$ and $T_4 \approx T''_d$ are approximate because a reactance, which is mutual between field and damper windings only, and not the stator, is ignored [11].

$$T_3 \approx T''_d = \frac{1}{\omega_n * r_D} * (x_{D\sigma} + \frac{1}{\frac{1}{x_{ad}} + \frac{1}{x_{s\sigma}} + \frac{1}{x_{f\sigma}}}) \tag{4.13}$$

$$r_D \frac{1}{2 * 50 * \pi * 0.0062} * (0.022 + \frac{1}{\frac{1}{0.58} + \frac{1}{0.064} + \frac{1}{0.21}}) = 0.035 \tag{4.14}$$

$$T''_q = \frac{1}{\omega_n * r_Q} * (x_{Q\sigma} + \frac{1}{\frac{1}{x_{ad}} + \frac{1}{x_{s\sigma}}}) \tag{4.15}$$

$$r_Q = \frac{1}{2 * 50 * \pi * 0.0062} * (0.073 + \frac{1}{\frac{1}{0.36} + \frac{1}{0.064}}) = 0.065 \tag{4.16}$$

$$T'_d \approx T_4 = \frac{1}{\omega_n * r_f} * (x_{f\sigma} + \frac{1}{\frac{1}{x_{ad}} + \frac{1}{x_{s\sigma}}}) \tag{4.17}$$

$$r_f = \frac{1}{2 * 50 * \pi * 0.069} * (0.21 + \frac{1}{\frac{1}{0.58} + \frac{1}{0.064}}) = 0.012 \tag{4.18}$$

4.4 Inertia and mechanical time constant

The mechanical time constant is the double of the inertia time constant, which is defined as the kinetic energy of the rotating mass, divided by the rated power. It can be calculated from equation 4.19, based on the inertia, and rated speed and power [11].

$$T_m = 2 * H = 2 * \frac{E_k}{S_n} = 2 * \frac{\frac{1}{2} J\omega^2}{S_n} [s] \tag{4.19}$$

Assuming a solid cylinder, the inertia of the rotor can be calculated using equation 4.20 [14].

$$J = \frac{1}{2} mr^2 [kg * m^2] \tag{4.20}$$

The measures of the physical size of the two rotors in the system are presented in Table 4.1. The diameter of the synchronous machine is measured directly, while the other parameters are approximated based on the size of the stator. The nameplate value of the total weight is also stated.

Table 4.1: Approximated rotor measurements

Parameter	Synchronous machine	Induction machine
Diameter	0.16 m	0.15 m
Length	0.40 m	0.30 m
Total weight	210 kg	98 kg

Assuming a typical density for electric steel $\rho = 7650 kg/m^3$ [15], the mass of the rotors can be calculated:

$$m_{SM} \approx V\rho = \pi r^2 l\rho = \pi * (\frac{0.16m}{2})^2 * 0.40m * 7650kg/m^3 = 61.5kg \tag{4.21}$$

$$m_{IM} \approx \pi * (\frac{0.15m}{2})^2 * 0.30m * 7650kg/m^3 = 40.6kg \tag{4.22}$$

$$J_{SM} \approx \frac{1}{2} * 61.5kg * (\frac{0.16m}{2})^2 * 61.5kg = 0.2kg * m^2 \tag{4.23}$$

$$J_{IM} \approx \frac{1}{2} * 40.6kg * (\frac{0.15m}{2})^2 * 40.6kg = 0.1kg * m^2 \tag{4.24}$$

The shafts connecting the machines have a very low inertia compared to the rotors, because of a much smaller diameter and a relatively small length. They are therefore neglected in the calculation of the total inertia.

$$J_{total} = J_{SM} + J_{IM} = 0.3kg * m^2 \tag{4.25}$$

Thus, the mechanical time constant is calculated:

$$T_m = \frac{0.3kg/m^2 * (104.72rad/s)^2}{8kVA} = 0.41s \tag{4.26}$$

4.5 Overview of calculated and estimated parameter values

A full overview of the parameter values which are estimated and calculated in this chapter is given in Table 4.2.

Table 4.2: Estimated synchronous machine parameters in per unit

Explanation	Symbol	Value
q-axis subtransient short-circuit time constant	T''_{q0}	0.0062s
d-axis transient open-circuit time constant	T'_{d0}	0.20s
d-axis subtransient open-circuit time constant	T''_{d0}	0.16s
q-axis subtransient open-circuit time constant	T''_{q0}	0.21s
Mechanical time constant	T''_{m}	0.41s
q-axis subtransient reactance	x''_{q}	0.125
Stator leakage reactance	$x_{s\sigma}$	0.064
d-axis magnetizing reactance	x_{ad}	0.58
q-axis synchronous reactance	x_{aq}	0.36
field winding leakage reactance	$x_{f\sigma}$	0.21
d-axis damper leakage reactance	$x_{D\sigma}$	0.022
q-axis damper leakage reactance	$x_{Q\sigma}$	0.073
field resistance	r'_{f}	0.012
d-axis damper resistance	r_{D}	0.035
q-axis damper resistance	r_{Q}	0.065

4.6 Evaluation of the parameter values

Some of the parameter values of the machine can both be found through lab tests, and calculated from other parameter values. This applies to the armature time constant, and the field circuit resistance. The parameter values used in the calculations are both from the lab tests in the previous chapter, and from estimations in this chapter.

4.6.1 Armature time constant

The armature time constant was already found through analyses of the DC component in a short circuit test. However, it can also be found through the armature resistance and the subtransient inductances. Using the equation (4.27) from [11], the armature time constant can be calculated.

$$T_a = \frac{1}{Ra}\frac{x''_d + x''_q}{\omega_n * 2}[pu] = \frac{1}{0.036}\frac{0.083 + 0.125}{100\pi * 2}s = 0.0092s \tag{4.27}$$

When comparing the result found in subsection 3.5.4 with the time constant calculated in (4.27), the time constant from lab is 50% longer than the calculated. Possible sources of this mismatch can be inaccuracies in the measurements of the armature time constant, including the curve fitting of the DC component. Also the measurements of the d-axis subtransient reactance, and the estimated q-axis value, are uncertain, and the found values might be too low.

4.6.2 Field circuit resistance

By finding the the base quantities of the field circuit, it is possible to calculate the physical value of the field resistance, based on the d-axis reactances and time constants, which was calculated in section 4.3. The per unit value of field current, is chosen so that the magnetising reactance for the field winding has the same per unit value as the d-axis magnetising inductance [11]. From previous tests, it is known that a field current of 2.6A (I_{f0}) is needed to induce 1 pu of voltage at rated speed. Hence, d-axis flux linkage $\Psi_d = 1$, while stator current is 0. Thereby, it is possible to find the base value of the field current, based on the per unit model in section 5.1:

$$\Psi_d = x_{ad} * i_{f0} = x_{ad} * \frac{I_{f0}}{I_{f_base}} = 1 \tag{4.28}$$

$$I_{f,base} = x_{ad} * I_{f0} = 0.58 * 2.6A = 1.508A \tag{4.29}$$

Based on the definition of the field circuit base values [11], the base voltage and impedance can be calculated:

$$U_{f,base} = \frac{S_n}{I_{f,base}} = \frac{8000kVA}{1.508} = 5305V \tag{4.30}$$

$$Z_{f,base} = \frac{U_{f,base}}{I_{f,base}} = \frac{5305V}{1.508A} = 3518\Omega \tag{4.31}$$

The per unit field circuit resistance found in (4.18), can thereby be calculated in physical units:

$$R_f = r_f * Z_{f,base} = 0.012 * 3518\Omega = 42\Omega \tag{4.32}$$

This calculated value is over 30% higher than the measured value of 31.5 Ω, found in chapter 3 by multimeter. The measured value is considered to be quite accurate, at least within a fault of 1-1.5Ω, as it also corresponds well to the rated field current and voltage from the nameplate. However, the calculations are based on a mix of values found by lab tests and estimated values. Changes in several of the values would lead to a more correct field resistance calculation. For example, if the stator leakage reactance $x_{s\sigma}$ had been bigger, it would make the field winding leakage reactance $x_{f\sigma}$ smaller according to (4.10). This would in turn make the calculated field resistance smaller, according to equation (4.18). The same would happen if the transient reactance x'_d was smaller, or the transient time constant T'_d was longer.

4.6.3 Discussion

In both cases there is a significant difference between the measured value, and the value calculated from other parameter values, which are both measured and calculated. This indicates that there are inaccuracies in either the measurements or the calculations, or in both. The calculations are dependent on parameter values from both testing and approximation based on typical values.

The exact sources of error are therefore difficult to identify. The rounding of the values during the calculations might also lead to some of the mismatch, as well as the equation used to calculate the field resistance, represents an approximate relationship. As it is difficult to determine by certainty which parameter values should be adjusted, it was decided to use the found parameter values without further adjustments.

Regardless, the measured and estimated values should be sufficiently accurate for simulation purposes, as the machine model will be defined by the same values used to calculate control variables. However, they might need to be adjusted when tuning the control system for the physical machine.

Chapter 5

Control strategy for a synchronous machine drive

This chapter presents a control strategy for a synchronous machine drive, based on using the equipment in the lab set-up. The machine side converter is fed from a constant voltage DC link, and feeding the machine with variable voltage and frequency. The task of the grid side converter (GSC) will thereby be to maintain a constant voltage on the DC link. Control strategies for both the synchronous machine controller and grid side controller are presented, although the main focus is on the machine side control.

5.1 Per unit model of the synchronous machine

It is favourable to use park transformation, to simplify the control system [16]. In park transformation, voltages and currents in the abc frame, is transformed to corresponding DC quantities in the rotating $dq0$ frame. The zero sequence component will be zero, as long as the system operates under balanced conditions, meaning the sum of the instantaneous values $v_a + v_b + v_c = 0$ and $i_a + i_b + i_c = 0$. A per unit model in the $dq0$ frame is presented below, which is based on [13] and [11].

Flux linkages:

$$\Psi_d = x_d * i_d + x_{ad} * i_f + x_{ad} i_D \tag{5.1}$$

$$\Psi_q = x_q * i_q + x_{aq} i_Q \tag{5.2}$$

$$\Psi_0 = x_{s\sigma} * i_0 \tag{5.3}$$

$$\Psi_f = x_{ad} * i_d + xf * i_f + x_{ad} i_D \tag{5.4}$$

$$\Psi_D = x_{ad} * i_d + x_D i_D \tag{5.5}$$

$$\Psi_Q = D = x_{aq} * i_q + x_Q i_Q \tag{5.6}$$

Stator voltages:

$$v_d = r_s * i_d + \frac{1}{\omega_n} \frac{d\Psi_d}{dt} + n * \Psi_q \tag{5.7}$$

$$v_q = r_s * i_q + \frac{1}{\omega_n} \frac{d\Psi_q}{dt} + n * \Psi_d \tag{5.8}$$

$$v_0 = r_s * i_0 + \frac{1}{\omega_n} \frac{d\Psi_0}{dt} \tag{5.9}$$

Field and damper windings voltages:

$$v_f = r_f * i_f + \frac{1}{\omega_n} \frac{di\Psi_f}{dt} \tag{5.10}$$

$$0 = r_D * i_D + \frac{1}{\omega_n} \frac{di\Psi_D}{dt} \tag{5.11}$$

$$0 = r_Q * i_Q + \frac{1}{\omega_n} \frac{di\Psi_Q}{dt} \tag{5.12}$$

Reactances:

$$x_d = xad + x_{s\sigma} \tag{5.13}$$

$$x_q = xaq + x_{s\sigma} \tag{5.14}$$

$$x_f = xad + x_{f\sigma} \tag{5.15}$$

$$x_D = xad + x_{D\sigma} \tag{5.16}$$

$$x_Q = xaq + x_{Q\sigma} \tag{5.17}$$

Torque and power:

$$T_m \frac{dn}{dt} = \tau_{el} - \tau_{mech} \tag{5.18}$$

$$\tau_{el} = \Psi_d * i_q - \Psi_q * i_d \tag{5.19}$$

$$\frac{d\theta}{dt} = \omega_n * n \tag{5.20}$$

$$p = v_d * i_d + v_q * i_q + 2 * v_0 * i_0 \tag{5.21}$$

The base quantities for the stator are normally the rated values. For the field and damper windings, the base quantities are chosen so that the per unit value of the mutual inductance between them and the stator has the same value for all the rotor windings. In that way, x_{ad} and x_{aq} will have the same value for the stator and rotor windings, so that the per unit model above will be correct. The procedure of calculating the base values of the rotor windings, is for example given in [11].

5.2 Cascaded control system with an outer and inner control loop

A typical way of designing a control system for an electrical machine drive, is with a cascaded control system [17]. The outer control loop regulates the speed, by sending a torque reference to the inner system, as shown in Figure 5.1. The inner controller regulates the current, based on the torque, and should be considerably faster than the outer loop. In a synchronous machine, the q-axis current is proportional to the torque. Therefore, the per unit torque reference is can be directly used as reference for i_q for the inner control system.

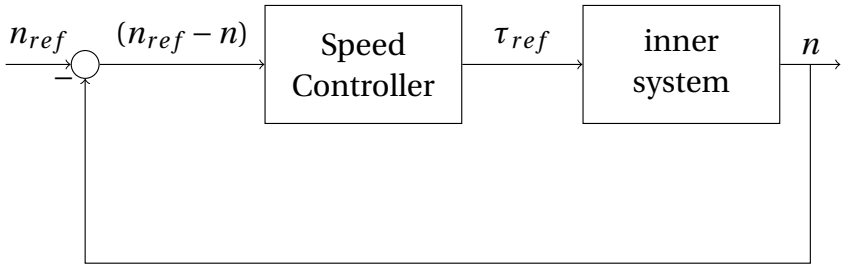

Figure 5.1: Principal block diagram of speed control loop

Figure 5.2 shows an inner current control system for a PM machine. The control system for a PM machine will be very similar, although feedback from the field current is needed for the synchronous machine, to determine the flux linkage in the d-axis. The figure uses a slightly different notation. This PM machine does as well not have different inductance values in d- and q-axis. When including the field winding, and using the notation using in this report, the decoupling terms becomes:

$$v_{d,ref} = PI_d + n * \psi_q = PI_d + n * x_q * i_q \tag{5.22}$$

$$v_{q,ref} = PI_q + n * \Psi_d = PI_q + n * (x_d * i_d + i_f * x_{ad}) \tag{5.23}$$

The way the per unit inductance is defined in this report, it does not make any difference whether

the reactance or the inductance is used in the equations. The damper windings are ignored in the decoupling, since it is not possible to measure them. Also, they have no effect in steady state operation.

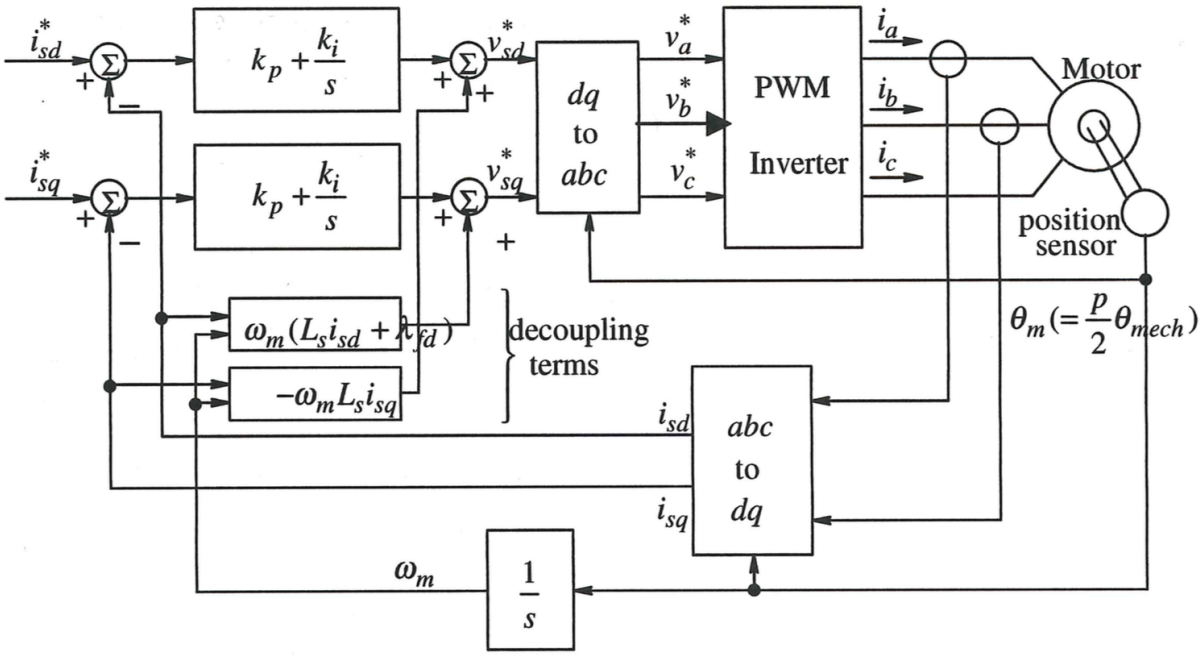

Figure 5.2: Inner control system of a PM machine [18]

Both the d-axis current and the field current affect the voltage level on the stator, according to the flux linkage equations. Thereby, it will also affect the torque, according to (5.19). The strategy used in this report is to inject stator current only in the q-axis, while the field current is used to keep d-axis flux linkage Ψ_d to 1 pu. This is done by setting the $i_{d,ref}$ to zero, and $i_{f,ref}$ to the value which induces rated voltage at no load. The field current controller can be tuned by modulus optimum, similar to the inner current controller.

5.3 Tuning of controller

5.3.1 PI controllers

The proportional and integral (PI) controller is one of the most used controllers in industry for electrical machine drive systems [17]. It is efficient in terms of following references, and because of the integral part, it can remove the steady state error after a disturbance. It is is widely used in electrical machine drives, and has also been used in this project.

The behavior of the proportional part is given by the proportional gain K_p, which is multiplied by the error between the reference and the feedback signal.

The response of the integral part is given by the integral time constant T_i or the integral gain constant K_i, depending on the form of the transfer function. T_i is the time an error of 1 has to be integrated, before the output from integrator increases with 1. The ratio between T_i and K_i is $K_i = \frac{K_p}{T_i}$, which can be seen from Equation (5.24).

$$PI_{controller} = K_p \frac{1 + T_i s}{T_i s} = K_p * (1 + \frac{1}{T_i s}) = K_p + K_i s \tag{5.24}$$

A saturation limit is often applied to the controller, to prevent that the output is exceeding the physical limits of the system. If the controller keeps integrating, a negative error is needed for some time, to get the controller out of saturation. This is called *wind-up*, and should be prevented. The controllers should therefore have a feature that stops the integration when saturation is reached. This is called *anti-wind-up* functionality[16].

5.3.2 Sampling and filtering

The measurements in the feedback loops are normally taken with a specific sampling frequency. This means the controllers will be digital, since they will receive discrete measurements signal. Some filtering of the measured signal will anyway be required, since converters used to feed machine produce a certain amount of ripple. The filter should then prevent the ripple from entering the controller, which will also make ripple in the controller output.

A sampling technique called synchronous sampling can be used in combination with digital controllers, for the inner current controllers. Then, the current must be measured exactly at top and bottom of the triangular PWM curve of the converter. In this way, the measurement is sampled in the middle of the duty cycle. Thereby, most of the ripple is avoided in the sampling of the measured current, so that a smaller filtering time constant can be chosen [16].

5.3.3 Modulus and Symmetrical Optimum

Modulus and symmetrical optimum, can be used to tune the PI controllers in a electrical machine drive, which gives a predefined stability limit [19]. The presented technique is for continuous controllers, but will be approximately correct for digital controllers as well. The digital sampling time can also be taken into account, by including a discrete time z-domain, to improve the tuning[20]. For simplicity continuous tuning is chosen for use. Simplifying of the transfer functions to a first order system is required to use these methods.

For tuning of the inner current controller, modulus optimum can be used. When simplifying the open loop transfer function, it ends up with one dominant time constant from the RL circuit of the stator, and some time constants from filtering and converter switching that are considerably smaller. The smaller time constants can be approximated by a single time constant $T_{sum,inner}$, so that it becomes a first order system. Then the open loop transfer function, including the PI controller, is:

$$h_{0,MO}(s) = K_p \frac{1 + T_i s}{T_i s} K_s \frac{1}{1 + T_{1,inner} s} \frac{1}{1 + T_{sum,inner} s} \tag{5.25}$$

According to modulus optimum, the integral time constant (5.26) is chosen to be the same as the dominant time constant, so that the pole is cancelled. K_p (5.27) is selected so that the relative damping becomes $\frac{1}{\sqrt{2}}$ [16].

$$T_i = T_1 \tag{5.26}$$

$$K_p = \frac{T_1}{2K_s T_{sum,inner}} \tag{5.27}$$

When the system is tuned according to modulus optimum, the crossover frequency can be calculated from $T_{sum,inner}$. A high frequency means that the system is fast. The inner system should be fast, so that the cascaded control system can work well [16].

$$\omega_{c,i} = \frac{1}{\sqrt{2} T_{sum,inner}} \tag{5.28}$$

For the simplified transfer function of the outer speed controller (5.29), the process contains an extra integrator because of the rotating mass. Pole cancellation by modulus optimum, will in this case lead to a -180-degree phase shift, which gives a phase margin of 0. Instead, the speed controller can be tuned according to symmetrical optimum [19].

$$h_{0,SO}(s) = K_{p,n} \frac{1 + T_{i,n}}{T_{i,n}} K_s \frac{1}{T_{1,n} s} \frac{1}{1 + T_{sum,n} s} \tag{5.29}$$

When the outer system is simplified, according to the simplified open loop transfer function (5.29), the controller parameters can be calculated as below, according to symmetrical optimum [16].

$$T_i = 4 * T_{sum,n} \tag{5.30}$$

$$K_p = \frac{T_{1,}}{K_s * 2 * T_{sum,n}} \tag{5.31}$$

The crossover frequency for the speed controller is calculated as below, and should be approximately one decade lower than for the inner controller, so that the inner controller is considerably faster [16].

$$\omega_{c,n} = \frac{1}{2 * T_{sum,n}} \tag{5.32}$$

5.4 Tuning of inner loop current controller

For tuning the inner controllers it is required to find $T_{1,inner}$ and $T_{sum,inner}$ in the simplified open loop transfer function of the stator, given in (5.25). To find $T_{1,inner}$, it is needed to use the inductance and resistance of the stator. The stator inductance in the d- and q-axis is dependent on frequency, and is given in the Laplace frame below [11].

$$L_d(s) = L_d * \frac{(1 + s * T'_d)(1 + s * T''_d)}{(1 + s * T'_{d0})(1 + s * T''_{d0})} \tag{5.33}$$

$$L_q(s) = L_q * \frac{(1 + s * T'_q)(1 + s * T''_q)}{(1 + s * T'_{q0})(1 + s * T''_{q0})} = L_q * \frac{(1 + s * T''_q)}{(1 + s * T''_{q0})} \tag{5.34}$$

The expression for L_q (5.34) can be simplified, since $T'_q = T'_{q0} = 0$ for a salient pole machine. When applying a sudden change in the current, s will tend to infinity. Using the relations between the open circuit and short circuit time constants used in subsection 4.2.1, the inductance will be equal to the subtransient value, as shown below [11].

$$L_d(\infty) = L_d * \frac{(T'_d)(T''_d)}{(T'_{d0})(T''_{d0})} = L''_d \tag{5.35}$$

$$L_q(\infty) = L_q * \frac{(1 + s * T''_q)}{(1 + s * T''_{q0})} = L''_q \tag{5.36}$$

When a step in stator current is applied, currents will be induced in the damper windings, similar to an induction machine, which increases the resistance initially seen from the terminals. The contribution from the damper windings can be calculated the same way as in an induction machine [16], with 100% slip. This contribution can be calculated using the damper winding leakage factor (σ_D/σ_Q) and resistance (r_D/r_Q). This is added to the armature resistance, as shown in (5.39) and (5.40) [21] [22].

$$\sigma_D = \frac{x_{D\sigma}}{x_{ad}} \tag{5.37}$$

$$\sigma_Q = \frac{x_{Q\sigma}}{x_{aq}} \tag{5.38}$$

$$r'_{sd} = r_s + \frac{r_D}{(1+\sigma_D)^2} \tag{5.39}$$

$$r'_{sq} = r_s + \frac{r_Q}{(1+\sigma_Q)^2} \tag{5.40}$$

The control parameters are calculated according to modulus optimum, which was explained in subsection 5.3.3. $T_{sum,inner}$ is calculated as the sum of the filter time constant in measurements of the current, plus the time delay caused by the switching.

$$T_{sum,inner} = T_{f,i} + \frac{T_{sw}}{2} \tag{5.41}$$

The integral time constant is the same as the time constant for the electrical circuit L/R, where the values at the instant of a rapid transient is used. For the inner d- and q- axis controller, the control parameter values can be calculated as below.

$$T_{i,d} = T_{1,d} = \frac{x''_d}{\omega_n * r'_{sd}} \tag{5.42}$$

$$T_{i,q} = T_{1,q} = \frac{x''_q}{\omega_n * r'_{sq}} \tag{5.43}$$

$$K_{p,d} = \frac{x''_d}{2\omega_n * T_{sum,inner}} \tag{5.44}$$

$$K_{p,q} = \frac{x''_q}{2\omega_n * T_{sum,inner}} \tag{5.45}$$

5.4.1 Tuning of speed controller

For the outer loop, one needs to determine $T_{1,n}$, $T_{sum,n}$ and K_s in (5.29). The large time constant $T_{1,n}$, is equal to the mechanical time constant, which is calculated in section 4.4. The sum of the delays, $T_{sum,n}$, is calculated in (5.46), as the filter time constant for the speed measurements, plus the equivalent time constant of the inner system. When the current controller is tuned according to modulus optimum, the closed loop of the inner system can be simplified to a first order system, where the equivalent time constant is two times the delay in the inner system, $T_{eq} = 2 * T_{sum,inner}$ [23].

$$T_{sum,n} = T_{f,n} + 2 * T_{sum,inner} \tag{5.46}$$

In the model, the speed and position measurements are ideal. However, there will in reality be a time delay, since it is a digital decoder. In addition, some filtering of the speed measurement might be necessary in the lab set-up. The size of the time constant $T_{f,speed}$ in the filtering of the speed in the model, should therefore account for both the filtering and delay from the digital decoder and in the lab set-up.

The torque is equal to $\tau = i_q * \Psi_d + i_d * \Psi_q$ according to (5.19). When i_d is kept at zero by the inner system, the expression of the torque can be simplified to $\tau = i_q * \Psi_d$. Then, the d-axis flux linkage Ψ_d will be equal to the system gain K_S in the outer loop. A block diagram of an outer speed control loop is shown in Figure 5.3. The PI control parameters can be calculated as below.

$$T_{i,n} = 4 * T_{sum,n} = 4 * (T_{f,n} + 2 * T_{sum,inner}) \tag{5.47}$$

$$K_{p,n} = \frac{T_m}{2 * T_{sum,n} * \Psi_d} \tag{5.48}$$

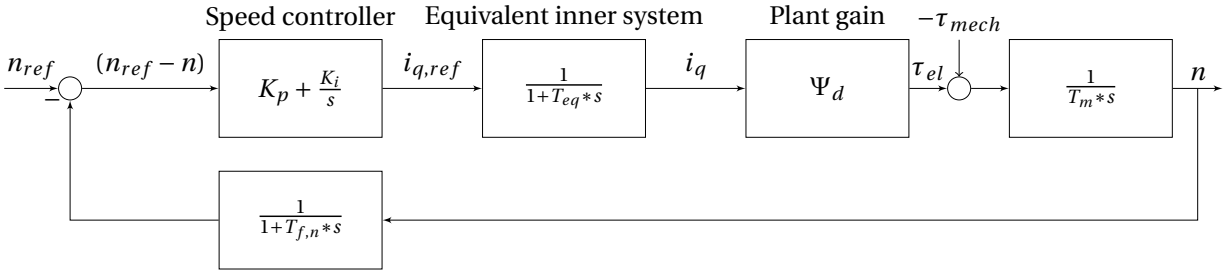

Figure 5.3: Block diagram with speed controller and inner system

5.5 Grid side converter

In the control system for a grid connected converter, it is common that $\omega t = 0$ for the dq frame is aligned 90 degrees behind phase a. This is opposite to the motor side, where $\omega t = 0$ is aligned with phase a. This causes that the d-axis current corresponds to active power, while i_q corresponds to reactive power [24] for the grid connected converter. The controllers of the grid side converter can be similarly tuned with modulus and symmetrical optimum as the machine side controllers [25].

Since the DC link voltage value will change if unbalance occurs in the active power flow of the two converters, the outer loop of the GSC can keep the DC link voltage constant by controlling the active power flow delivered to the grid. The reference for the d-axis current i_d is given to the inner current controller, based on the active power needed to maintain the DC link voltage at its reference. Then the large time constant in the outer loop is equal to the time constant of the DC link capacitor. The inner control system is quite similar to the machine side. The reactive power delivered to the grid can be controlled independently through i_q, which can be used to stabilise the grid voltage. The DC link voltage will be stable when the active power delivered from the DC link to the grid, is equal to the power which is delivered from the machine. A PLL (phase locked loop) can be used to get frequency and voltage angle measurements from the grid, and is important for synchronising the converter to the grid.[24]

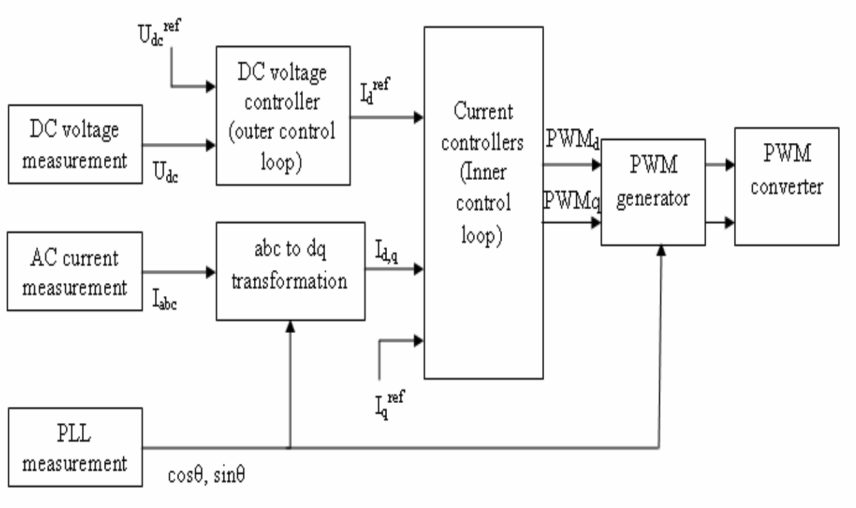

Figure 5.4: Functional control for a grid connected VSC [25]

Figure 5.4 shows a functional block diagram of a grid connected VSC which controls the DC link voltage. The principle of an outer DC link control loop is shown in Figure 5.5, while the principle of the inner control loop is shown in Figure 5.6. The L refers to the inductance between the AC grid and the converter.

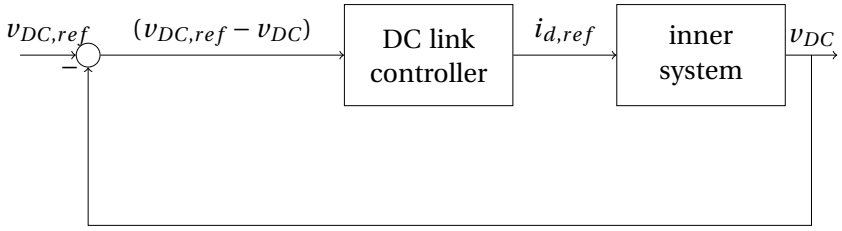

Figure 5.5: Outer control loop of a grid connected VSC

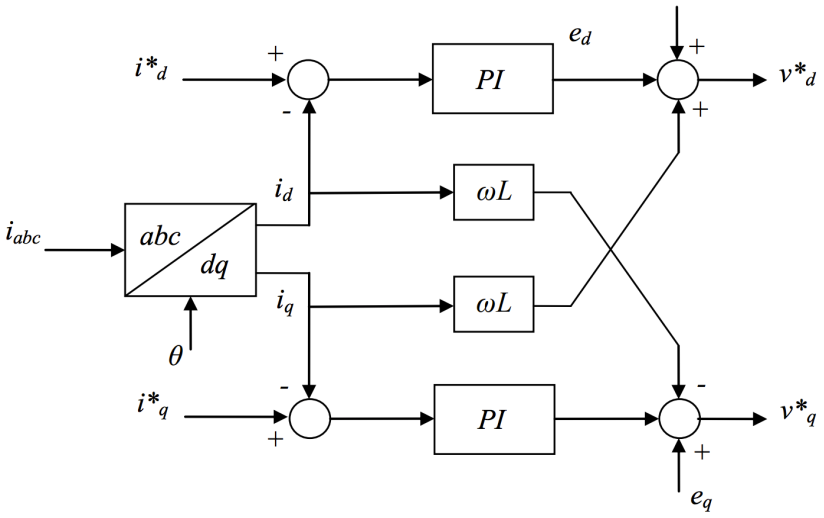

Figure 5.6: Inner control loop of a grid connected VSC [26]

From Figure 5.6, the decoupling terms in the inner current controller will be as below, modified for the different notation used.

$$v_{d,ref} = PI_d + \omega * l * i_q + v_{d,grid} \tag{5.49}$$

$$v_{q,ref} = PI_q - \omega * l * i_d + v_{q,grid} \tag{5.50}$$

Chapter 6

Simulation Model and Adjustable Speed Simulations

The purpose of the modelling and simulations in this chapter is to make a simulation model, which is representative of the equipment in the lab-set up. In this way, it is attempted to verify that the 20 kVA converter set-up is suitable for variable speed control of the synchronous machine in lab.

Grid side converter is fed by 400 V AC, which is controlling the DC-link voltage to be 600V DC. Machine side converter is converting 600 V DC to AC, and feeding the machine with variable voltage and frequency. The AC and DC voltage levels are chosen according to the present lab set-up. However, there are also possibilities to modify the lab set up, by connecting it to an AC grid voltage level which is similar to the voltage level of the machine, and lowering the DC link voltage accordingly.

An ideal mechanical load is used to control the mechanical torque, which can be controlled freely in both directions. In this chapter, it is only run at constant torque, or changed in steps. Some plots have various disturbances during the first tenth of a second which is caused by initial conditions in the simulations, and can be ignored.

6.1 Simulation model

The simulation model is made in Matlab/Simulink. The main structure of the motor controller was made with help from Ph.D student Abel Taffese, at the Department of Electrical Engineering at NTNU. In first step, the control system for the synchronous machine was developed in a simplified model. Here the machine is fed by an ideal variable voltage source, which delivers the frequency and voltage which is given from the control system. The control system contains an outer speed control loop, which gives the reference for i_q, as shown in Figure 5.3. The inner control system is similar to what is shown in Figure 5.2. It gets measurements of the currents in the stator and field winding, as well as the angel from the speed/position sensor. Thereby, it gives the voltage reference to the source to achieve the desired d- and q- axis currents, as shown in Figure 6.1.

In later steps, a 2L-VSC is added to the model to feed the machine from a DC source. In the last step, a grid-side converter is also implemented. The control structure of the inner and outer loops in the Simulink model are shown in Appendix E.

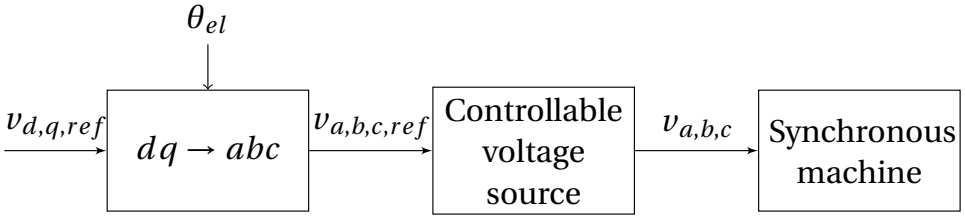

Figure 6.1: Voltage source loop

The electrical angle can be determined from the mechanical angle from the position sensor, by multiplying with the number of pole pairs in the machine: [18]

$$\theta_{el} = pp * \theta_{mech} \tag{6.1}$$

6.1.1 PI controllers

PI controllers from the Simulik library are used in the model. Saturation limits of ±1 are set for most of the controllers, so that their saturation limits correspond to the rated values. An anti-wind up strategy called clamping is chosen for the controllers.

6.1.2 Machine model

The machine is modelled by using the machine model *Synchronous Machine Salient Pole (standard)* from the Simscape Power Systems library in Simulink. Its parameter values are defined from the power ratings, as well as the found impedances and time constants. For simplicity, the machine is modelled as unsaturated. This is accurate enough, since the machine is operated at constant field current of 2.6 A. The saturation level would thereby be constant for the physical machine. The induced voltage voltage in the machine model is thereby according to the modified air gap line in Figure 3.18 in section 3.8, which is very close to the actual machine characteristics in the area around the chose operation point.

The rated input values for the machine model which is used is the rated apparent power, voltage, pole pairs and frequency. In addition, the field current which induces rated terminal voltage at no load, is defined to be 2.6 A. The rest of the input is given in Table 6.1 in per unit. The zero sequence reactance is not discussed earlier, and is not very important, since it will only be relevant during unbalanced faults. However, it is set to half of the d-axis subtransient reactance, which is assumed to be a realistic value for the actual machine.

Table 6.1: Synchronous machine model input

Explanation	Symbol	Value
Stator resistance	r_s	0.036
Stator leakage reactance	$x_{s\sigma}$	0.064
d-axis synchronous reactance	x_d	0.644
q-axis synchronous reactance	x_q	0.423
zero-sequence reactance	x_0	0.04
d-axis transient reactance	x'_d	0.218
d-axis subtransient reactance,	x''_d	0.083
q-axis subtransient reactance,	x''_d	0.125
d-axis transient time constant	T'_d	0.069 s
d-axis subtransient time constant	T''_d	0.0062 s
q-axis subtransient time constant	T''_d	0.0093 s

6.2 Simulations with a controllable voltage source

The simulations are run with a digital sampling time of $T_s = 1/20kHz = 20\mu s$. It is also possible to run the simulations in continuous time in Simulink. However, the run time of the simulations is much faster with a discrete simulation.

Since the voltage waveforms are perfectly sinusoidal, there are be no voltage ripple from switching, and thereby no ripple in the current either. Filtering of the current measurements is however done, to make the model more similar to the real system. The same is done with the speed/position measurements.

To simulate the time delay from the switching of a VSC, a time delay is added in the reference to the ideal voltage source. The time delay $T_{v,delay}$ is set to 150μs. This is shown in Figure 6.2.

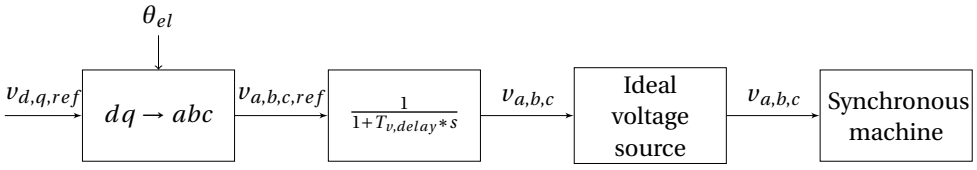

Figure 6.2: Time delay added to the ideal voltage source

6.2.1 Calculation of control parameter values

The control parameter values are calculated according to procedure described in section 5.4.

$$\sigma_D = \frac{x_{D\sigma}}{x_{ad}} = \frac{0.022}{0.58} = 0.0379 \tag{6.2}$$

$$\sigma_Q = \frac{x_{Q\sigma}}{x_{aq}} = \frac{0.073}{0.36} = 0.203 \tag{6.3}$$

$$r'_{sd} = r_s + \frac{r_D}{(1+\sigma_D)^2} = 0.036 + \frac{0.035}{(1+0.0379)^2} = 0.068 = 1.89 * r_s \tag{6.4}$$

$$r'_{sq} = r_s + \frac{r_Q}{(1+\sigma_Q)^2} = 0.036 + \frac{0.065}{(1+0.203)^2} = 0.081 = 2.25 * r_s \tag{6.5}$$

$$T_{i,d} = T_{1,d} = \frac{x''_d}{\omega_n * r'_{sd}} = \frac{0.083}{100 * \pi * 1.89 * 0.036}[s] = 3.88 * 10^{-3} s \tag{6.6}$$

$T_{sum,inner}$ is found by adding the delay in the voltage source, to the filter time constant.

$$T_{sum,inner} = T_{fi} + T_{v,delay} = 300\mu s + 150\mu s = 450\mu s \tag{6.7}$$

From this, the gain can be calculated:

$$K_{p,d} = \frac{x''_d}{2\omega_n * T_{sum,inner}} = \frac{0.083}{2 * 100 * \pi * 4.5 * 10^{-4}} = 0.293 \tag{6.8}$$

The integral gain is thereby found:

$$K_{i,d} = \frac{K_{pd}}{T_{id}} = \frac{0.293}{3.88 * 10^{-3}} = 75.5 \tag{6.9}$$

The calculations for the q-axis controller is done similarly, using the resistance found in (5.40).

$$T_{i,q} = \frac{x''_q}{\omega_n * r'_{sq}} = \frac{0.125}{100 * \pi * 2.25 * 0.036} = 4.91 * 10^{-3} s \tag{6.10}$$

$$K_{p,q} = \frac{x''_q}{2\omega_n * T_{sum,inner}} = \frac{0.125}{2 * 100 * \pi * 4.5 * 10^{-4}} = 0.44 \tag{6.11}$$

$$K_{i,d} = \frac{K_{pd}}{T_{id}} = \frac{0.44}{4.91 * 10^{-3}} = 90.1 \tag{6.12}$$

Outer speed control variables

The filter time constant of the speed measurement $T_{f,n}$ is set to 0.005 s. This affects how fast the outer loop will be. The speed controller should be significantly slower than the inner loop. This can be examined by looking at the crossover frequencies of the two systems. From the calculations below in (6.17) and (6.18), it can be seen that the crossover frequency of the speed controller is in the range of a tenth of the frequency of the current controller, which means they are suitably fast compared to each other [16].

$$T_{sum,n} = T_{f,n} + 2 * T_{sum,inner} = 0.005 + 2 * 4.5 * 10^{-4} = 5.9ms \tag{6.13}$$

Then the speed control values can be calculated:

$$T_i = 4 * T_{sum,n} = 0.0236s \tag{6.14}$$

$$K_p = \frac{T_m}{Psi_d * 2 * T_{sum,n}} = \frac{0.41}{1 * 2 * 5.9 * 10^{-3}} = 34.75 \tag{6.15}$$

$$K_i = \frac{K_p}{T_i} = 1472 \tag{6.16}$$

Then the crossover frequencies of the the inner and outer system can be calculated.

$$\omega_{c,i} = \frac{1}{\sqrt{2} * 2 * T_{sum,inner}} = \frac{1}{\sqrt{2} * 2 * 4.5 * 10^{-4} s} = 785.6 rad/s \tag{6.17}$$

$$\omega_{c,n} = \frac{1}{2 * T_{sum,n}} = \frac{1}{2 * 5.94.5 * 10^{-3} s} = 84.7 rad/s \tag{6.18}$$

6.2.2 Field controller

The field controller is tuned according to modulus optimum, similar to the inner current controller. The task of the field controller is to keep the field current constant at 2.6A, also during rapid changes in stator, which tends to induce currents in the field winding.

The field is fed by a DC source. In reality, a converter of some kind will feed the field circuit. To make the voltage source more realistic, a time delay is added between the voltage reference and the voltage source. A block diagram of the control loop is provided in Figure 6.3.

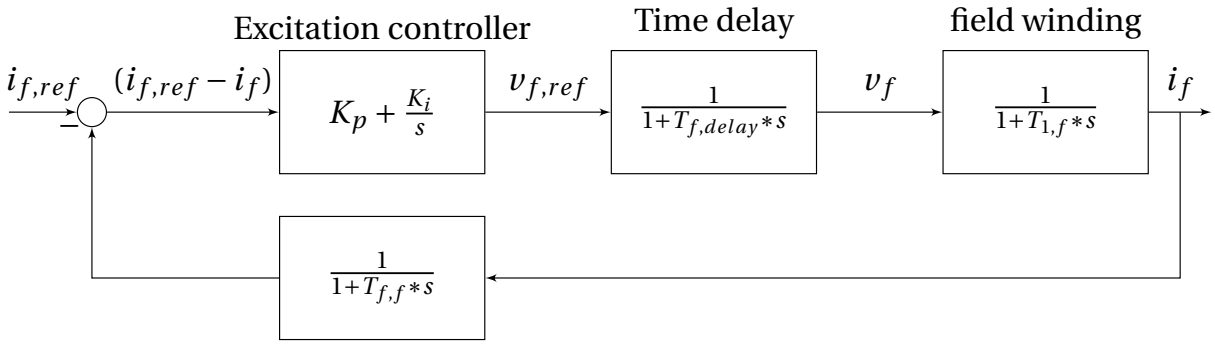

Figure 6.3: Block diagram of field circuit control loop

The field current controller is tuned according to modulus optimum, similar to the inner current controller, by using the leakage reactance, and adding the effect of the d-axis damper winding from (5.39) to the resistance:

$$T_{sum,f} = T_{f,f} + T_{fv,delay} \tag{6.19}$$

$$T_{i,f} = T_{1,f} = \frac{x_{f\sigma}}{\omega_n * (r_f + \frac{r_D}{(1+\sigma_D)^2}} = \frac{x_{f\sigma}}{\omega_n * (r_f + 0.9 * r_s)} \tag{6.20}$$

$$K_{p,d} = \frac{x''_d}{2\omega_n * T_{sum,f}} \tag{6.21}$$

The filtering time constant $T_{f,f}$ of the current measurements is set to 200μs, while the delay $T_{fv,delay}$ is set to 500 μs. Then the field control parameters is calculated:

$$T_{sum,f} = 200\mu s + 500\mu s = 700\mu s \tag{6.22}$$

$$T_{i,f} = \frac{0.21}{100 * \pi * (0.012 + 0.9 * 0.036)} = 0.015s \tag{6.23}$$

$$K_{p,f} = \frac{0.21}{100 * \pi * 7.0 * 10^{-4}} = 0.954 \tag{6.24}$$

$$K_{i,f} = \frac{0.954}{0.015} = 63.6 \tag{6.25}$$

6.2.3 Testing of field and inner current controller

The inner current controllers and the field controller were tested independently. When performing the tests, the initial speed was set to zero, and the gains of all the other controllers set to zero. The inertia was also increased, to keep the speed close to zero, when testing the q-axis controller. The field circuit was short circuited during the test of the current controllers. These actions were done to minimise coupling between the circuits.

According to modulus optimum, it is expected that the overshoot is 4.7%, while the settling time is $8 * T_{sum}$ [16], which is $8 * 0.45ms = 3.6ms$ for the current controllers, when a step in reference is applied. It is seen from Figure 6.4 and Figure 6.5, that the overshoot is 5% and 4%, while the settling time is 3.5ms and 4.5ms, which complies well with the mentioned expectations.

Regarding the field circuit, the maximum voltage is set to 400 V, which corresponds to 7.54% of the field base voltage, which was calculated in subsection 4.6.2. The saturation limit of the controller is set accordingly. The controller quickly goes to saturation when a step of 1 pu is applied, as in Figure 6.6. However, it reaches the new value after 20ms. Since the controller goes to saturation during the step, it does not have the typical overshoot, which is seen for the inner current controllers. It also uses longer time to reach the reference than $8 * T_{sum,f}$.

It was observed that a field voltage of 113V is needed to maintain the rated 2.6A field current in the model. This corresponds to a resistance of $113V/2.6A = 43.5\Omega$, which corresponds well with

the calculated value in subsection 4.6.2.

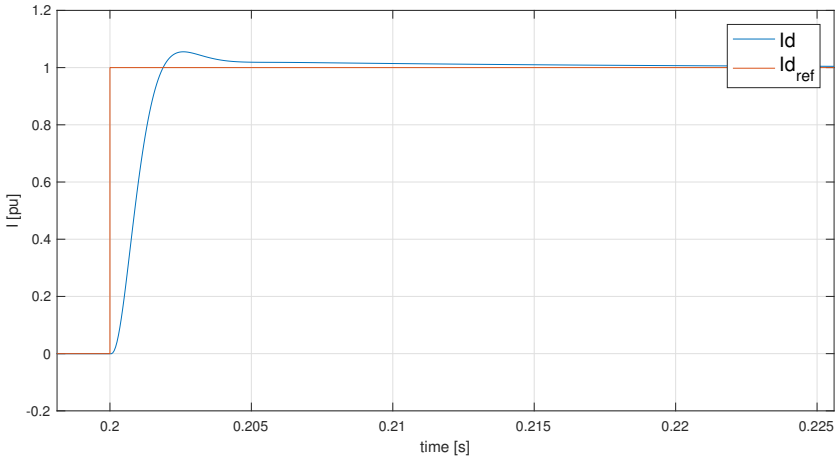

Figure 6.4: Step response of d-axis current controller, with 5% overshoot and 4.5ms settling time

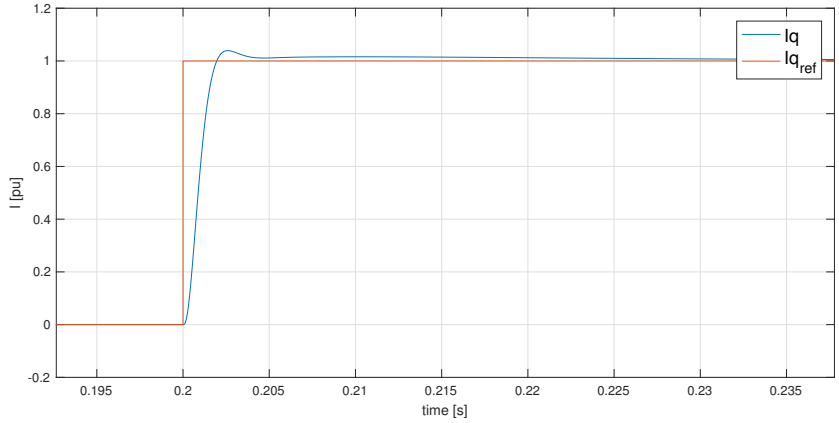

Figure 6.5: Step response of q-axis current controller, with 4% overshoot and 3.5 ms settling time.

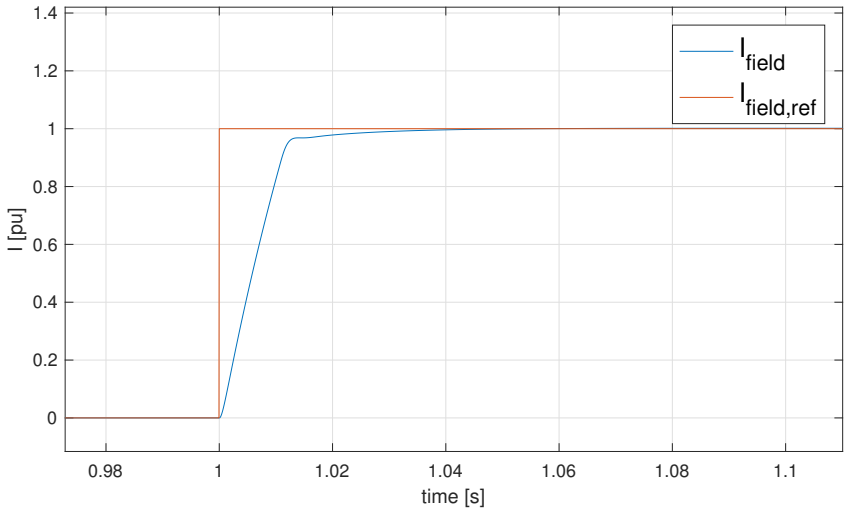

Figure 6.6: Step response of field current controller, with a settling time of 20ms

6.2.4 Simulation with step in speed

A step in speed is simulated in no load. As seen in Figure 6.7, the speed has some overshoot before it stabilises on the new reference value. Figure 6.8 and Figure 6.9 also shows that the torque q-axis current reference almost immediately goes to saturation. Consequently, the q-axis current, and thereby also the electrical torque, gets some overshot. Figure 6.10 shows that a considerably large current is induced in the d-axis during the speed. The field current is also influenced, as seen in Figure 6.11.

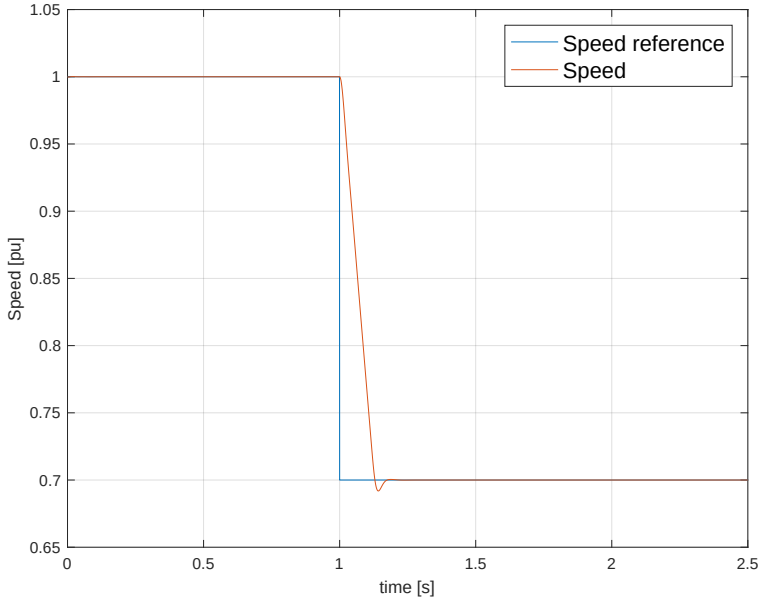

Figure 6.7: Step in speed during no load

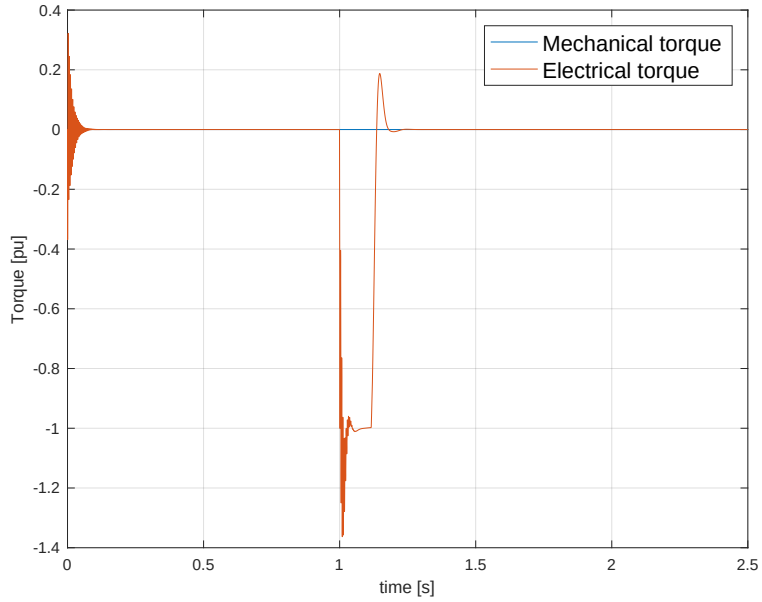

Figure 6.8: Electrical and mechanical torque during a step in speed

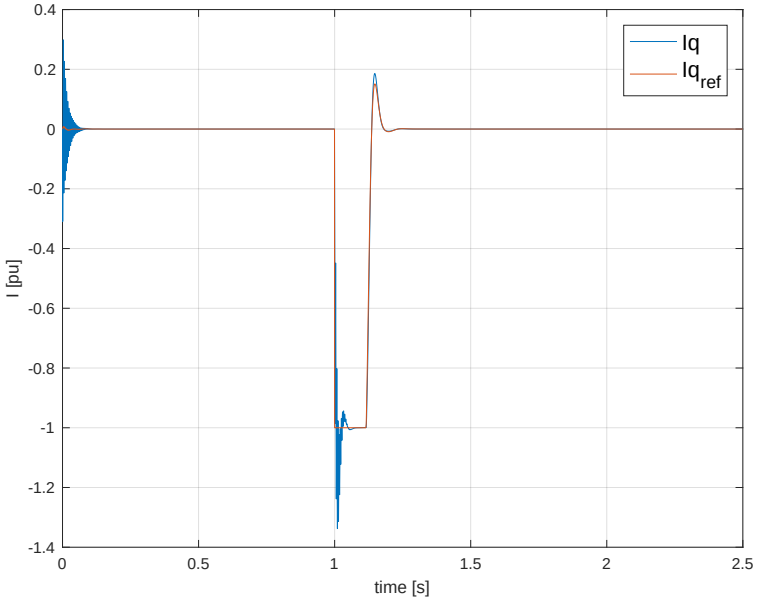

Figure 6.9: q-axis current during speed sped

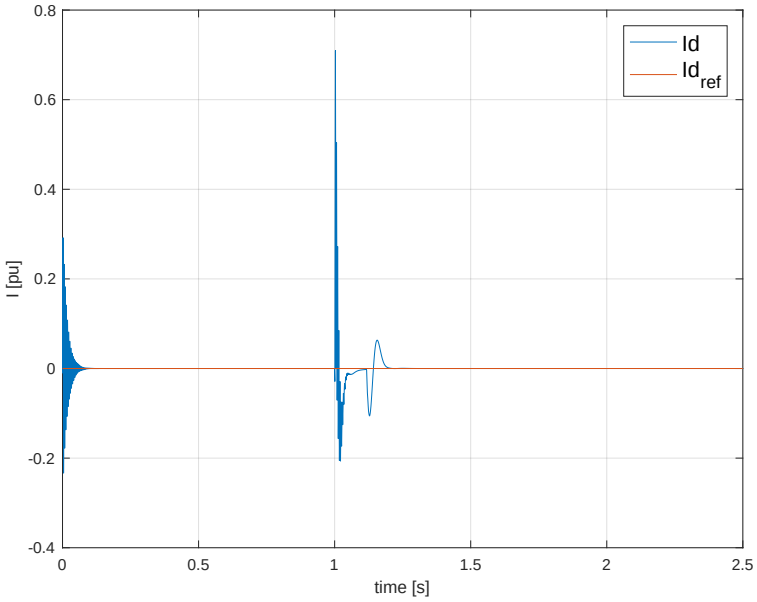

Figure 6.10: d-axis current during speed step

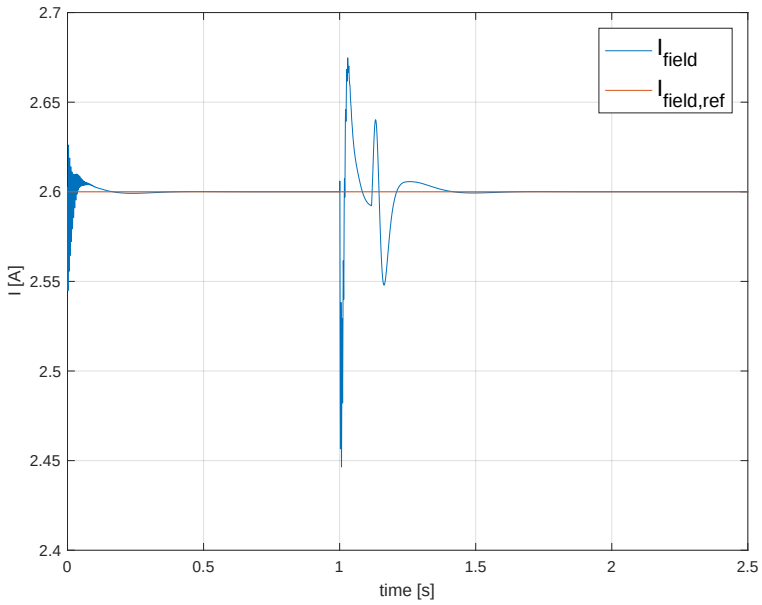

Figure 6.11: The field current during a sharp sted in speed

6.2.5 Simulation with filtering of the speed reference

To avoid the speed from overshooting, filtering of the speed reference is applied. By filtering the speed reference with a filter with time constant 0.1s, the overshoot is removed, as seen in Figure 6.12. The overshoot in q-axis current is also reduced, according to Figure 6.14. The d-axis current and the field current is also less influenced, compared to when a sharp step is applied.

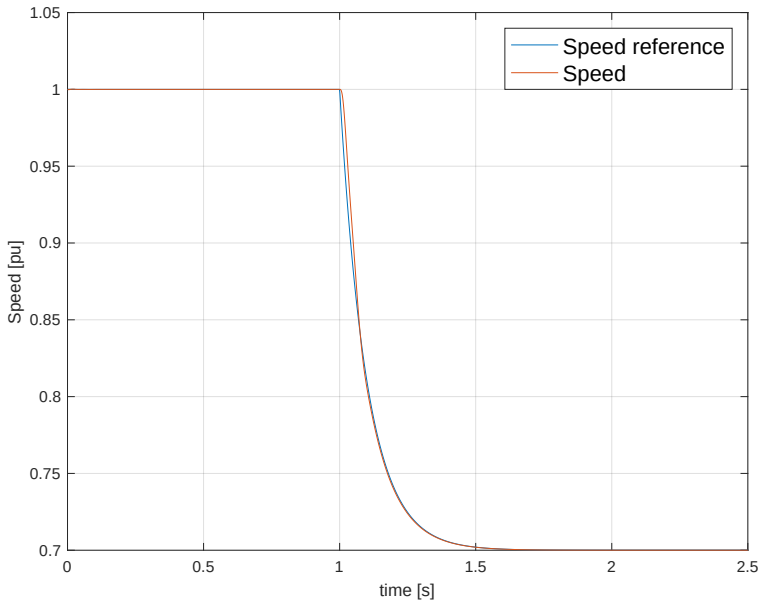

Figure 6.12: Speed and speed reference during filtered speed step

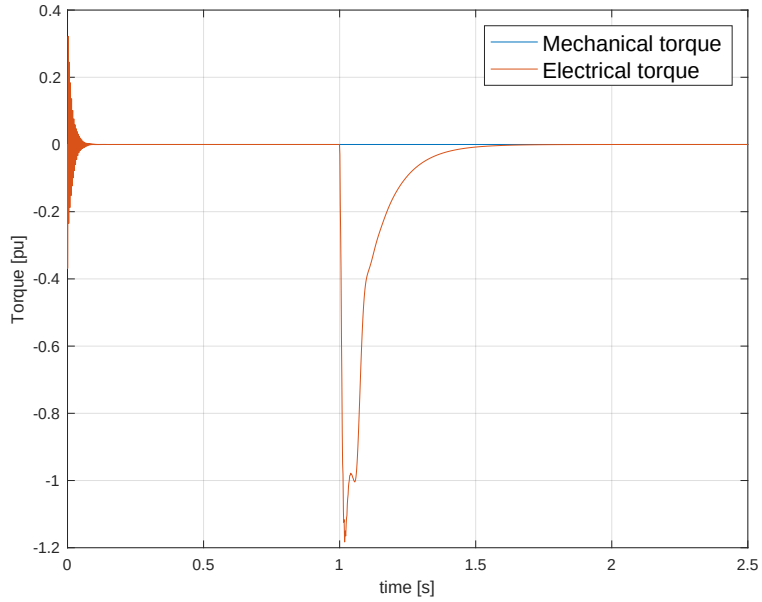

Figure 6.13: Electrical and mechanical torque during a step in speed

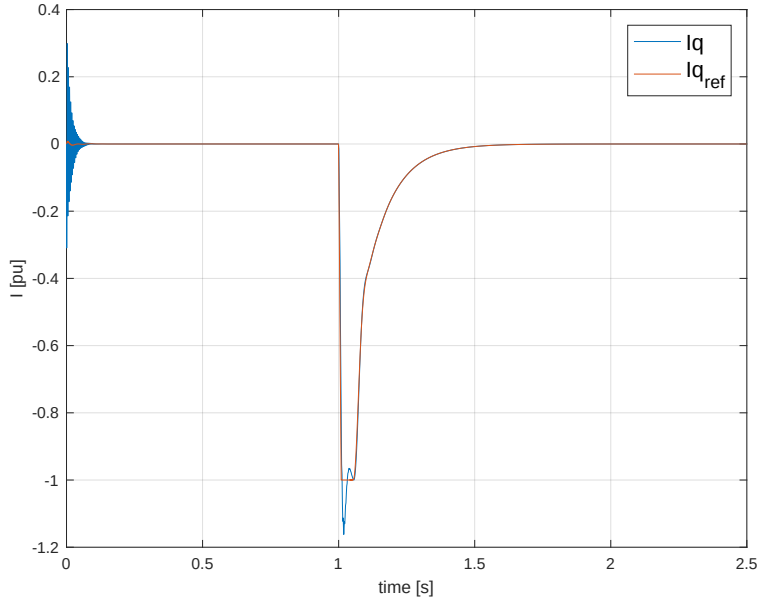

Figure 6.14: q-axis current during filtered speed step

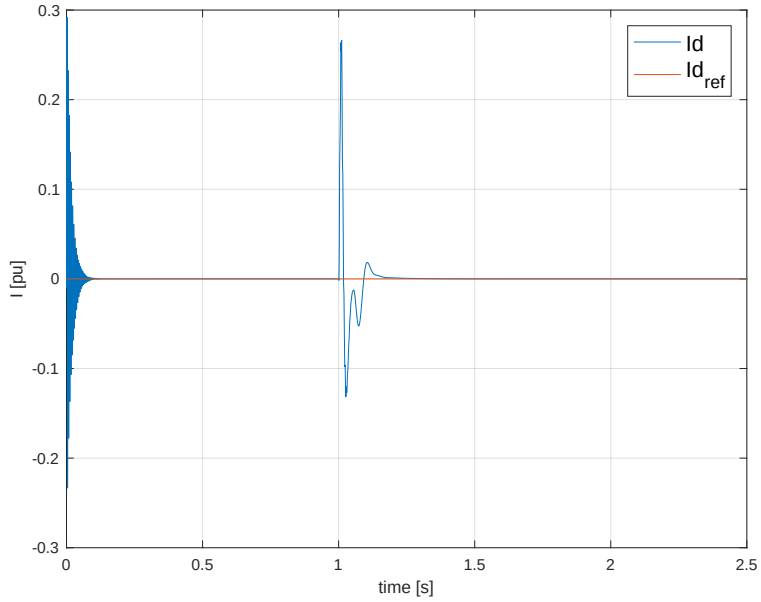

Figure 6.15: d-axis current during filtered speed step

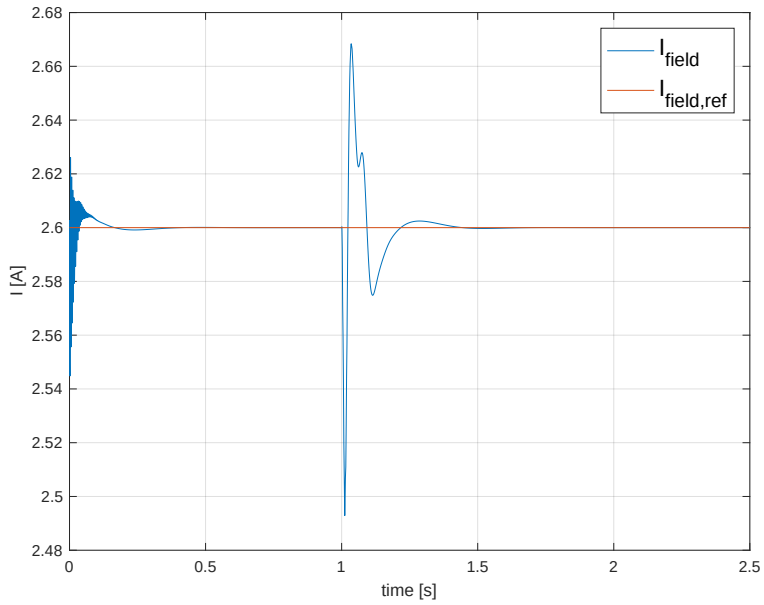

Figure 6.16: Field current during filtered speed step

6.3 Simulation with step in torque and speed

In the next step, a step in load torque at 0.7 in the rotating direction is applied after 1s, so that the machine becomes a generator. The same step in speed after 2s is applied, which is filtered as in the prior section, with a time constant of 0.2s. Such a sharp step in torque may not be realistic for hydropower applications, but is nevertheless done to test the control system.

Figure 6.19 shows that the speed controller is giving the required torque reference to the inner controller within 20ms, as the speed rises as seen in Figure 6.17. The inner controller has no problem to follow the torque reference set by the outer loop, though it overshoots by a few percent, similar as in the test in subsection 6.2.3. Overall, the system is acting fast on the sudden change in mechanical torque, and only 2% increase in speed is observed. The speed and torque stabilise on the reference within 0.1-0.2 after the torque step.

From Figure 6.17, it can be seen that the speed is not perfectly following the reference, as it does in Figure 6.12. This occurs because the machine is using 70% of its torque capabilities on the

mechanical, and has less available torque to change the speed. However, it stabilises on the new reference after 0.5s, without any considerable overshoot.

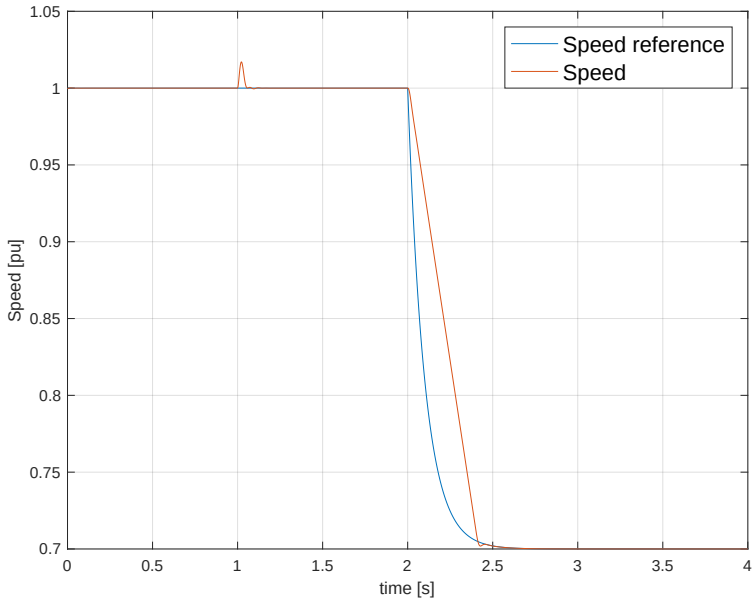

Figure 6.17: Speed and speed reference during step in torque and filtered speed step

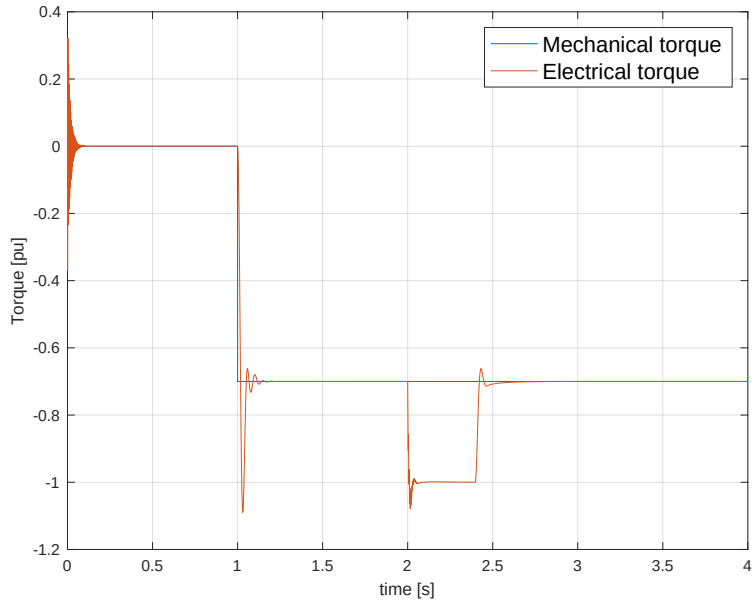

Figure 6.18: Electrical and mechanical torque during step in torque and filtered speed step

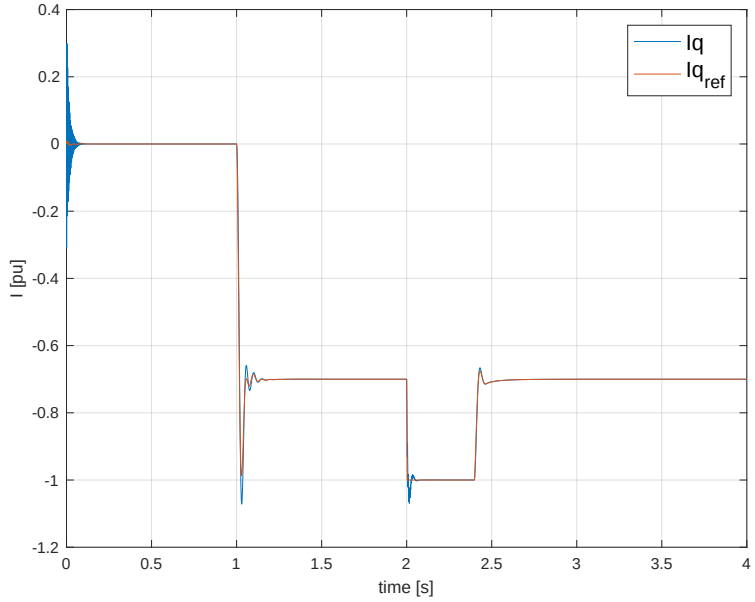

Figure 6.19: q-axis current during step in torque and filtered speed step

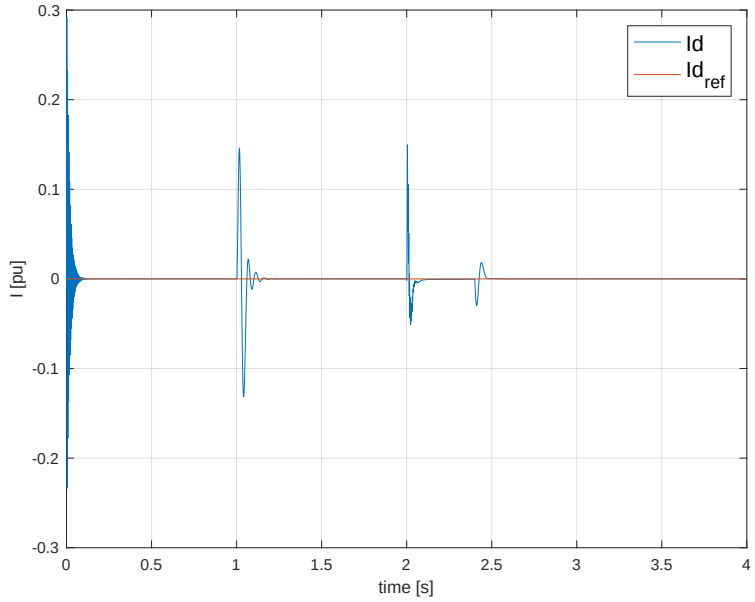

Figure 6.20: d-axis during step in torque and filtered speed step

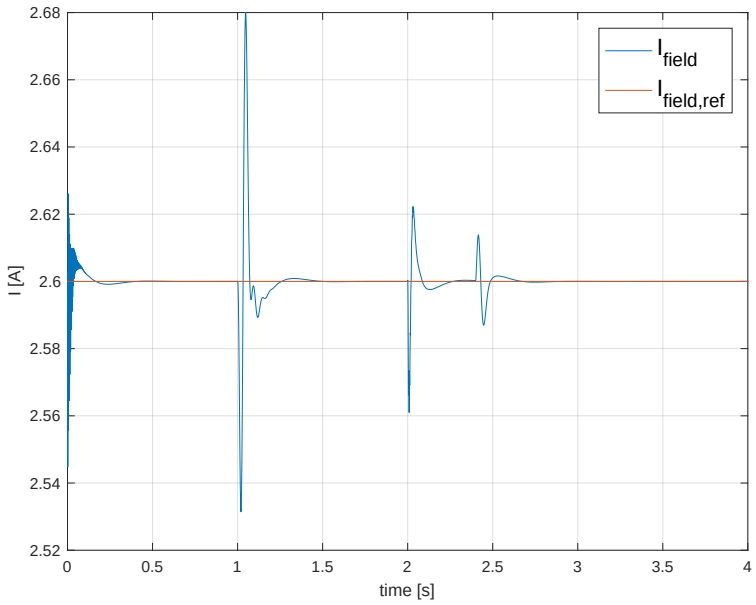

Figure 6.21: Field current during step in torque and filtered speed step

For the rest of this chapter, and in Appendix F, all the simulations are done with same speed reference and load torque as done in this section.

6.4 Model with voltage source converter with DC source as DC link

In next step, the machine side 2L-VSC is implemented in the model. In this case, the voltage reference is sent to the PWM generator, which generates signals that control the switches in the converter. The DC link is replaced by a 600 V DC source, which is feeding the motor side converter. Sinusoidal PWM is used to control the switches in the converter.

The system is simulated in discrete time, with a sampling time of 2.5μs. This is done to a have high enough resolution in the PWM modulation and the switching. A switching frequency of 4 kHz is chosen, which means it will be a resolution of 100 samples for each switching period. A disadvantage of choosing a low sampling time for the system is that the run time of the simulations

increases. With the low sampling time, the controllers will behave more similar to continuous controllers, compared to running the systems with higher sampling time.

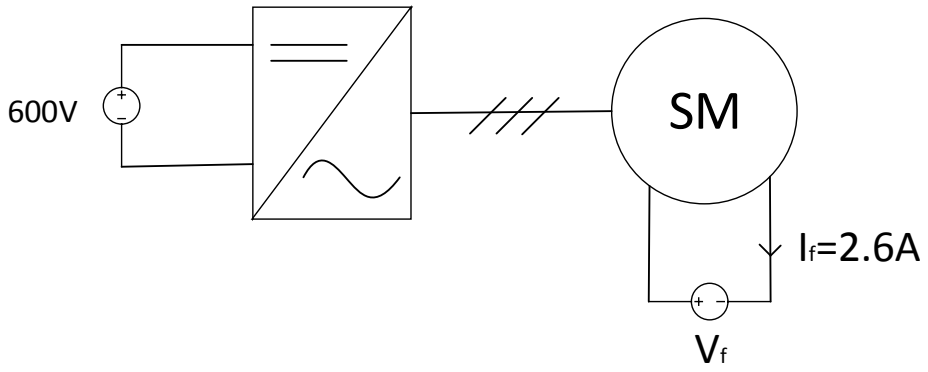

Figure 6.22: Converter with DC link modelled as a DC source

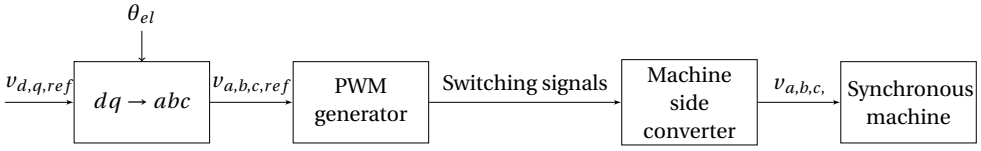

Figure 6.23: A PWM converter as voltage source

6.4.1 LCL filter

The back-to-back converter in the lab setup has an LCL filter installed on either side, as can be seen in Figure 2.1. The inductances are series connected, while the capacitor is star connected, and has the data given below [27]. The LCL filter is inserted in the model between the converter and the machine, to make the model similar to the lab setup.

Converter side inductor: L_{conv} = 1mH

Filter capasitor: C_{LCL} = 25μF

Output side inductor: L_{out} = 0.6mH

Their reactances become:

$$X_{L,conv} = \omega_n * L_{LCL,conv} = 100\pi/s * 1mH = 0.314\Omega = 0.052pu \tag{6.26}$$

$$X_C = \frac{1}{\omega_n * C_{LCL}} = \frac{1}{100\pi * 25\mu} = 127\omega = 21pu \tag{6.27}$$

$$X_{L,out} = \omega_n * L_{LCL,conv} = 100\pi * 0.6mH = 0.188\Omega = 0.031pu \tag{6.28}$$

$$\tag{6.29}$$

The documentation[27] does not mention anything about the resistance in the inductors. However, it is assumed to be in the area 20-50mΩ, and is set to be 30mΩ in the model, distributed by half on each inductor. The series connected impedances from the LCL filter must be accounted for in the calculations of the inner current controller. The resistance is added to the stator resistance, while the reactances from the inductors are added to the subtransient reactance. The star connected capacitor is for simplicity neglected in this context.

$$x_{LCL} = 0.052 + 0.031 = 0.083pu \tag{6.30}$$

$$r_{LCL} = 20m\Omega = 0.005pu \tag{6.31}$$

$$T_{i,inner} = \frac{x'' + x_{LCL}}{\omega_n * (r' + r_{LCL})} \tag{6.32}$$

$$K_{p,inner} = \frac{x'' + x_{LCL}}{2\omega_n * T_{sum,inner}} \tag{6.33}$$

The simulation results from using the LCL filter are given in section F.1 in the appendix. It was observed that a large filter time constant in the inner loop was needed for stable q-axis current.

6.4.2 Synchronous sampling

It is attempted to implement synchronous sampling in the model. The controller will sample measurements every 2.5 μs. However, a block is implemented, which freezes the measurements

at each top and bottom of the triangular modulation curve. However, there are some harmonics in the current at approximately 1 kHz. This is probably because of the LCL filter, which has a resonant frequency of 1 kHz [27]. The synchronous sampling does not take away these oscillations from the sampling, as seen in Figure 6.24 and Figure 6.25, which is taken from the simulation in **??**.

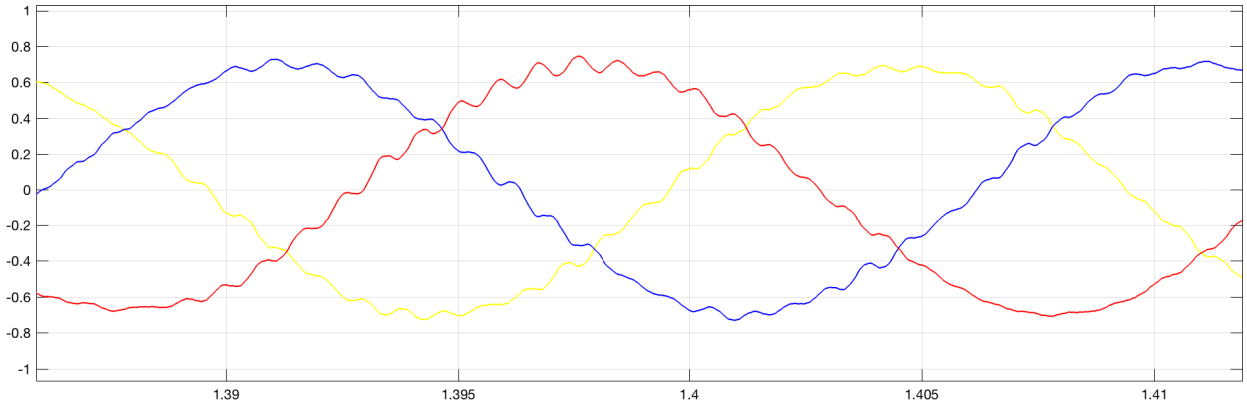

Figure 6.24: An excerpt from the abc current from the synchronous machine

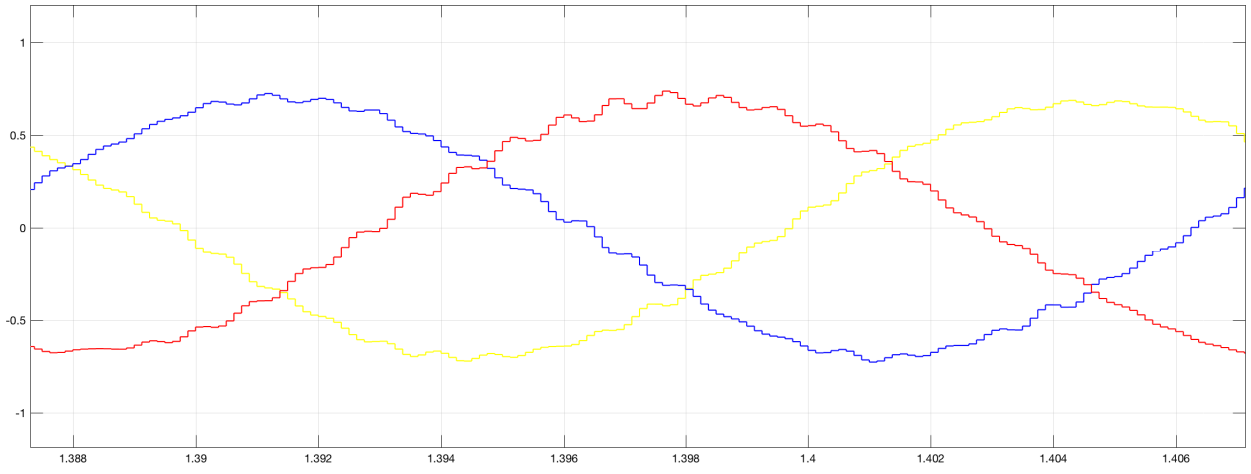

Figure 6.25: The abc current from stator measured at top and bottom of the modulation signal, showing the sampling of the firs waves in Figure 6.24

6.5 Modelling without the LCL filter

Apparently, the 1kHZ oscillations caused by the LCL filter tend to disturb the current controller. A large filter time constant was needed to dampen them in the feedback of the inner controller. This leads to a slower inner control loop, which is not desirable. Since the LCL filter was causing those problems, it was removed from the model. An LCL filter is normally not needed on the motor side of a converter [28]. It is also possible to disconnect it from the back to back converter in the lab set-up [29].

A simulation without the LCL filter is presented in section F.2 in the appendix, where the current is sampled each 2.5μs.

Synchronous sampling without the LCL filte

In the simulations without the LCL filter on the machine side of the converter, better effect is seen from implementing synchronous sampling. The simulations with synchronous sampling without the LCL filter are presented in section F.3 in the appendix.

The current waves from the machine contains ripples in the current, as seen in Figure 6.26. The discrete sampling of the same current waves is shown in Figure 6.27. In this case, the purpose of synchronous sampling is functioning in the model, by avoiding the ripple to be measured. It does not remove the ripple, but prevents it from affecting the controller. A smaller filter time constant for the current measurements can be used when sampling in this way.

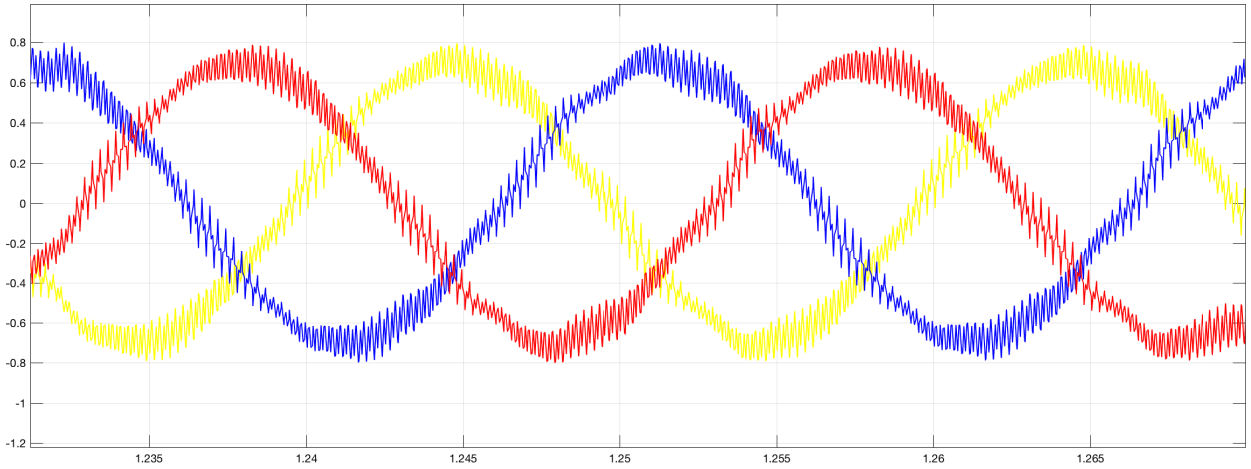

Figure 6.26: An excerpt from the abc current from the synchronous machine from one of the simulations in section F.3

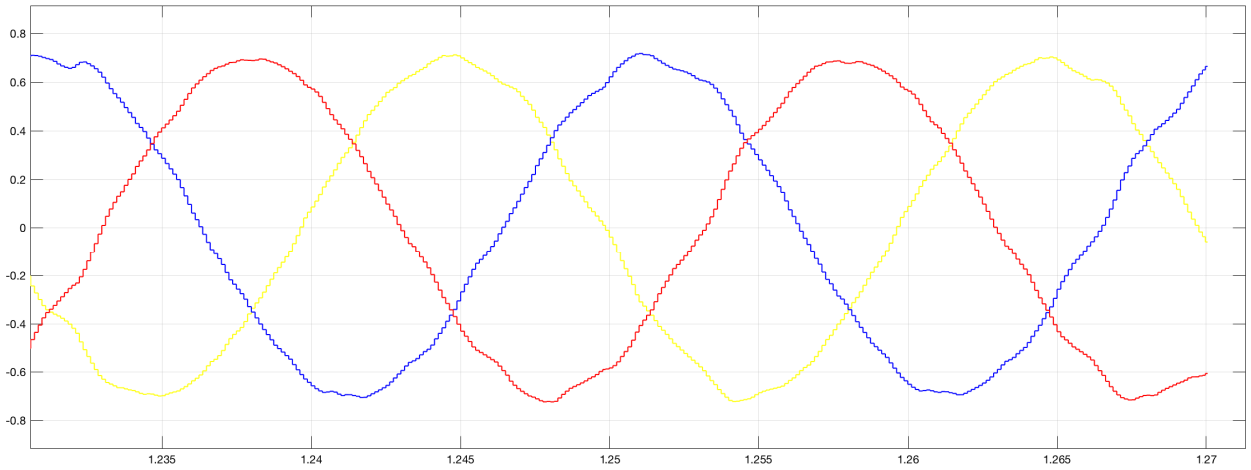

Figure 6.27: The abc current from stator sampled at top and bottom of the PWM modulation signal, showing the sampling of the waves in Figure 6.26

6.6 Model including a grid side converter

The task of the grid side converter to is monitor and control the DC link to be 600 V. The same LCL filter as described in subsection 6.4.1, is between the converter and the pint of common coupling (PCC). The gird is modelled as a stiff 400 V AC source, with a grid impedance and of $1\mu\Omega$ and 1μH in series between the voltage source and the PCC.

A PLL is connected to the PCC, and is used to find the electrical angle which is needed for park and inverse park transformation, so that the grid converter can be synchronised with the grid. The structure of the control system of the GSC can be seen in Appendix E

6.6.1 Space vector PWM

A simple approach of PWM modulation is implemented in the grid side converter, by taking the mean of the maximum and minimum instantaneous values of the abc voltage reference, and subtracting it from the sinusoidal signal. The implementation simulates the effect of SVPWM, by creating SVPWM control waveforms [18]. The implementation is shown in Figure 6.28, while the control waveform generated, which goes to PWM modulator, is shown in Figure 6.29. The main advantage of doing this is to to invert higher AC voltage from the same DC link voltage, compared to sinusoidal PWM.

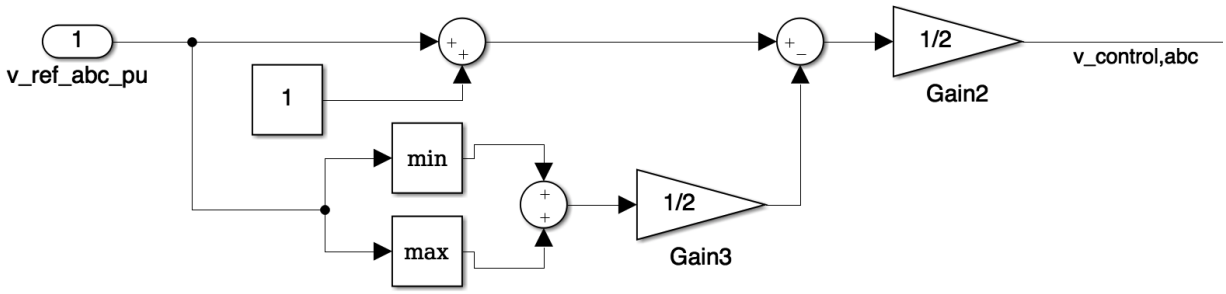

Figure 6.28: Changing the shape of the control signal, with third harmonics injection/SVPWM

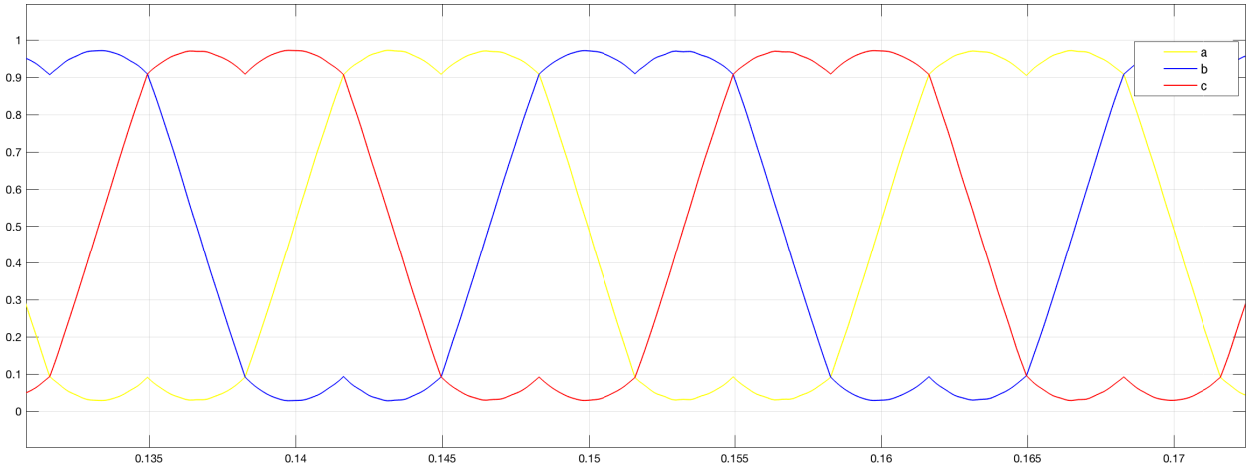

Figure 6.29: Reference waveforms from SVPWM in the GSC

6.6.2 Calculation of control parameter values for GSC

For the control system for the grid-side converter, the per unit quantities are determined by the voltage level on the grid and the power rating of the converter. The calculations of the grid-side and DC link per unit values can be seen in Appendix A.

Inner control system

First, the per unit reactance and resistance in the LCL filter must be calculated, using the grid side quantities.

$$x_{LCL,GSC} = \frac{X_{LCL}}{Z_{c,base}} = \frac{0.314\Omega + 0.188\Omega}{8.0\Omega} = 0.0628pu \tag{6.34}$$

$$r_{LCL,GSC} = \frac{X_{LCL}}{Z_{c,base}} = \frac{0.314\Omega + 0.188\Omega}{8.0\Omega} = 0.0628pu \tag{6.35}$$

Since the inductance of the LCL filter is symmetrical, the properties of d- and q-axis controllers will be equal, and can be calculated as below:

$$T_{i,GSC} = T_{1,GSC} = \frac{x_{LCL}}{\omega_n * r_{LCL}} \tag{6.36}$$

$$\tag{6.37}$$

$$T_{sum,GSC,inner} = T_{f,i} + \frac{T_{sw}}{2} \tag{6.38}$$

$$K_{p,GSC,inner} = \frac{x_{LCL}}{2\omega_n * T_{sum,GSC,inner}} \tag{6.39}$$

$$K_{i,GSC,inner} = \frac{K_{p,GSC,inner}}{T_{i,GSC}} \tag{6.40}$$

Outer control system

For the outer loop, it is needed to find the large time constant, which is the DC capacitor time constant. As each of the converters has a DC link capacitor bank of 3300μF [30], the total DC link capacitance is 6600μF. The time constant is calculated by using the base impedance on the DC link [25].

$$T_{C,DC} = C_{DC} * Z_{DC,base} = 6600\mu F * 18\Omega = 0.1188s \tag{6.41}$$

$$\tag{6.42}$$

Since a 1 pu output from the DC controller will set the active power reference to 1 pu, the plant gain $K_{s,DC} = 1$.

The the DC controller gains can be calculated accordingly:

$$T_{i,DC} = 4 * (T_{f,DC} + 2 * T_{sum,GSC,inner}) \tag{6.43}$$

$$K_{p,DC} = \frac{T_m}{2 * T_{sum,DC}} \tag{6.44}$$

$$K_{i,DC} = \frac{K_{p,n}}{T_{i,DC}} \tag{6.45}$$

6.7 Simulation including the GSC

The grid-side converter is simulated, while doing the same changes in torque and voltage, as in the prior simulations. The system can be simulated both with and without synchronous sampling. It is chosen to present one simulation, with synchronous sampling of both the machine and grid side. The filter time constant is set to 100mus. The DC link filter time constant is set to 500mus. The system sampling time was $Ts = 2.5\mu s$ and the switching frequency to 4 kHz, as in the simulations in Appendix F. The controller gains are calculated according to the presented method, and are presented below.

Machine side control properties:
Current filter time constant: $T_{f,i} = 100\mu s$
Speed filter time constant: $T_{f,n} = 5ms$
d-axis current controller gain: $K_{p,d} = 0.62$
d-axis current controller integral gain: $K_{i,d} = 86.3$
q-axis current controller gain: $K_{p,q} = 0.78$
q-axis current controller integral gain: $K_{i,q} = 101$
Speed controller gain: $K_{p,n} = 60.6$
Speed controller integral gain: $K_{i,n} = 2589$
Current controllers crossover frequency: $\omega_{c,i} = 1563rad/s$
Speed controller crossover frequency: $\omega_{c,n} = 91.7rad/s$

Grid side control properties:

Current filter time constant: $T_{f,i} = 100\mu s$

DC link filter time constant: $T_{f,DC} = 500\mu$

Inner current controllers gain: $K_{p,d} = 0.62$

Inner current controllers integral gain: $K_{i,d} = 86.3$

DC link controller gain: $K_{p,DC} = 60.6$

DC link controller integral gain: $K_{i,DC} = 2589$

Current controllers crossover frequency: $\omega_{c,i} = 1571 rad/s$

DC link controller crossover frequency: $\omega_{c,n} = 526.3 rad/s$

6.7.1 Machine side simulation results

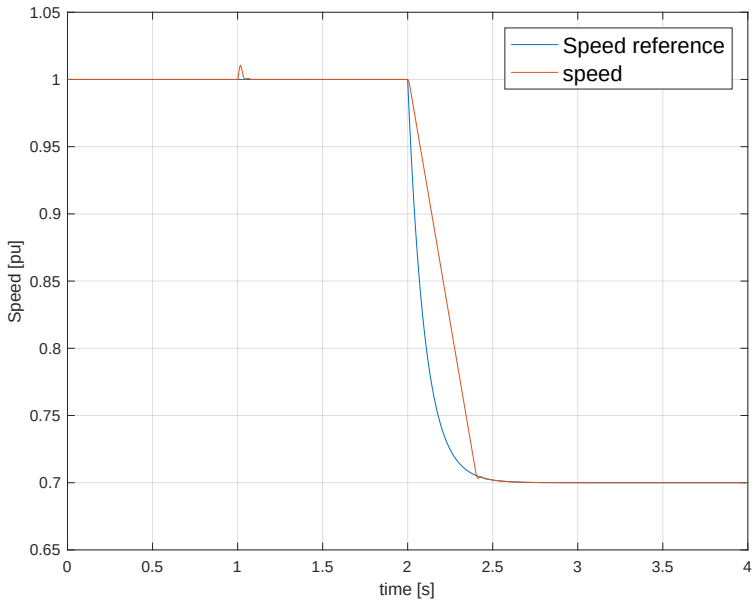

Figure 6.30: Speed and speed reference

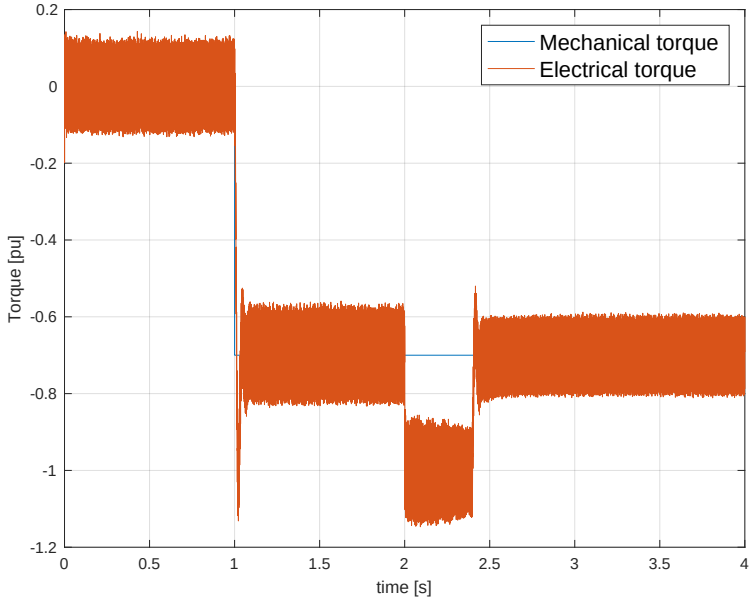

Figure 6.31: Electrical and mechanical torque

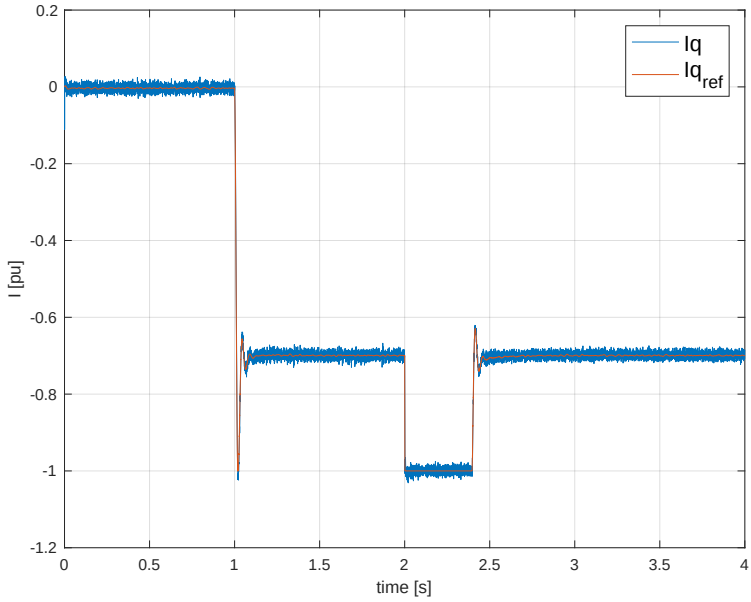

Figure 6.32: Machine side q-axis current i_q and its reference

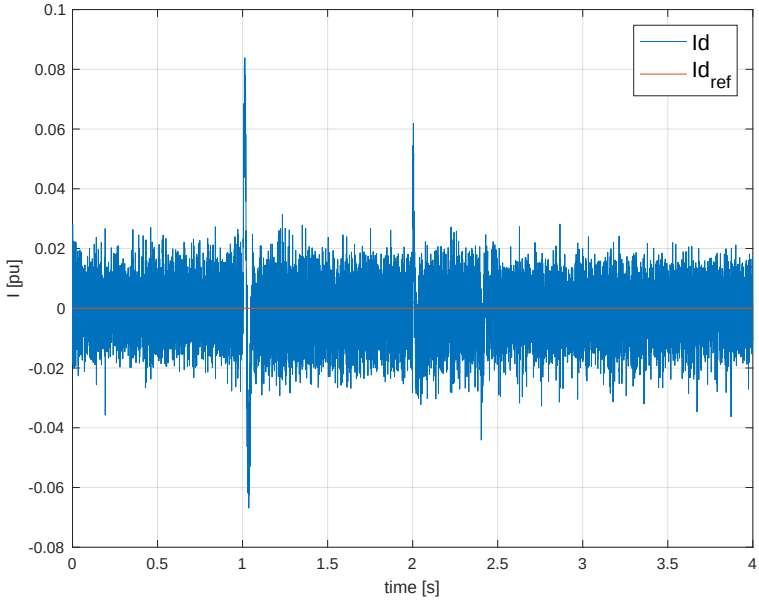

Figure 6.33: Machine side d-axis current i_d and its reference

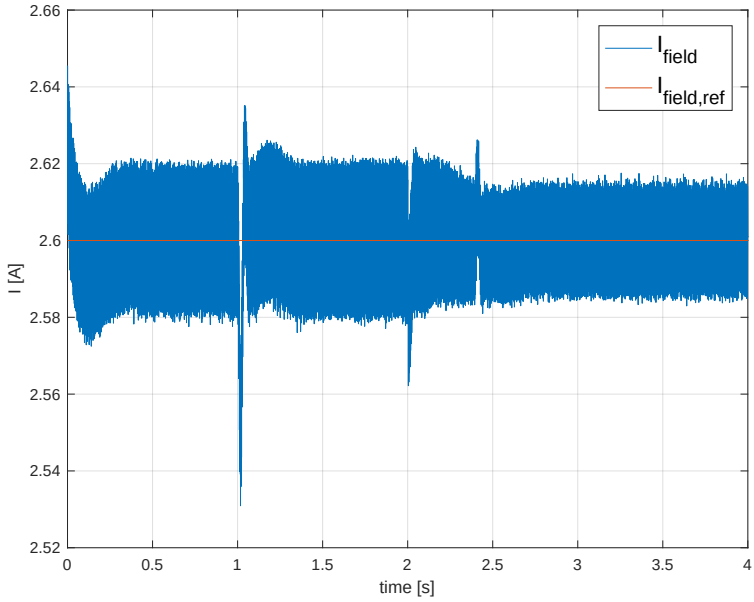

Figure 6.34: Field curren I_f and its reference

6.7.2 Grid side converter simulation results

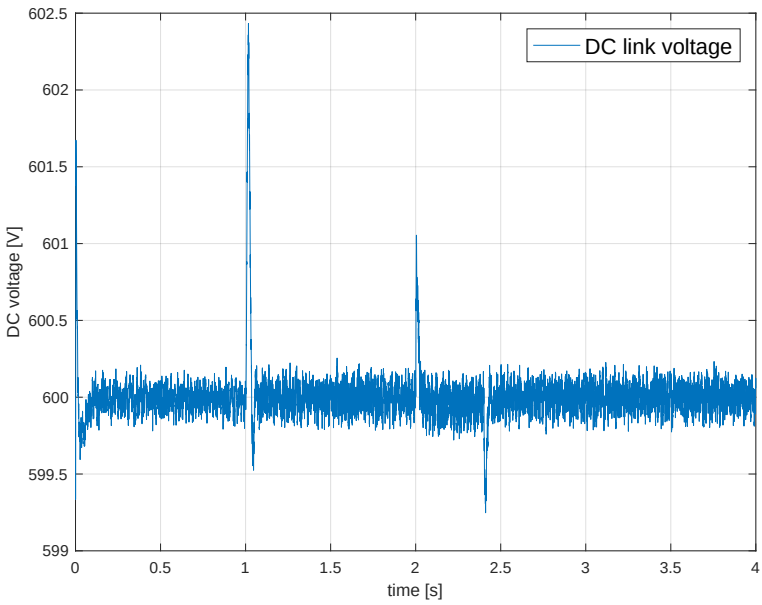

Figure 6.35: The DC link voltage is maintained at 600 V, it is however influenced by rapid changes in power from the machine side

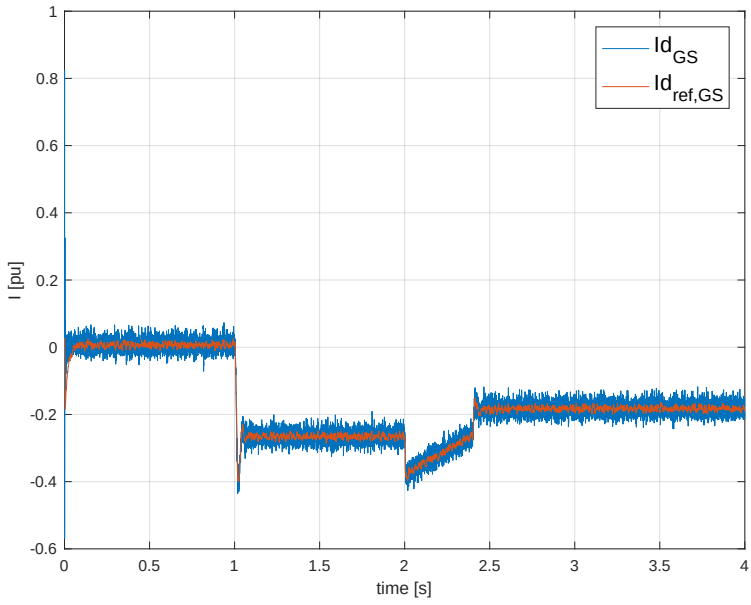

Figure 6.36: GSC d-axis current i_d and its reference

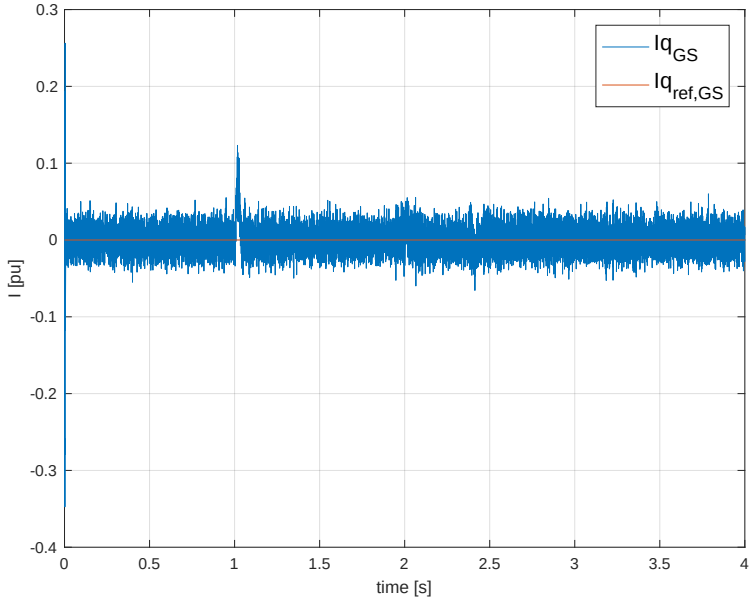

Figure 6.37: GSC q-axis current i_q and its reference

6.8 Evaluation of the simulation models

For all the simulations, the speed stabilises on the new speed reference without any significant overshoot. In the presented test scenario, the speed stabilises on the new speed within 0.5s. When examining the simulations presented in Appendix F, it can be seen that the models which included the LCL filter had slightly higher fluctuations in q-axis current, when the step in torque was applied, compared to the other converter models, and the simplified model. The electrical torque is sampled at a high frequency, so that it has large ripples in the same frequency as the switching. However, its mean values are equal to the q-axis current and its reference, which are filtered through the current measurement filter in the presented plots.

For the model which includes the back-to-back converter, the grid side converter manages to keep the DC link voltage within 2.5 V from the reference, also during the rapid changes in power from the machine side, which appears during the torque step. Overall, it seems like the simulation models where the machine is fed by a PWM voltage source converter performs as good as the model with the simplified voltage source.

When using the chosen control design, d-axis flux linkage will be $\Psi_d = 1$. The q-axis flux linkage will be proportional to the q-axis current, which is varied between 0 and 1 in magnitude. Using the per unit model from section 5.1, and neglecting the resistance, the d and q-axis steady state voltages can be calculated:

$$v_d = n * \Psi_q = n * x_q * i_q \tag{6.46}$$

$$v_q = n * \Psi_d = n \tag{6.47}$$

$$v = \sqrt{v_d^2 + v_q^2} = \sqrt{(n * x_q * i_q)^2 + n^2} \tag{6.48}$$

In the *abc* frame, the magnitude of the stator voltage will be as in (6.48) [16]. At maximum power at rated speed, v_q, i_q, p and n will all be 1pu. The stator voltage will be $v = \sqrt{0.42^2 + 1^2} = 1.084$, which means the stator voltage will be 8.4% above its rated value in that case. However, according to the open circuit test in section 3.8, the machine is rated for fields currents, which induces inner voltages that are at least 30% higher than the rated stator voltage of 220V. Therefore, it is assumed that the exceeding of the stator voltage of 8.4% during full torque and power is acceptable for the machine.

The control system is made for running the machine up to rated speed. For running the machine for higher than the rated, a control loop for field weakening should be implemented, to avoid exceeding the rated voltage excessively [31]. If it is wanted to avoid the exceeding of the rated voltage when operating at rated torque and power, it is also possible to control the d-axis current so that stator voltage and current is in phase, which means that $cos(\phi) = 1$ [16].

The 1 kHz harmonics caused by the LCL filter, showed in Figure 6.24 will also be present on the grid side. A possibility to reduce those oscillations is to implement control loops for active damping [32]. If the LCL filter is kept on the machine side, this would be useful on the machine

side as well.

It was observed that the models which included PWM switching had a much longer run time than simplified model. The model including the back-to-back converter, used approximately 15 minutes to simulate 4s, while this was done in 20-30s in the simplified model.

Chapter 7

Scenarios for variable speed hydro

In this chapter, scenarios that can be relevant for variable speed hydro are simulated. Simplified torque-speed characteristics are given, which determines the mechanical torque from a lookup table in the model.

The model with the simplified adjustable voltage source was used in this simulations. According to the simulations in the previous chapter, the back-to-back model and the simplified model performed similarly in the speed control of the machine. Thereby, the simplified model was chosen based on the advantage of a shorter simulation time. However, DC link dynamics is ignored in this model, meaning it will act like the grid side converter was ideal. The proposed and simulated test scenarios will also be possible to perform in the laboratory set-up. The filter time constants and the controller gains are the same as used in section 6.2.

7.1 Synthetic inertia of hydro generator

In this simulation, the torque is set to be dependent on speed, so that the torque is given by a look-up table, equal to the curve seen in Figure 7.1. This curve will be equal to a Pelton turbine operating with constant gate opening. It is chosen to simulate a Pelton turbine, because of the turbine speed, and the water flow is decoupled so that waterways can be ignored. For a Francis

turbine, the water flow will be dependent on the speed, which makes it more complicated to simulate the torque [33].

The torque is set to be 70% of the machine base torque at rated speed. There is no governor implemented, since the effect of the inertia is wanted to be seen. A drop in grid frequency of 0.2 Hz is shown in Figure 7.2, goes into the derivative controller, which gives an additional signal to the i_q reference current. The power system is not included in the simulation, and the frequency drop is only a signal, made to investigate the behaviour of the control system and the synchronous machine. The objective of the scenario is to inject a disturbance to the q-axis current, which will increase the torque during the frequency drop, to increase the delivered power for a short period. In this way, the converter-fed generator can contribute to damp frequency drops in a power system, by boosting the power for a short time, before the governor makes a lasting change in power production.

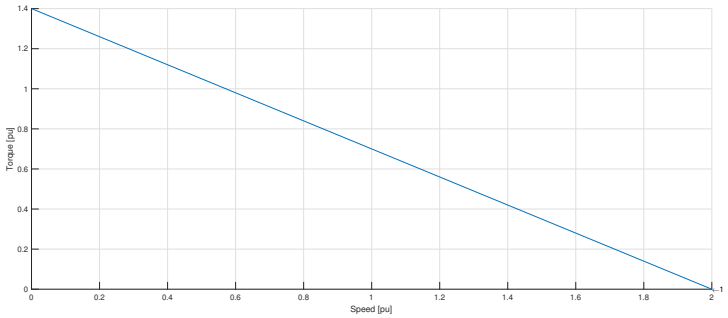

Figure 7.1: Torque speed characteristics of a pelton turbine with constant gate opening

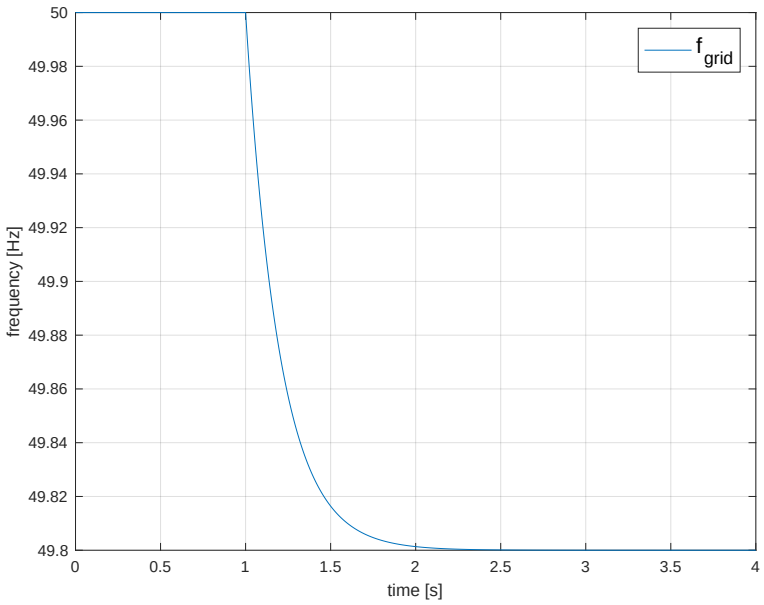

Figure 7.2: Simulated frequency signal which goes in to the derivative controller

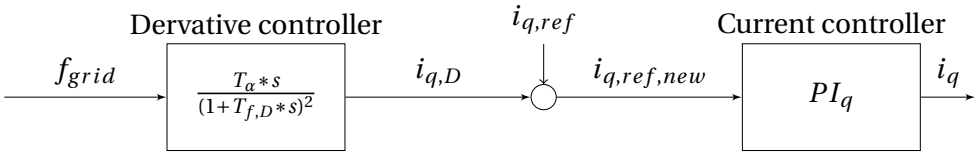

Figure 7.3: Derivative control loop for short synthetic inertia

The frequency drop signal was modelled as a step from 50 to 49.8, filtered with a filter time constant of 0.2s, and is showed in Figure 7.2. It was applied to the control loop, showed in Figure 7.3. The chosen controller is a derivative controller. It will only act on changes in grid frequency, and will not have a steady-state impact after a change in frequency. In the simulation presented, the controller values are set to $T_{f,D} = 0.1s$ and $T_\alpha = 30 * T_f$. From Figure 7.4, it is seen that the disturbance injected from the derivative controller is quickly accounted for by the speed controller. However, the new reference going to the current controller, and the q-axis current, is increased slightly, according to Figure 7.5. The impact on the power and speed is shown in Figure 7.6, where the initial power production is set to 1. The deacceleration time only last 0.1s, and the power is at maximum boosted with 8% compared to the initial production. The impact on the speed is well below 1%.

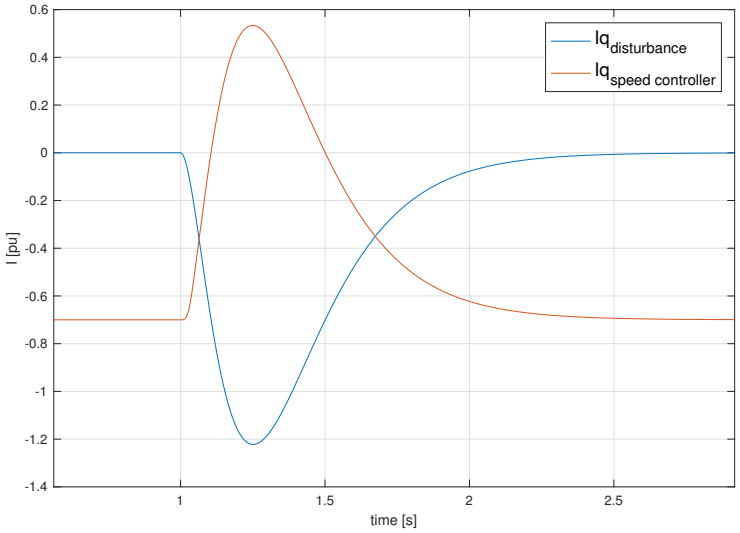

Figure 7.4: Disturbance signal and signal from speed controller for i_q current

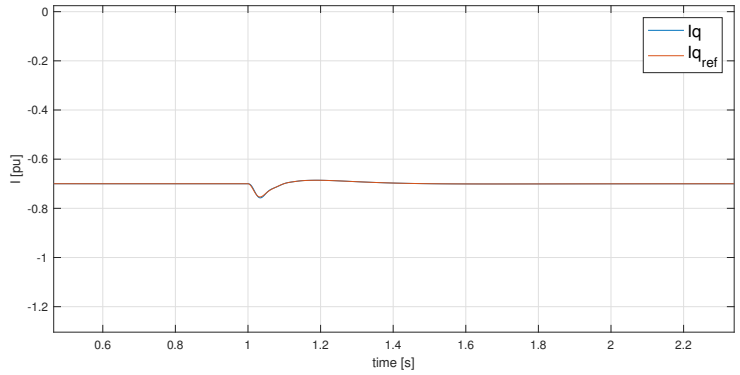

Figure 7.5: q-axis current and its reference

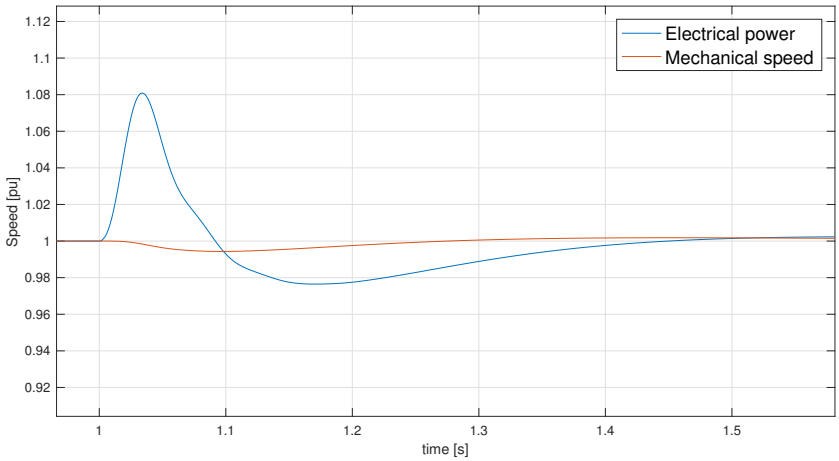

Figure 7.6: Active power boosts with up to 8 percent under deceleration of the rotor

From the simulations, it is clear that the speed controller is quite fast, so that the disturbance from the derivative controller is cancelled quite fast. If a longer and more aggressive response is desired, the gain of the derivative controller can be further increased. The speed controller can also be made slower, so that it would use longer time to repress the injected disturbance.

Influencing the speed reference

Another solution attempted was to inject the disturbance by the speed reference to achieve a lengthier power injection. Then, the response from the derivative controller was added to the speed reference, and thereby not opposed by the outer control loop. Figure 7.7 shows a much stronger and longer-lasting response than in Figure 7.6, with $T_{f,D} = 0.5s$ and $T_\alpha = 0.35 * T_f$ at the derivative controller. In this case, the power boost is at 18% at its maximum, and lasts 0.7s before the generator speed is starting to recover. In this case, the duration and magnitude of the power boost, can easily be adjusted by controlling the deacceleration through the derivative controller. The model structure of the control loop is shown in section E.2

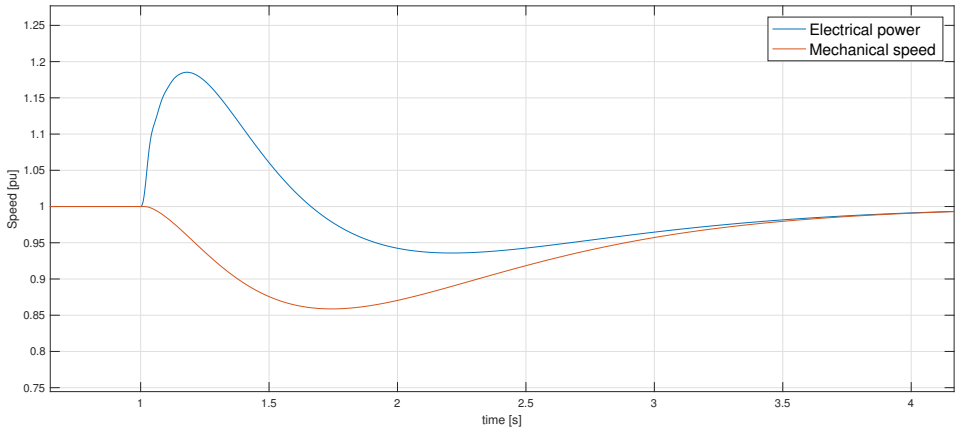

Figure 7.7: Active power boosts when influencing the speed reference

7.2 Simulation of pumped hydro plant as a variable load

As new renewables are emerging, an important task of pumped hydro plants is to store available surplus power during high production from fluctuating sources. The mechanical load torque is given from the curve in Figure 7.8. A torque characteristic equal to n^2 is assumed in the relevant pumping area. The nominal pumping torque is set to 0.8 of the machine capability. Transients in the hydraulic waterways are ignored, assuming a well-damped hydraulic system. It is also assumed that the acceleration time of the water ways is below the limitations of speed changes, set in the simulations.

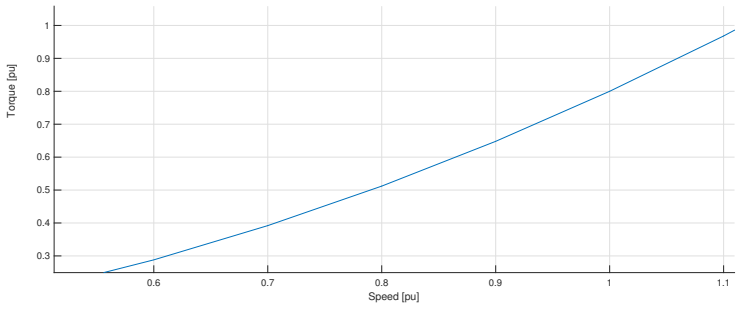

Figure 7.8: n^2 torque speed characteristics for a pump

7.2.1 Changes in speed with 0.35 pu/s

The limit of the change in the reference was set to 0.35/s, meaning the speed reference at least uses 2.86s to go from zero to 1. The reference is also filtered, with a filter time constant of 0.2s. This gives a smooth change in speed and power, as shown in Figure 7.9 and Figure 7.10. In this system, large changes in power can be done in a short. According to Figure 7.9, changes of 2-3kW in power can be done within 0.2-0.3s.

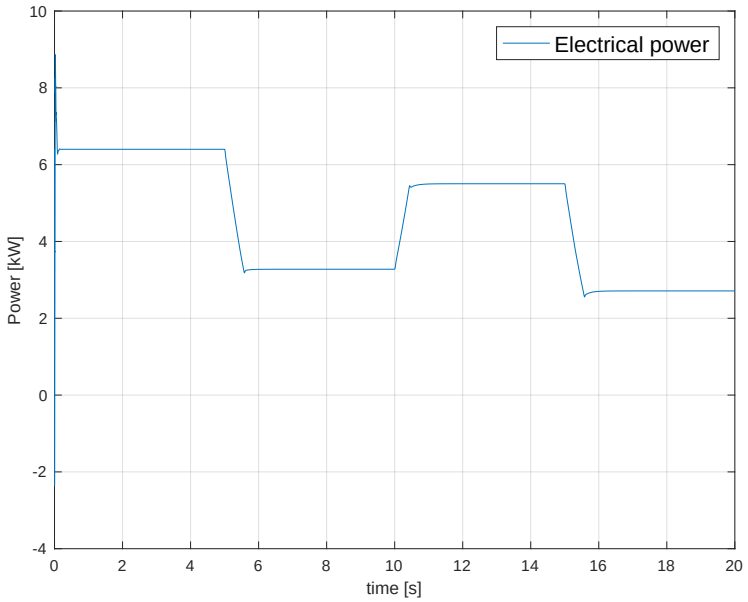

Figure 7.9: Pumping power can be changed with the speed

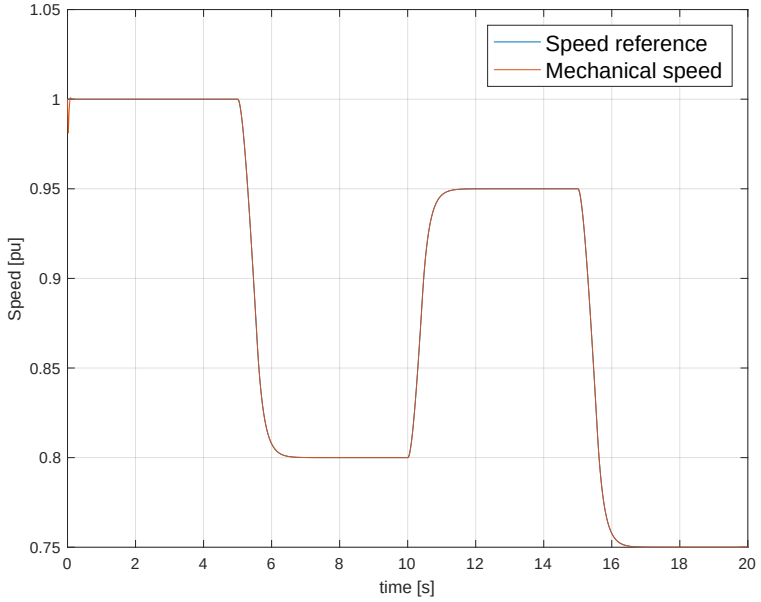

Figure 7.10: The speed following the ramped and filtered speed reference

7.2.2 Changes in speed with 1 pu/s

A more aggressive approach is also simulated, with a change of rate limit of 1/s, meaning the speed reference can go from 0 to nominal speed in 1s. Assuming a hydraulic waterway which is short, so that the acceleration time of the water is equal to, or below 1s. The reference is also filtered with a filter time constant of 0.1s. Using this rate, the changes in power can be done within 0.1s. However, some overshoot has to be accepted, according to Figure 7.11. The speed is changed without any overshoot, as seen in Figure 7.12.

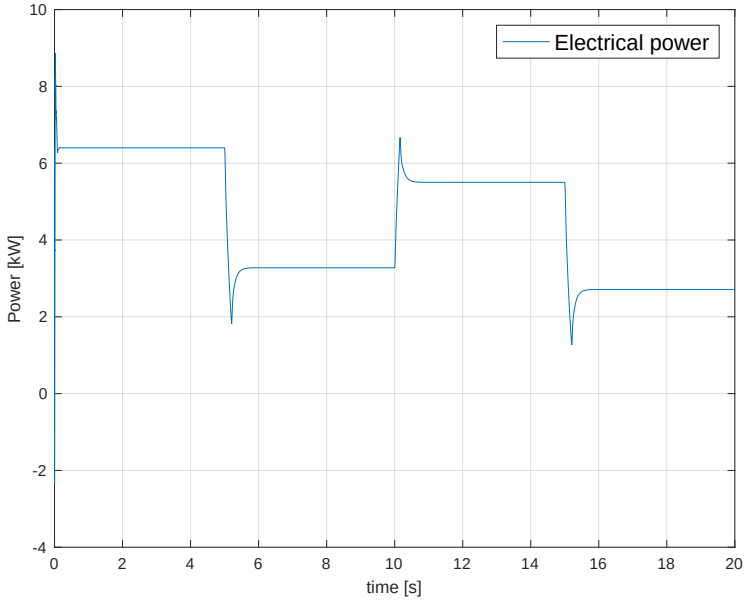

Figure 7.11: Pumping power can be changed with the speed

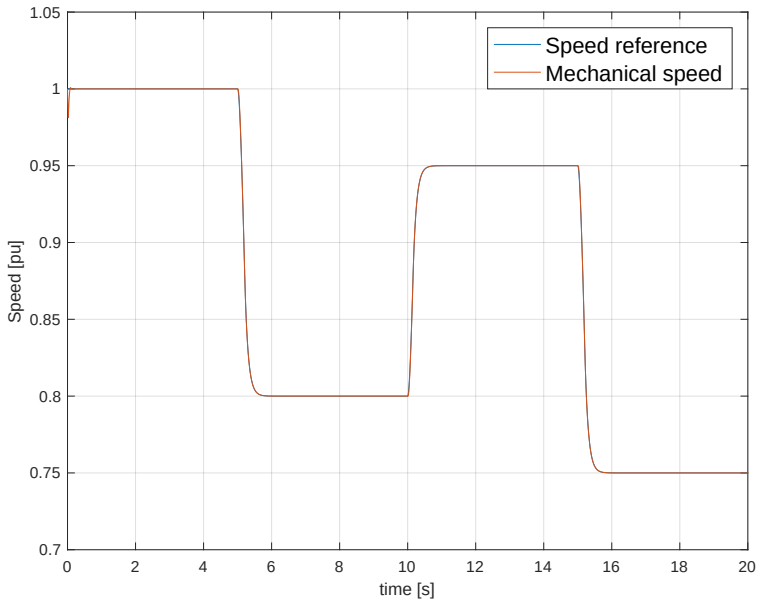

Figure 7.12: The speed following the ramped and filtered speed reference

It will also be possible to apply the control strategy for synthetic inertia for the pumped power plant, similar to what is done in the previous section. Since the power during pumping is

determined by the speed, it is also possible to apply a droop in the speed control, for steady-state contribution to grid frequency stability [1].

Chapter 8

Discussion

8.0.1 Synchronous machine parameters

Considering the amount of matching data from the lab tests, the steady state and transient parameter values can be considered to be quite accurate. However, there is an uncertainty regarding the subtransient values. There is also a fair amount of uncertainty regarding the armature time constant found in the lab, as it was required to know the d-axis reactances and time constant, to determine the value from the lab test. The accuracy of the armature time constant is thereby dependent on the accuracy of the d-axis parameters.

As discussed in section 4.6, some formulas showing the relations between different parameter values does not match very well. If the armature time constant found in lab is the correct value, it is very likely that the subtransient parameter values are higher than the found values. If the assumed ratio between subtransient d- and q- axis reactance is correct, both of them should be proportionally bigger. However, the estimated ratio might be wrong or the armature time constant found in lab may be too big. As also previously discussed, a calculated value from the d-axis reactances and the transient time constant is calculated to be 30 % higher than the measured value. This implies that there are inaccuracies in the parameter values. Modification of one or several parameter values could be done to make the calculations more correct. Estimating

a higher value of the stator leakage reactance would lead to a lower calculated field resistance, as previously discussed in section 4.6. However, the ratio to the d-axis subtransient value is already high, meaning that this scenario is very unlikely unless the subtransient reactance is adjusted upwards. Another scenario could be that the d-axis transient parameter values found in lab should be adjusted. The reactance could be adjusted downwards, or the time constant upwards, or a combination of these two. It should also be noted that the formula used for calculating the field resistance is an approximated relation, as it contains a simplification as discussed in section 4.3. The mechanical time constant is also quite roughly calculated, and could be tried to be more precisely determined in further work.

8.0.2 Simulations and control system

The control system for the motor can be improved considering control of d-axis current and field current. In the presented control system, the armature voltage is allowed to exceed the rated value up to 8.4% at rated speed, which is considered to be acceptable for the machine. The converter and the converter voltage level is over dimensioned compared to the machine, which means it has no problem delivering the required machine side voltage. However, implementation of control loops for field weakening could be implemented as an improvement, to be able to run the machine above rated speed, without exceeding the voltage machine rated voltage excessively.

The way the converter is connected to the grid, is not realistic, considering the difference in voltage level between the grid and the machine. A more realistic set-up would be to connect it to 230V AC on the grid side, for example through a transformer. The DC link voltage could be decreased accordingly. This would also set higher requirements to the machine side control system, as the AC voltage would be limited by the DC link voltage. SVPWM could be implemented to get higher AC voltage from the DC link.

For the simulations of hydro-power scenarios, an important aspect is the inertia of the machine. The lab machine has a low inertia, and a low inertia constant of $H = \frac{T_m}{2} = 0.2$s. A hydropower generator normally has an inertia time constant which is 10 to 20 times higher [3]. The higher

inertia constant of real hydro generators can be made to make a higher and longer lasting impact using synthetic inertia, than in the presented simulations using the lab machine properties.

Chapter 9

Conclusion and Recommendations for Further Work

9.1 Conclusion

Variable speed of hydropower generators has a potential for increasing the flexibility of hydropower plants, which will be important in future power systems, as the contribution from fluctuating sources such as wind and solar is increasing. This thesis strives to contribute to the development, by studying the implementation of a converter fed synchronous machine in lab. The work progress can be summarised by the following steps:

1. Testing and documentation of the 8 kVA synchronous machine in lab, including short circuit tests, a slip test, and an open circuit saturation test.
2. Estimations and calculations of parameter values which were not covered by the tests.
3. Development of a simulation model using Simulink, with a cascaded control system for variable speed of the synchronous machine. In the first step, it was done with a simplified voltage source, which can be varied with regard to voltage and frequency.

4. Modelling of the back-to-back converter and development of a control system for the grid side converter.

5. Identification and simulations of operating scenarios that are relevant for variable speed hydropower.

From the parameter determination test results, the steady state and transient values are determined with relatively high precision. The d-axis subtransient values were also found, however with higher uncertainty regarding the accuracy. Also, the armature time constant was found from the test results. The resistances in the field and armature winding were measured directly.

The stator leakage reactance was estimated to be 10% of the steady state value in the d-axis, while the q-axis subtransient parameters were estimated based on typical relationships to the subtransient d-axis values. From the stator impedances and time constants, the leakage reactances and resistances in the rotor were calculated.

Values for the armature time constant and the field winding resistance were calculated from the found stator parameters. This was interesting because they were already determined via lab experiments. The calculation of the armature time constant indicates that one or both of the subtransient reactances are too low, or that a too high value was found from the short circuit tests. The calculation of the field winding resistance indicates that there is inaccuracy in the determination of the transient parameter values, or in the estimation of the stator leakage reactance.

For the machine side system, a cascaded control system was used. An outer speed control loop maintains the speed at its reference by giving a torque reference to the inner control loop, which controls the q-axis current according to the reference. For the grid side converter, the outer loop is set to monitor and control the DC link voltage to 600V. This is done by controlling the active power reference to an inner control system, which controls the d-axis current accordingly. In this way, the active power exchange with the grid is controlled to be equal to the DC link power exchange with the machine side.

Both the model with a simplified voltage source and the models including converters, provided

satisfying results in controlling the speed. Meaning the speed stabilised within 0.5s in the presented simulation, and inner q-axis controller is following the reference from the outer loop.

In the simulation model, the DC link voltage is chosen to be 600 V, while the the grid side converter is coupled to a 400 V AC source. This is done to mimic the present lab set-up. However, it will be possible to redesign the lab set-up, so that the grid side is coupled to a voltage level which is closer to the ratings of the machine, which is more realistic compared to a real implementation in a hydropower plant.

For hydropower application, a control method is proposed and simulated for the synchronous machine, for a contribution of synthetic inertia during a frequency drop in the grid. This is done by implementing a derivative controller that has the grid frequency as the input. This is used to inject a disturbance to the torque or the speed reference during a frequency drop, so that the machine brakes and delivers additional power.

For simulations of synthetic inertia, the mechanical torque was given the torque characteristics of a typical hydro turbine, while a signal representing the grid frequency dropped by 0.2Hz during 2s.

In the presented simulation where the speed reference is influenced by the derivative controller, the power reaches 18% increase, while the total boost duration is 0.7s. By influencing the torque, a fast, but shorter response was achieved. In the presented simulation, the power increases with 8% at its peak, while the boost duration is 0.1s. An issue of these simulations is that the lab machine has a low inertia constant of 0.2s. For typical hydropower generators, with a ten to twenty times higher inertia constant, the response could have been more significant and long-lasting. It is probable that controlling converter fed hydrogenerators for synthetic inertia can boost the power production during frequency drops, and thereby contribute to stabilise the grid. Adjustable power pumping was also simulated, by giving the torque the characteristics of pump. The power was then adjusted in steps of 2-3kW within 0.1-0.3s.

The simplified model with a variable AC source was used for simulating hydropower operation scenarios, as it performed very similar to the models that included converters and PWM switching,

and had a much lower run time. However, it does not account for the DC link dynamics. For further simulations, it is recommended to develop the simplified model with a so called averaged model. This will keep the benefits of a low run time, while the DC link dynamics can be included, so that the simplified model is more representative for a converter.

In the case of lowering the DC link voltage and connecting the grid side converter to 230 V AC, the maximum AC voltage which can be delivered to the machine will be limited by the DC link voltage. The control system should then be further developed to inject d-axis current, so that $cos(\phi) = 1$. This will lead to 8% lower voltage at rated power, compared to injecting only q-axis current, as done in the present control system. A control loop for field weakening should be implemented, to be able to run above rated speed. It is also recommended to apply SVPWM on the machine side converter, to better utilise the DC link voltage when inverting to AC, compared to sinusoidal PWM switching.

9.2 Recommendations for Further Work

- For further investigation of the effect of synthetic inertia contribution on power system stability, a power system should be included in the simulations.
- Implementation and simulation of droop characteristics in pump mode.
- Implementation of synchronous sampling in the lab set-up.
- Implement a controlled excitation source in the lab, with feedback measurements from the field current.
- Perform experiments of the proposed operating scenarios in the lab set-up.
- Apply active damping in the control system, to damp the oscillations from the LCL filter.
- Control the 15 kW asynchronous machine in lab to mimic a Francis turbine.
- Further testing for more precise determination of synchronous machine parameters.

Bibliography

[1] H. Schlunegger and A. Thöni, "100 mw full-size converter in the grimsel 2 pumped-storage plant," in *Proc. 2013 HYDRO Conference*, 2013.

[2] N. Hamsic, A. Schmelter, A. Mohd, E. Ortjohann, E. Schultze, A. Tuckey, and J. Zimmermann, "Increasing renewable energy penetration in isolated grids using a flywheel energy storage system," in *2007 International Conference on Power Engineering, Energy and Electrical Drives*, IEEE, 2007, pp. 195–200.

[3] A. Lechner, "Pumped storage contribution to grid inertia, andritz hydro,"

[4] NVKS, `http://www.ntnu.no/nvks/ex_english`, Accessed: 2017-06-06.

[5] B. Iversen, *Doubly-fed induction machine for use in mini-hydro power plants*, 2016.

[6] K. Ljøkelsøy, *Control system for a three-phase grid connected converter. 3 september 2014 version. description*. SINTEF Energi, 2014.

[7] J. Machowski, J. Bialek, and J. Bumby, *Power system dynamics: Stability and control*. John Wiley & Sons, 2011.

[8] *Ieee guide: Test procedures for synchronous machines - std 115-1983*, IEEE, 1983.

[9] S. Chapman, *Electric machinery fundamentals*. McGraw-Hill, 2012.

[10] P. C. Sen, *Principles of electric machines and power electronics, third edition*. John Wiley & Sons, 2014, pp. 297–299.

[11] P. Kundur, N. J. Balu, and M. G. Lauby, *Power system stability and control*. McGraw-hill New York, 1994, vol. 7.

[12] K. Bonfert, *Betriebsverhalten der Synchronmaschine*. Springer, 1962.

[13] R. Nilsen, *Synkron motordrifter*. NTNU, 2016.

[14] *Calculation of moment of inertia of a hollow/solid cylinder*, `https://www.miniphysics.com/uy1-calculation-of-moment-of-inertia-of-cylinder.html`, Accessed: 2017-06-06.

[15] JFE, *Electrical steel sheets*, `http://www.jfe-steel.co.jp/en/products/electrical/catalog/f1e-001.pdf`, Accessed: 2017-04-21, 2017.

[16] R. Nilsen, *Kompendium TET4120, Electric Drives*. NTNU, 2016.

[17] S.-K. Sul, *Control of electric machine drive systems*. John Wiley & Sons, 2011, vol. 88.

[18] N. Mohan, *Advanced electric drives: Analysis, control, and modeling using MATLAB/Simulink*. John wiley & sons, 2014.

[19] J. W. Umland and M. Safiuddin, "Magnitude and symmetric optimum criterion for the design of linear control systems: What is it and how does it compare with the others?" *IEEE Transactions on Industry Applications*, vol. 26, no. 3, pp. 489–497, 1990.

[20] J. A. Suul, M. Molinas, L. Norum, and T. Undeland, "Tuning of control loops for grid connected voltage source converters," in *Power and Energy Conference, 2008. PECon 2008. IEEE 2nd International*, IEEE, 2008, pp. 797–802.

[21] R. Nilsen, Private communication, Department of Electrical Engineering, NTNU, 2017-04-25.

[22] G. Oddmund, *Identifikasjon og regulering av en synkronmotordrift*, 2004.

[23] T. F. Nestli, *Modulus and symmetric optimum criteria for the design of linear control systems*, memo, TET4120, 2010-03-15.

[24] A. Yazdani and R. Iravani, *Voltage-sourced converters in power systems: Modeling, control, and applications*. John Wiley & Sons, 2010.

[25] C. Bajracharya, M. Molinas, J. A. Suul, T. M. Undeland, *et al.*, "Understanding of tuning techniques of converter controllers for vsc-hvdc," in *Nordic Workshop on Power and Industrial Electronics (NORPIE/2008), June 9-11, 2008, Espoo, Finland*, Helsinki University of Technology, 2008.

[26] T. Kalitjuka, *Control of voltage source converters for power system applications*, 2011.

[27] K. Ljøkelsøy, *20 kva back to back converter set. documentation*, SINTEF Energi, 2011.

[28] R. Nilsen, Private communication, Department of Electrical Engineering, NTNU, 2017-05-05.

[29] K. Ljøkelsøy, private communication, e-mail, SINTEF Energi, 2017-05-05.

[30] ——, *20 kw igbt omformer. beskrivelse*, SINTEF Energi, 2003.

[31] S. Umans, A. Fitzgerald, and C. Kingsley, *Electric Machinery*. McGraw-Hill Higher Education, 2013.

[32] O. Mo, M. Hernes, and K. Ljøkelsøy, "Active damping of oscillations in lc-filter for line connected, current controlled, pwm voltage source converters," in *Proc. 10th European Conf. Power Electron. Applicat*, 2003.

[33] B. Svingen, private communication, Department of Energy and Process Engineering, NTNU, 2017-05-08.

Appendix A

Per Unit Quantities Calculations

A.1 Per unit quantities of the machine

The per unit quantities for the stator of the synchronous machine, is based on the rated values of the machine. Even though the machine will be run as both motor and generator, the rated values in generator mode are chosen on the basis of the per unit quantities.

The basis of the voltage and current is chosen to be the peak of their sinusoidal function. This is practical in the control system, since they are sampled, measured and transformed to the dq frame in their instantaneous values.

The per unit value of the inductance l, is defined as $l = \frac{L}{L_base}$. This means the inductances will have the same per unit value as its corresponding reactance.

$V_{s,base}$ = peak value of rated line to neutral voltage [V]
$I_{s,base}$ = peak value of rated line current [A]
$f_{s,base}$ = rated frequency [Hz]

Based on the rated values in Table 3.1, the base quantities can be calculated, based on the voltage and rated power below:

$$S_{s,n} = S_{s,base} = 8kVA \tag{A.1}$$

$$V_{s,n} = 220V \tag{A.2}$$

$$f_n = 50Hz \tag{A.3}$$

$$V_{s,base} = \frac{\sqrt{2} * V_{s,n}}{\sqrt{3}} = \frac{\sqrt{2} * 220V}{\sqrt{3}} = 179.62V \tag{A.4}$$

$$I_{s,base} = \frac{\sqrt{2} * S_{s,base}}{\sqrt{3} * V_{s,n}} = \frac{\sqrt{2} * 8000VA}{\sqrt{3} * 220V} = 29.69A \tag{A.5}$$

$$Z_{s,base} = \frac{S_{s,base}}{\sqrt{3} * V_{s,n}} = \frac{V_{s,base}}{I_{s,base}} = 6.05\Omega \tag{A.6}$$

$$\omega_{el,base}\omega_n = 2 * \pi * f_n = 100 * \pi rad/s \tag{A.7}$$

$$\omega_{m,base} = \frac{\omega_{el,base}}{pp} = \frac{100 * \pi}{3} = 104.72rad/s \tag{A.8}$$

$$L_{s,base} = \frac{Z_{s,base}}{\omega_n} = 0.01925H \tag{A.9}$$

$$\tau_{base} = \frac{S_{s,base}}{\omega_{m,base}} = \frac{8000VA}{104.72rad/s} = 76.39Nm \tag{A.10}$$

Since the machine is rated for higher current in motor mode, it would lead to a lower base impedance, if the motor rating was used for calculating the base values. In that case, the base impedance would be $Z_{b,motor} = \frac{220V}{\sqrt{3}*26.1A} = 4.87\Omega$, while the base apparent power would be $S_{b,motor} = \sqrt{3} * 26.1A * 220\text{V} = 9945VA$.

A.2 Per unit quantities of the grid side converter

For the grid side converter, the grid voltage and the power rating of the converter are used to determine per unit quantities.

$$S_{c,n} = S_{c,base} 20kVA \tag{A.11}$$

$$V_{c,n} = 400V \tag{A.12}$$

$$f_n = 50Hz \tag{A.13}$$

$$V_{c,base} = \frac{\sqrt{2} * V_{c,n}}{\sqrt{3}} = \frac{\sqrt{2} * 400V}{\sqrt{3}} = 326.6V \tag{A.14}$$

$$I_{c,base} = \frac{\sqrt{2} * S_{c,base}}{\sqrt{3} * V_{c,n}} = \frac{\sqrt{2} * 20000VA}{\sqrt{3} * 400V} = 40.82A \tag{A.15}$$

$$Z_{c,base} = \frac{V_{s,base}}{I_{s,base}} = \frac{326.6V}{40.82A} = 8.0\Omega \tag{A.16}$$

$$L_{c,base} = \frac{Z_{c,base}}{\omega_n} = \frac{8.0\Omega}{100 * \pi} = 0.0255H \tag{A.17}$$

$$\tag{A.18}$$

A.2.1 DC link per unit quantities

The DC link per unit current and impedance can be calculated when choosing the DC base to be 600 V.

$$V_{DC,base} = 400V \tag{A.19}$$

$$I_{DC,base} = \frac{S_{c,base}}{V_{DC,base}} = \frac{20000VA}{600V} = 33.33A \tag{A.20}$$

$$Z_{DC,base} = \frac{V_{DC,base}}{I_{DC,base}} = \frac{600V}{33.33A} = 18\Omega \tag{A.21}$$

Appendix B

Offer for Upgrading the Speedgoat Software

The following two pages are showing av offer for upgrading the existing software on Speedgoat equipment used in the lab, to make it compatible with the newest versions of Matlab. The offer was received by Vladimir Klubicka 25/1-2017, at the Service Lab at the Department of Electrical Engineering.

Speedgoat GmbH
Waldeggstrasse 37
3097 Liebefeld
Switzerland

Phone +41 26 670 75 50
Fax +41 26 670 75 58
www.speedgoat.ch

NTNU/Elkraftteknikk
O.S. Bragstadsplass 2E
3 etg. E-blokk
NO 7491 Trondheim
NO

Reference No. Ref_17012521

Date	25-January-2017
Currency code	EUR
Your reference	Vladimir Klubicka
Our reference	Joscha Kunz
Renewal Period	01-February-2018

Systems Software Maintenance and Support Renewal - 1 Year

The Systems Software Maintenance and Support Service provides access to latest Speedgoat drivers and tools compatible with future MathWorks software releases and therefore instant access to latest MathWorks and Speedgoat software features with your real-time target machine, and professional technical support by phone and e-mail.

The offer renews subscription of all your systems listed below to the renewal date 01-February-2018, and guarantees continued access to maintenance and support services. Annual pricing is 5% of the product list price.

Modular-HD160GB - SN1415					**Vladimir Klubicka**
Renewal					
Item Description	**Item-ID**	**# of Months**	**Renewal Period**	**Monthly Cost**	**Ext. Price**
Modular-HD160GB	103020	12	01/Feb/2017 - 01/Feb/2018	1.30	15.60
IO106	20106	12	01/Feb/2017 - 01/Feb/2018	18.60	223.20
IO110	20110	12	01/Feb/2017 - 01/Feb/2018	19.10	229.20
IO203	20203	12	01/Feb/2017 - 01/Feb/2018	9.50	114.00
IO311	20311	12	01/Feb/2017 - 01/Feb/2018	17.40	208.80
IO311-PMW18TTL-R2010b	20311A	12	01/Feb/2017 - 01/Feb/2018	0.00	0.00
IO703	20703	12	01/Feb/2017 - 01/Feb/2018	2.00	24.00
System total:					**814.80**

Modular-Large real-time target machine - SN1416					**Vladimir Klubicka**
Renewal					
Item Description	**Item-ID**	**# of Months**	**Renewal Period**	**Monthly Cost**	**Ext. Price**
Modular-Large real-time target machine	103004 103004 103020	12	01/Feb/2017 - 01/Feb/2018	76.10	913.20
IO106	20106	12	01/Feb/2017 - 01/Feb/2018	18.60	223.20
IO110	20110	12	01/Feb/2017 - 01/Feb/2018	19.10	229.20
IO203	20203	12	01/Feb/2017 - 01/Feb/2018	9.50	114.00

Modular-Large real-time target machine - SN1416					Vladimir Klubicka
Renewal					
Item Description	**Item-ID**	**# of Months**	**Renewal Period**	**Monthly Cost**	**Ext. Price**
IO311	20311	12	01/Feb/2017 - 01/Feb/2018	17.40	208.80
IO703	20703	12	01/Feb/2017 - 01/Feb/2018	2.00	24.00
System total:					**1,712.40**

Subtotal net	**2,527.20**
Volume discount for 2 machines: 3% (2,527.20)	**75.80**
Total net	**2,451.40**

Renewing subscription to the Speedgoat Systems Software Maintenance and Support, and the MathWorks Software Maintenance Service in subsequent years guarantees continued access to latest product technologies. Reinstatement of the Maintenance Service fee is possible, but incurs back maintenance charges plus a reinstatement. Staying subscribed is the most cost-effective way to get the latest advances and all the support you want.

Total net **EUR 2,451.40**

Appendix C

Instrument list

Table C.1: List of measurement equipment used for parameter determination tests

Number	Equipment	Model type	NTNU ID
1	Oscilloscope	TEKTRONIX MSO 2014	G04-0344
2	Multimeter	Fluke 177	S03-0416
3	Multimeter	Fluke 177	S03-0423
4	Differential probe	TEKTRONIX P5200A	I06-0516
5	Current meter tong AC/DC	FLUKE 80i-110s	I04-0489
6	Current meter tong AC	FLUKE i1000s	I04-0494
7	Milliohm meter	Instek GOM - 802	H01-0096

Table C.2: Application of measurement equipment for parameter determination tests

Number	NTNU ID	Application
1	G04-0344	Logging of voltages and currents
2	S03-0416	Terminal voltage and field circuit resistance
3	S03-0423	Field circuit voltage and resistance
4	I06-0516	Phase to neutral voltage
5	I04-0489	Field current
6	I04-0494	Stator current
7	H01-0096	Armature resistance

Appendix D

Additional results from short circuit test

D.1 Test #64 and #90 from short circuit test

To investigate the credibility of the found results.The results from chapter 3 are plotted together with test #64 and #90, to investigate the validity of the results.

In Figure D.1 and Figure D.2, the transient part of the current of test #64 and #90, are plotted, the same way as in subsection 3.5.1. They are plotted together with a line corresponding to the found transient part of the current and the transient time constant, $\ln(90) + t/0.069$. For #90, the line fits very well to the test results. The line also fits sufficiently well for test #64, but could have been set a bit lower. However, the slightly bigger DC component of test #64 makes it less reliable for analysis.

For both tests, the small DC components make the analysis of the subtransient component unreliable. Plotted the same way as in subsection 3.5.2, they are shown in Figure D.1 and Figure D.2. Test #64 giving a very low subtransient current and long time constant, while opposite for #90. However, using the first and third half cycle of #90, a similar subtransient current can be found, but a longer time constant, when comparing to the result from #75 and #102 in chapter 3.

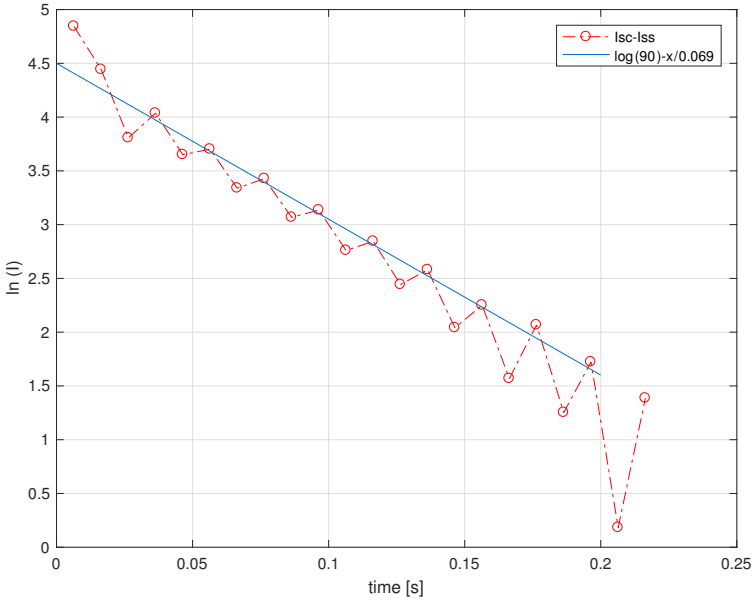

Figure D.1: Semi-logarithmic plot of the subtransient part of the short circuit current of test #64.

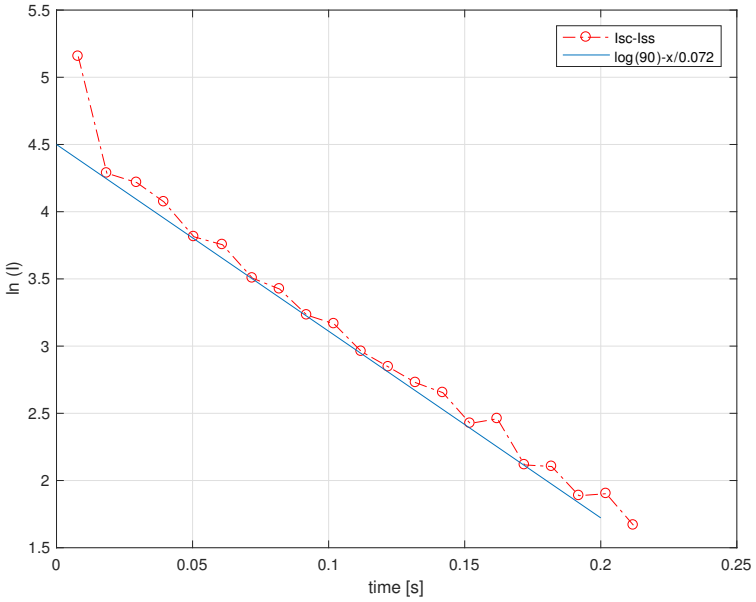

Figure D.2: Semi-logarithmic plot of the transient part of the short circuit current of test #90

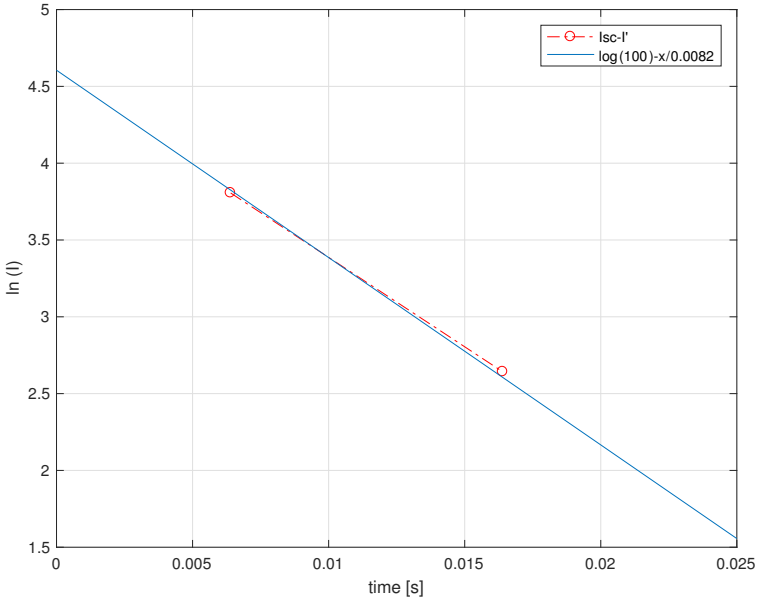

Figure D.3: Semi-logarithmic plot of the transient part of the two firs half cycles of test #64.

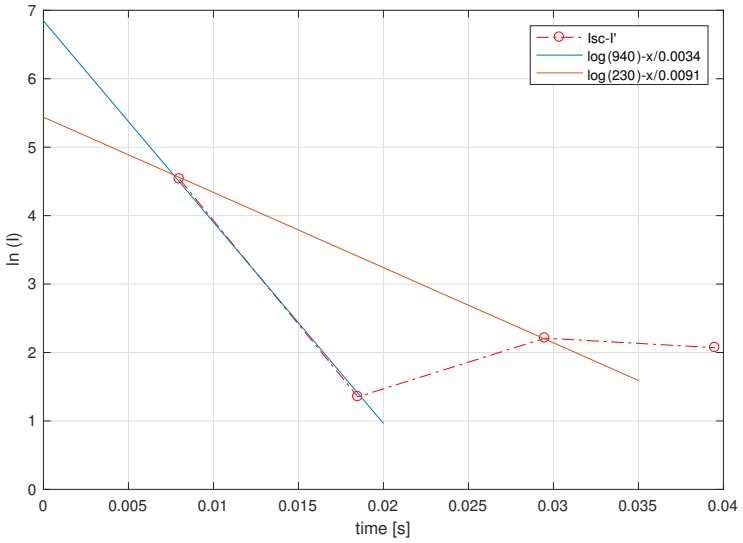

Figure D.4: Semi-logarithmic plot of the subtransient part of the four firs half cycles of test #90

D.1.1 Envelope

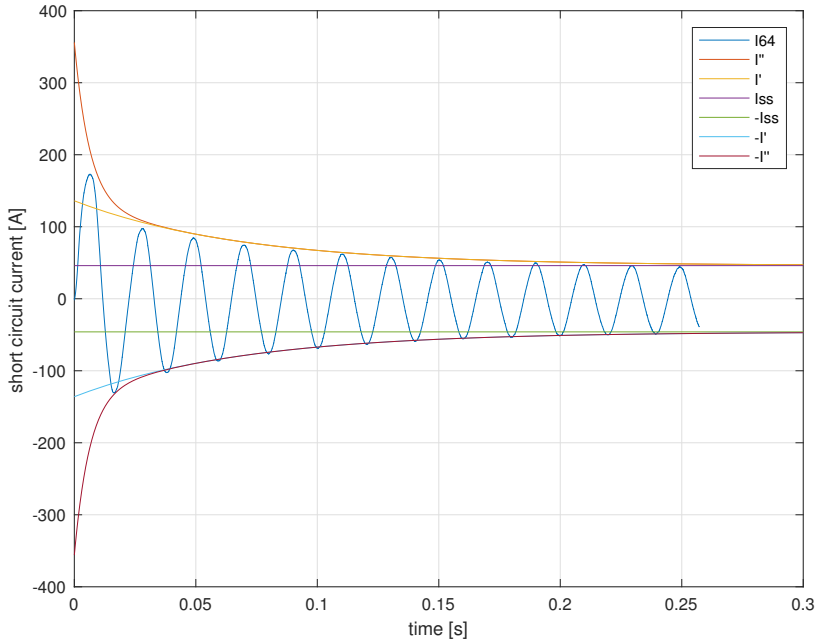

Figure D.5: Short circuit test $64 with the envelope found in chapter 3

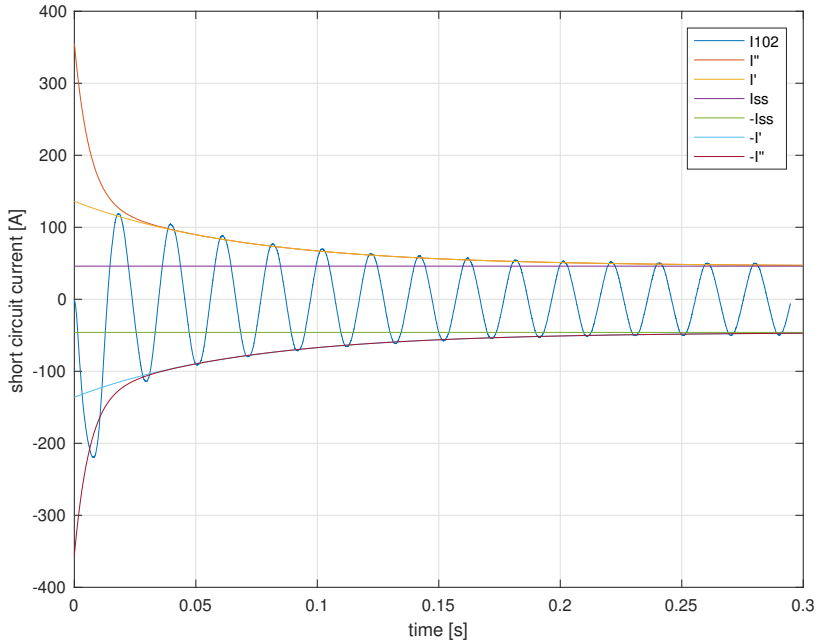

Figure D.6: Short circuit test $90 with the envelope found in chapter 3

D.2 Field current during short circuit

The field current during test #64 and #102 is shown in Figure D.7 and Figure D.8. According to expectations [7], both a DC and AC component is induced during the short circuit. The field current also apparently consists some ripple from the field excitation rectifier.

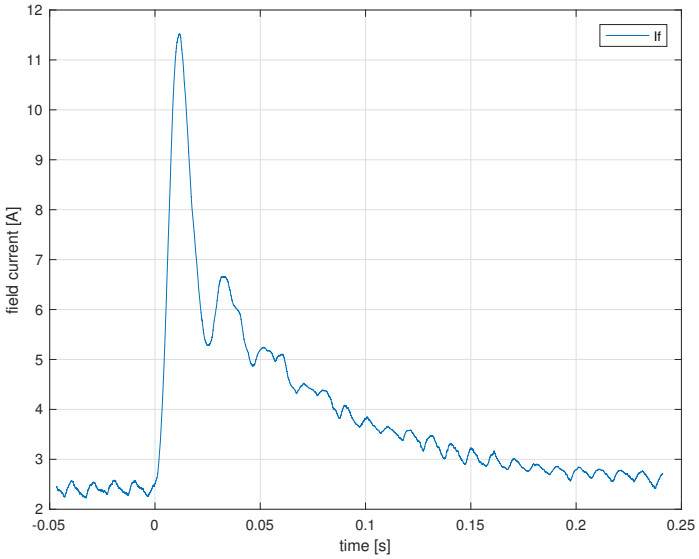

Figure D.7: Field current during short circuit test #64

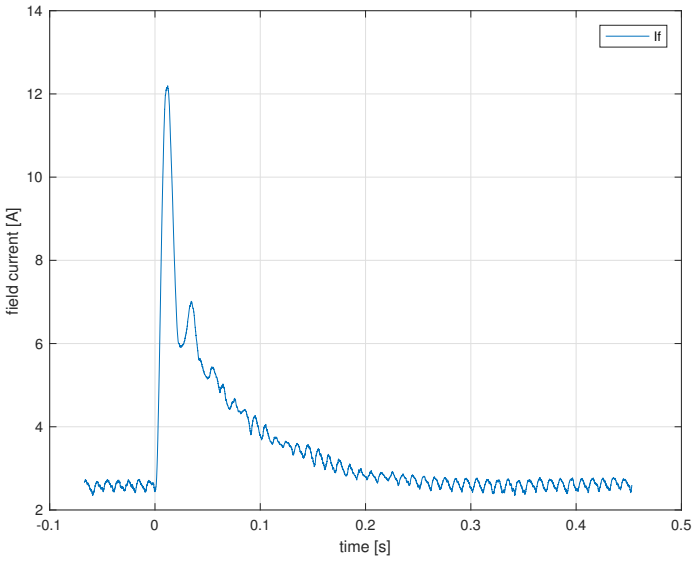

Figure D.8: Field current during short circuit test #102

Appendix E

Simulink model control system

E.1 Grid and machine side control system

Both for the machine and grid side, the positive current direction is defined to be in to the converter, from respectively the machine or the grid. This leads to opposite conventions in the inner control system, compared to the figures in chapter 5.

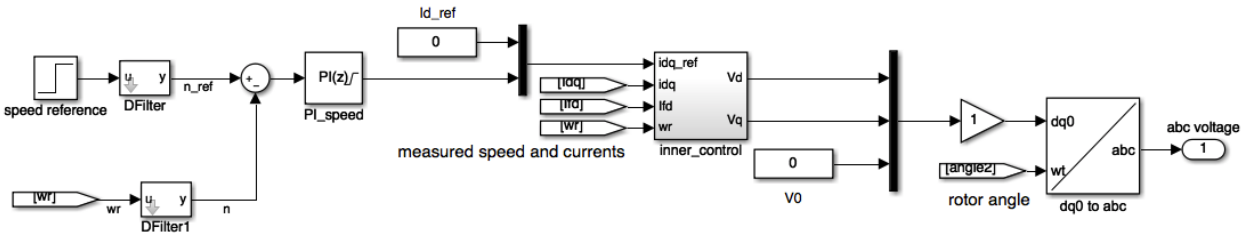

Figure E.1: Machine side speed control loop

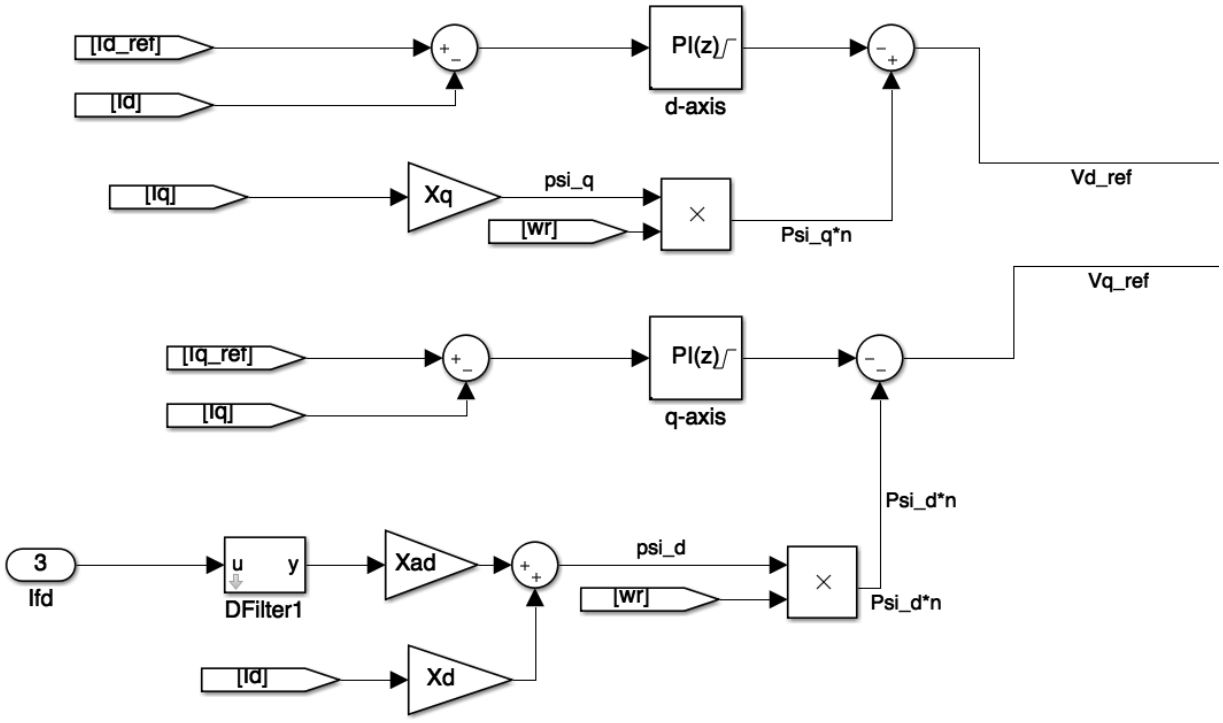

Figure E.2: Machine side inner control system

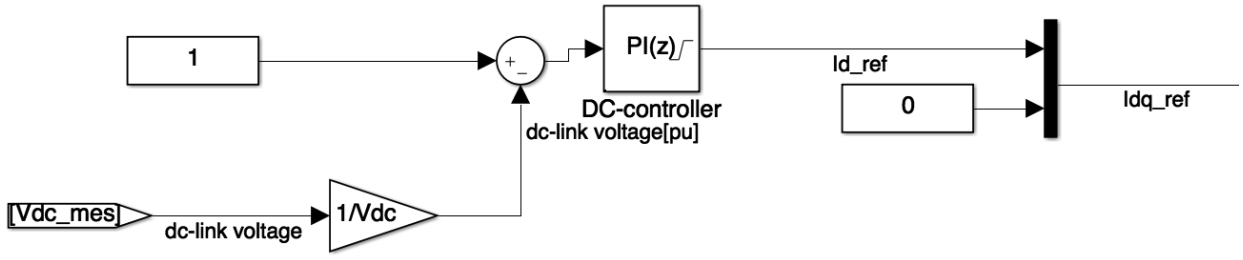

Figure E.3: GSC DC voltage control loop

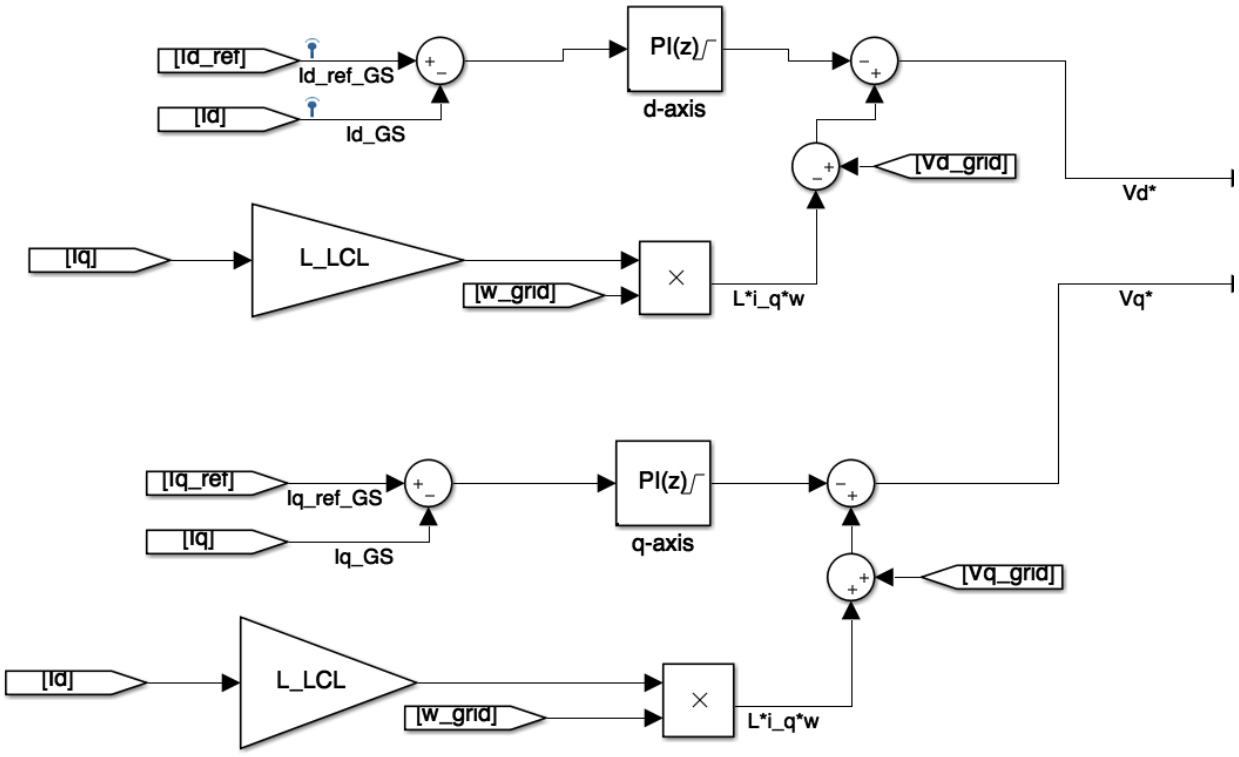

Figure E.4: GSC inner control system

E.2 Synthetic inertia

The derivative controller for synthetic inertia contribution is shown in Figure E.5. It is made by combining filters and a gain, which becomes the transfer function, as shown in (E.1).

$$K * \frac{1}{1+T_f s} * (1 + \frac{1}{1+T_f s}) = \frac{K * T_f}{(1+T_f s)^2} \tag{E.1}$$

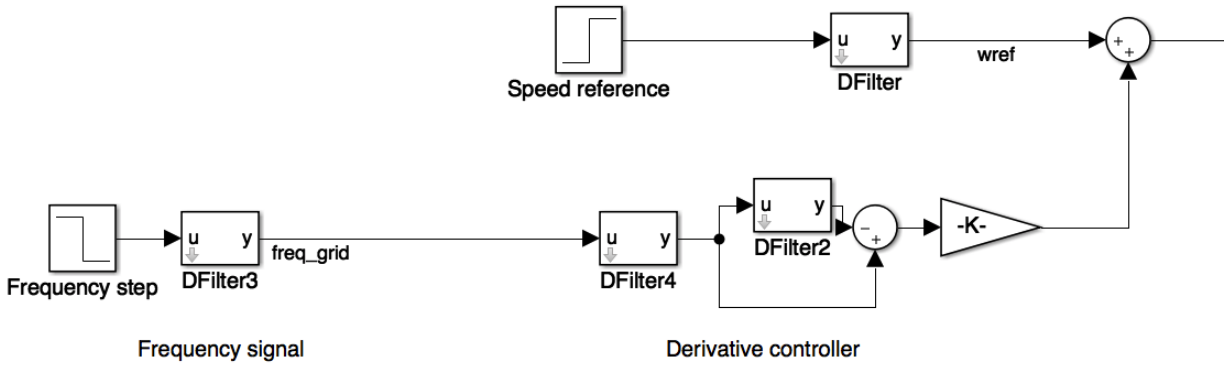

Figure E.5: Control loop for synthetic inertia contribution by influencing the speed reference

Appendix F

Additional simulation result

For all the simulations in this appendix, the mechanical load torque goes from 0 to 0.7 after 1s, the speed reference goes from 1 to 0.7 after 2s, filtered with a time constant of 100ms, the same way as done in section 6.3. The mechanical torque is applied in the rotating direction, so that the machine becomes a generator.

The controllers are tuned using the procedure described in chapter 6. For the simulations in the appendix, the synchronous machine is fed by a converter, which has a voltage source on the DC side, as shown below.

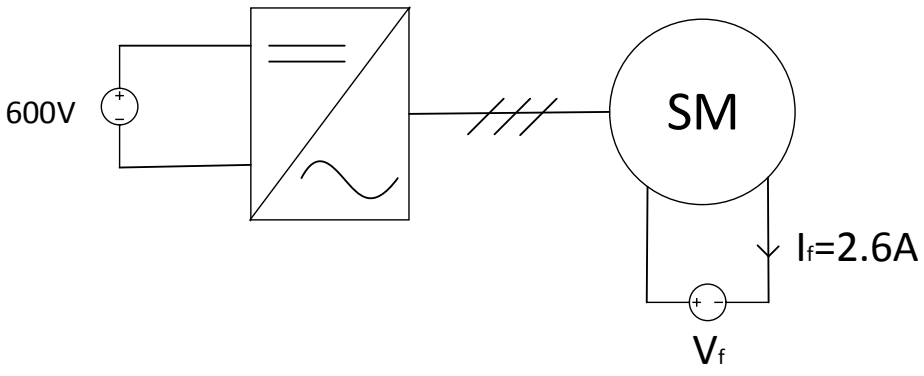

Figure F.1: CFSM with the DC link replaced by a DC source

F.1 Motor side converter including LCL filter

Simulation results where the converter is fed by a VSC, where the converter is fed by a DC source. The LCL filter is included in the model. I quite high filter time constant of 700μs had to be used, to keep the currents from oscillating too much.

The properties controller gains for the simulation is listed below:
System sampling time: $Ts = 2.5\mu s$
Current filter time constant: $T_{f,i} = 700\mu s$
Speed filter time constant: $T_{f,n} = 5ms$
Converter switching frequency: f_{sw} = 4kHz
d-axis current controller gain: $K_{p,d} = 0.32$
d-axis current controller integral gain: $K_{i,d} = 44.5$
q-axis current controller gain: $K_{p,q} = 0.40$
q-axis current controller integral gain: $K_{i,q} = 55.2$
Speed controller gain: $K_{p,n} = 53.3$
Speed controller integral gain: $K_{i,n} = 2004$
current controllers crossover frequency: $\omega_{c,i} = 427.9rad/s$
Speed controller crossover frequency: $\omega_{c,n} = 75.2rad/s$

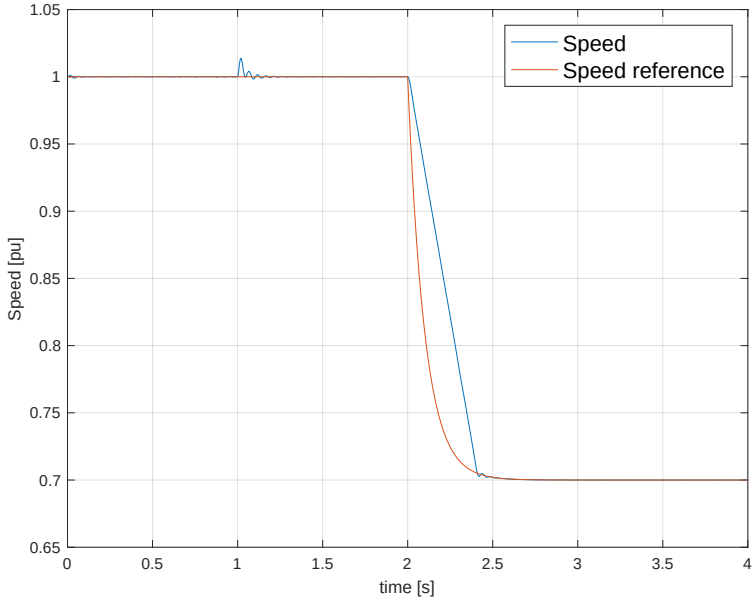

Figure F.2: Speed and speed reference

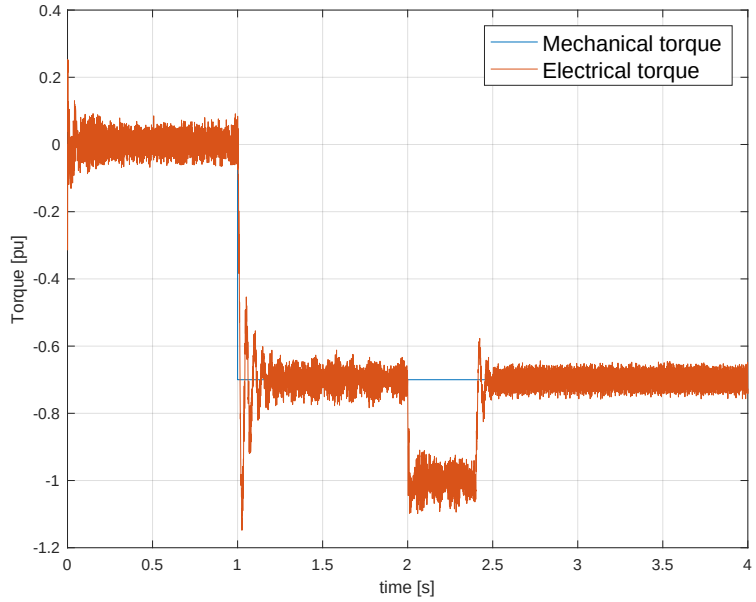

Figure F.3: Electrical and mechanical torque during a step in torque and speed

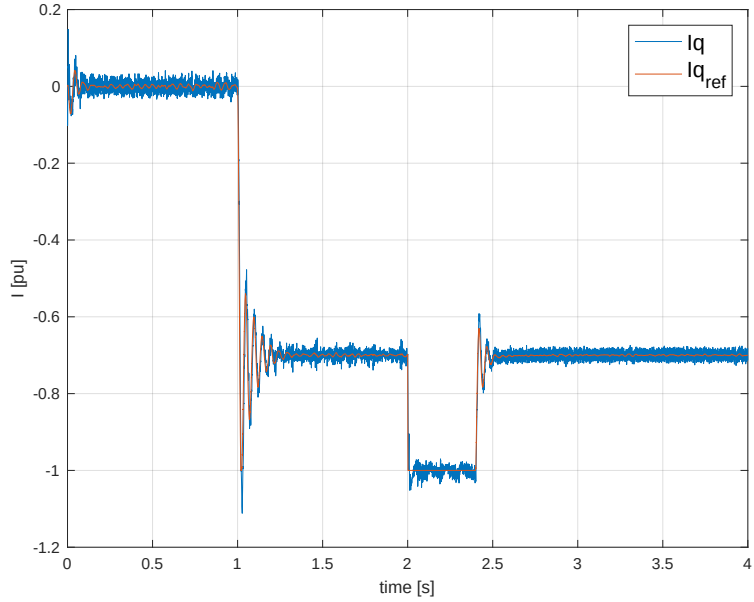

Figure F.4: q-axis current i_q

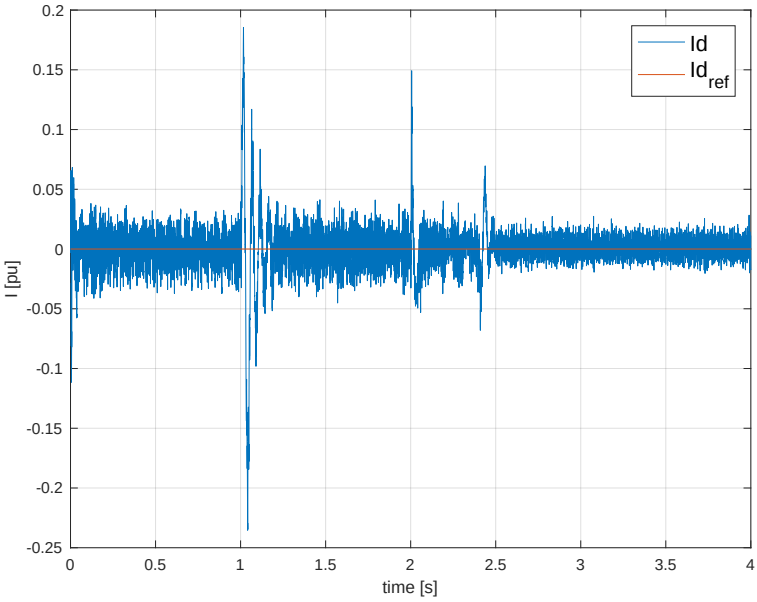

Figure F.5: d-axis current getting influenced by rappid changes in q-axis current

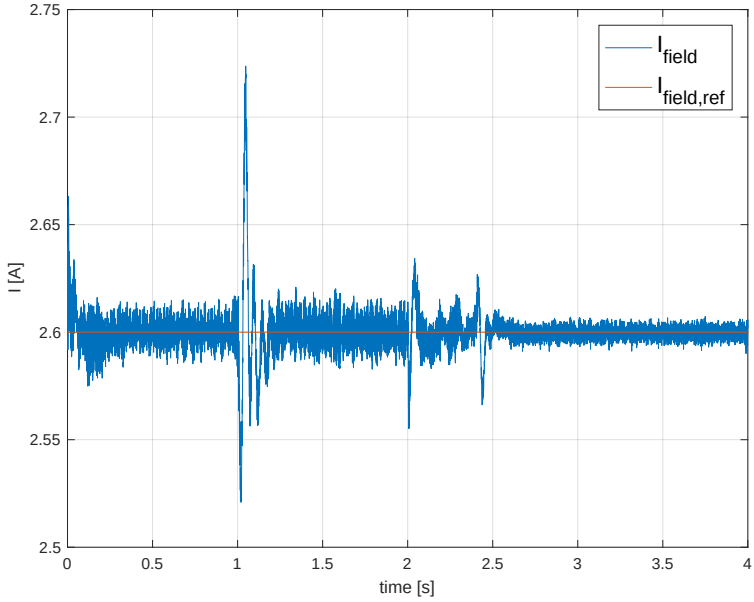

Figure F.6: d-axis current getting less influenced during the torque step

Motor side converter including LCL filter and synchronous sampling

Simulations with the same controller gains and simulation conditions as in the previous section, however with synchronous sampling implemented.

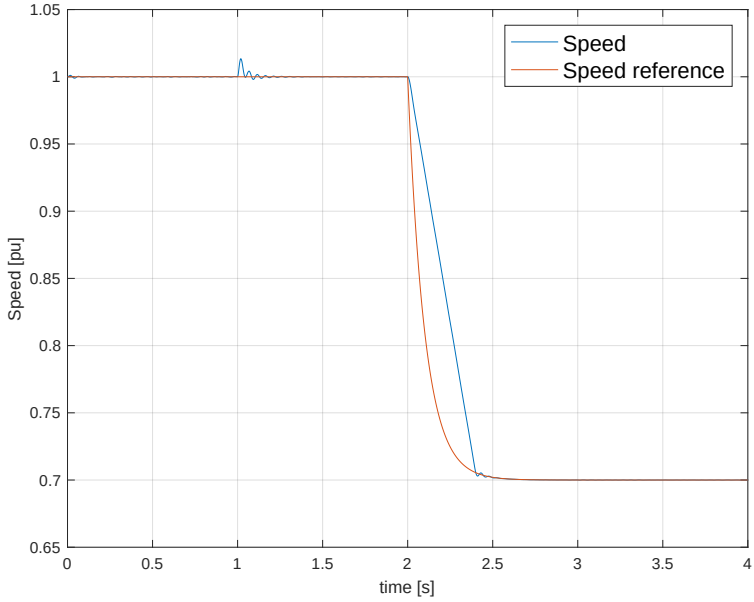

Figure F.7: Speed and speed reference

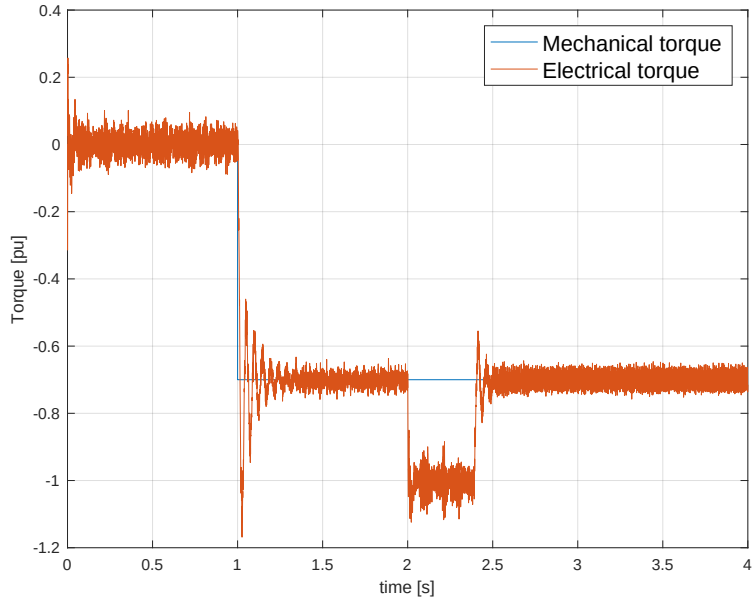

Figure F.8: Electrical and mechanical torque

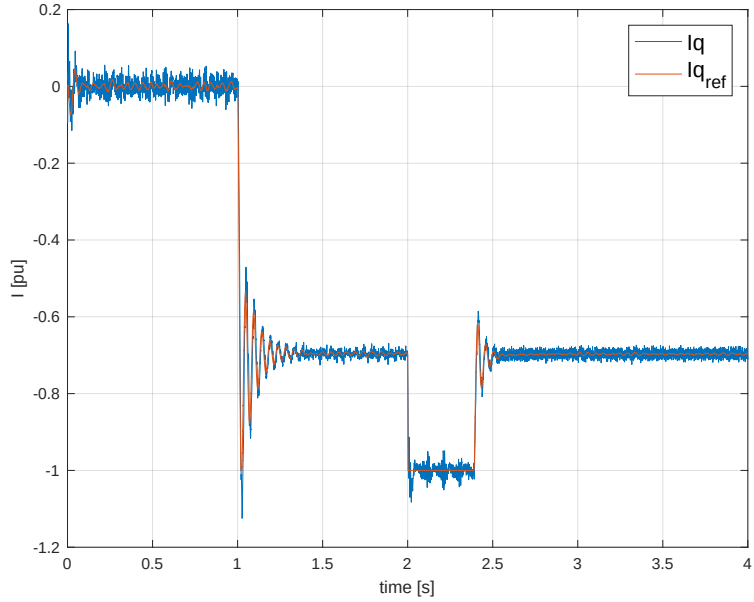

Figure F.9: q-axis current i_q and its reference

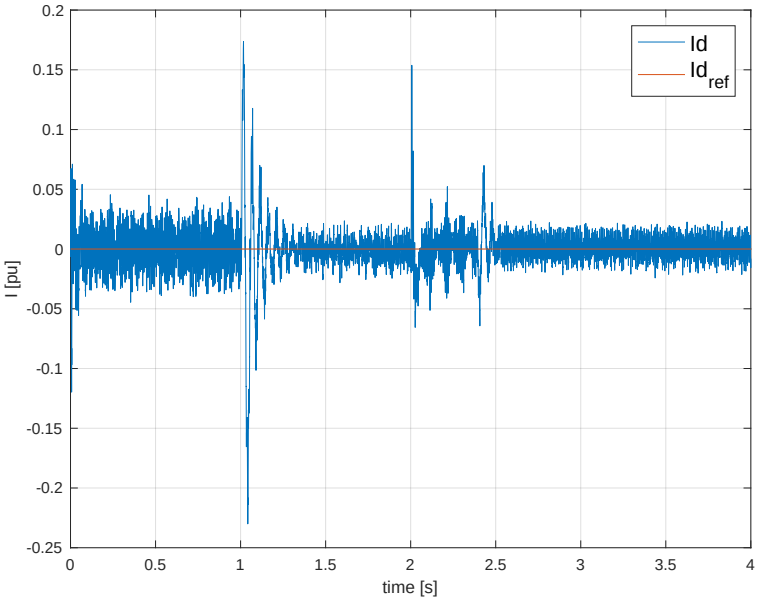

Figure F.10: d-axis current i_d and its reference

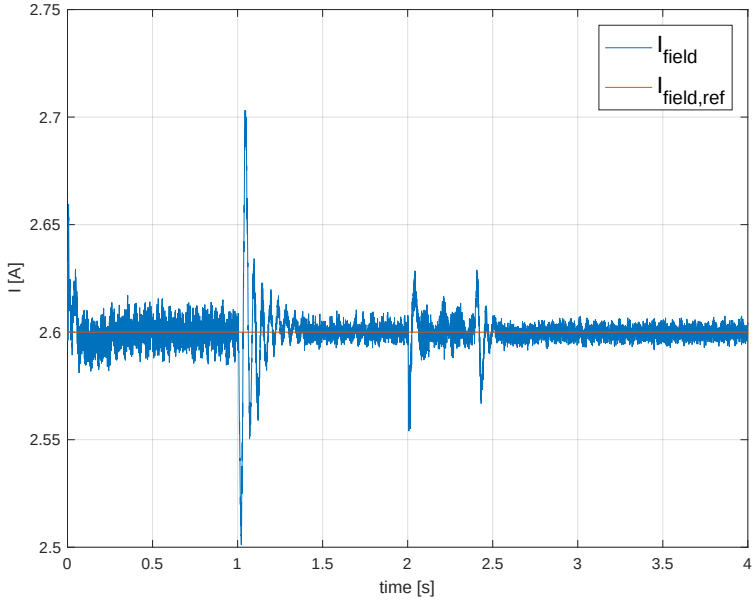

Figure F.11: Field curren I_f and its reference

F.2 Simulations without LCL filter

Simulation with the sampling of current each 2.5 μs, without the LCL filter between the converter and the machine.

Simulation properties and gains:

System sampling time: $Ts = 2.5\mu s$

Current filter time constant: $T_{f,i} = 300\mu s$

Speed filter time constant: $T_{f,n} = 5ms$

Converter switching frequency: $f_{sw} = 4$kHz

d-axis current controller gain: $K_{p,d} = 0.62$

d-axis current controller integral gain: $K_{i,d} = 86.3$

q-axis current controller gain: $K_{p,q} = 0.78$

q-axis current controller integral gain: $K_{i,q} = 101$

Speed controller gain: $K_{p,n} = 60.6$

Speed controller integral gain: $K_{i,n} = 2589$

current controllers crossover frequency: $\omega_{c,i} = 829 rad/s$

Speed controller crossover frequency: $\omega_{c,n} = 85.4 rad/s$

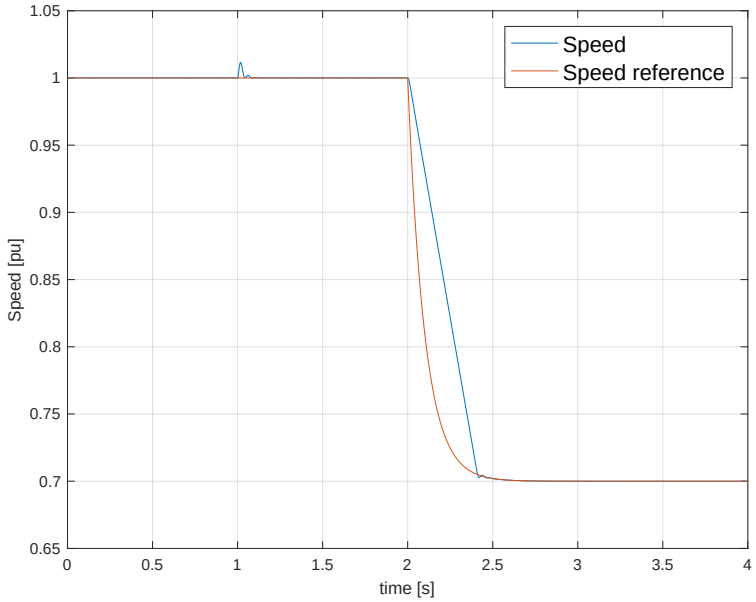

Figure F.12: Speed and speed reference

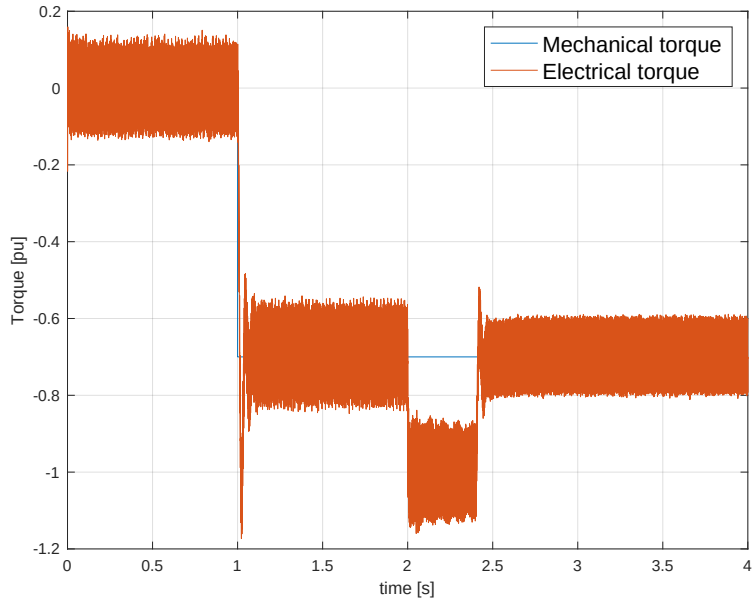

Figure F.13: Electrical and mechanical torque

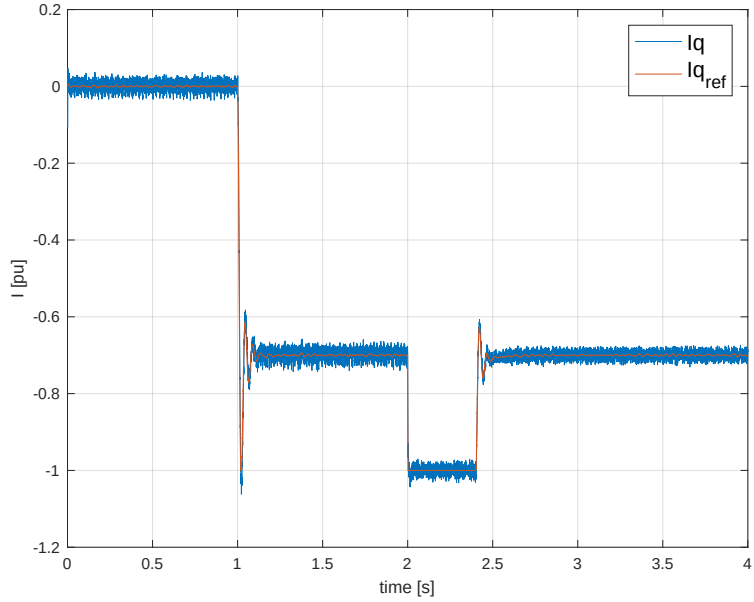

Figure F.14: q-axis current i_q and its reference

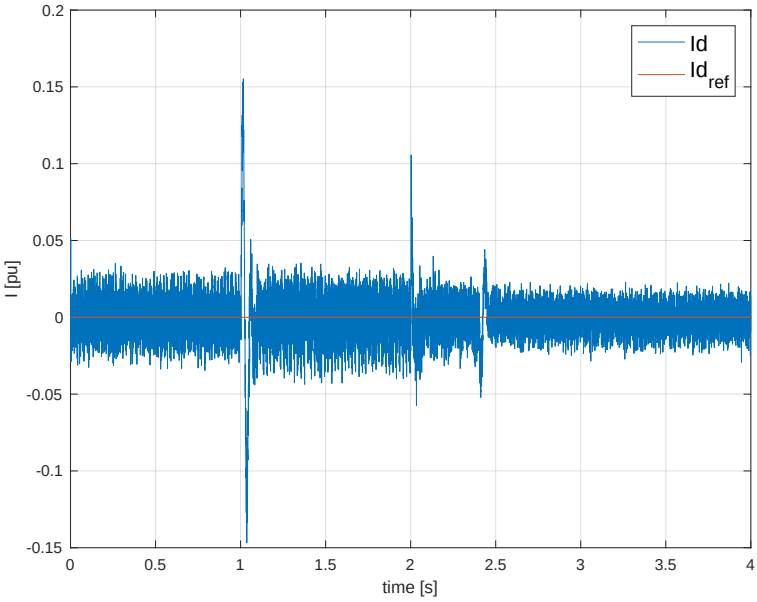

Figure F.15: d-axis current i_d and its reference

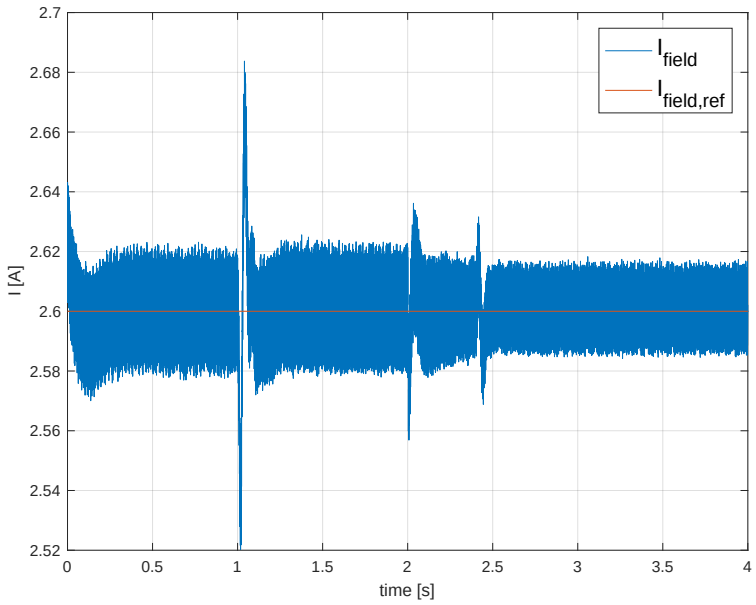

Figure F.16: Field curren I_f and its reference

F.3 Simulations with synchronous sampling and without LCL filter

F.3.1 Synchronous sampling without the LCL filter

In this simulation, the filtering time constant is as in the prior section, but with synchronous sampling implemented.

Simulation properties and gains:

System sampling time: $Ts = 2.5\mu s$

Current filter time constant: $T_{f,i} = 300\mu s$

Speed filter time constant: $T_{f,n} = 5ms$

Converter switching frequency: $f_{sw} = 4$kHz

d-axis current controller gain: $K_{p,d} = 0.62$

d-axis current controller integral gain: $K_{i,d} = 86.3$

q-axis current controller gain: $K_{p,q} = 0.78$

q-axis current controller integral gain: $K_{i,q} = 101$

Speed controller gain: $K_{p,n} = 60.6$

Speed controller integral gain: $K_{i,n} = 2589$

current controllers crossover frequency: $\omega_{c,i} = 829 rad/s$

Speed controller crossover frequency: $\omega_{c,n} = 85.4 rad/s$

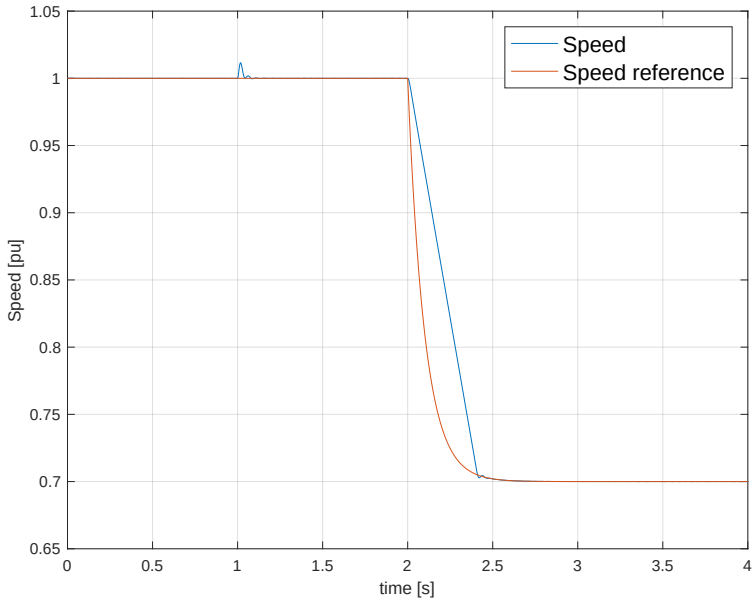

Figure F.17: Speed and speed reference

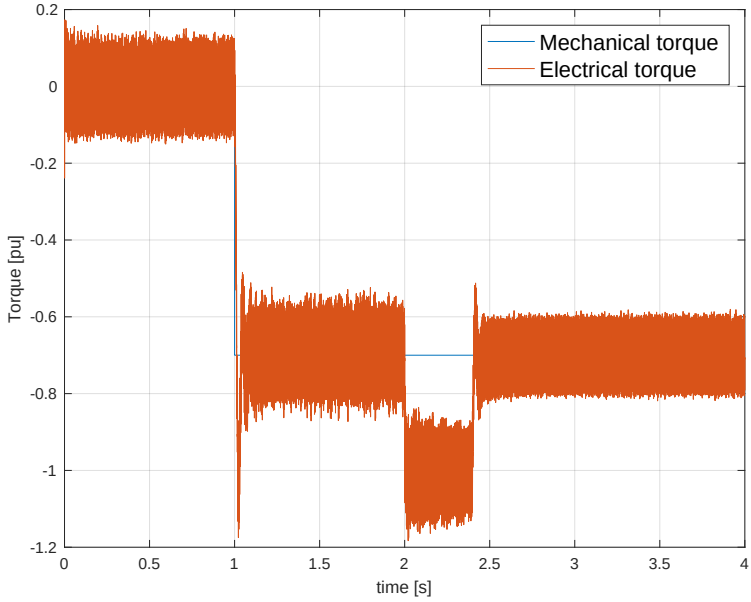

Figure F.18: Electrical and mechanical torque

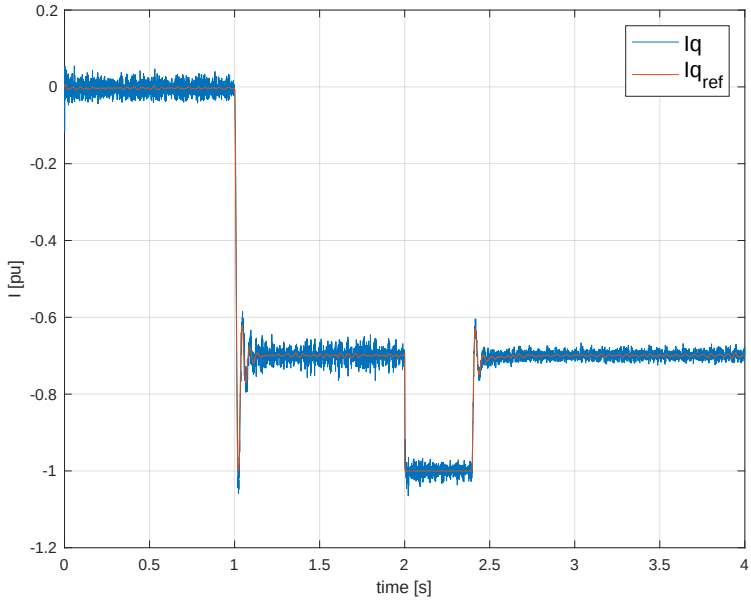

Figure F.19: q-axis current i_q and its reference

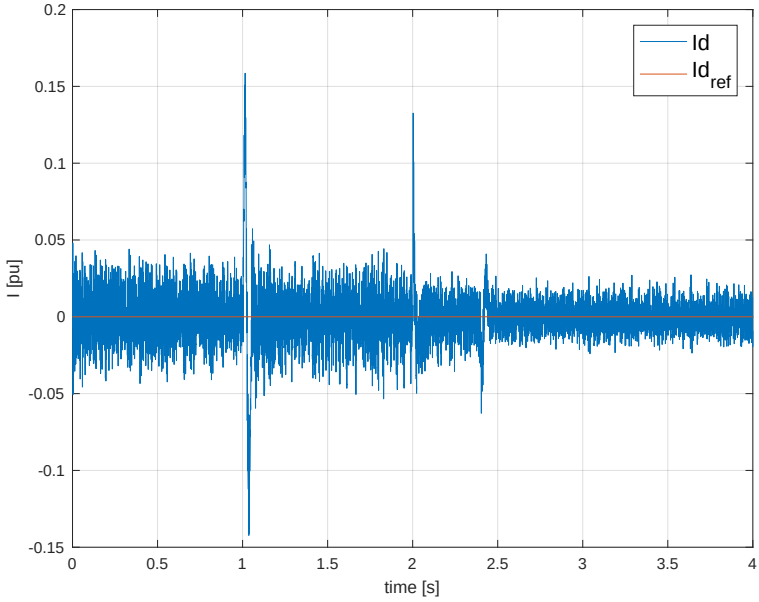

Figure F.20: d-axis current i_d and its reference

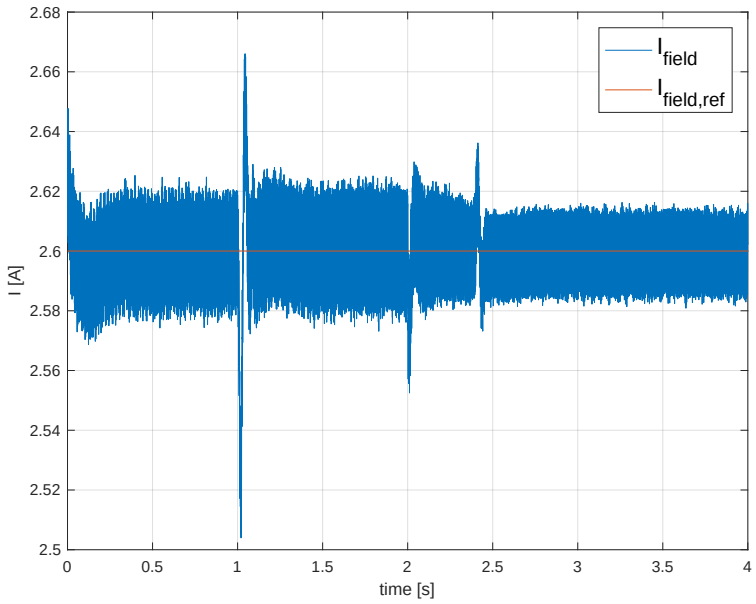

Figure F.21: Field curren I_f and its reference

F.3.2 Simulation with a lower $T_{f,i}$

One of the main advantages of implementing synchronous sampling is to be able to choose a lower filtering time constant for the current measurements, so that the inner system becomes faster. The filtering time constant is here set to $T_{fi} = 100\mu s$.

Simulation properties and gains:
System sampling time: $Ts = 2.5\mu s$
Current filter time constant: $T_{f,i} = 100\mu s$
Speed filter time constant: $T_{f,n} = 5ms$
Converter switching frequency: $f_{sw} = 4$kHz
d-axis current controller gain: $K_{p,d} = 1.16$
d-axis current controller integral gain: $K_{i,d} = 162.6$
q-axis current controller gain: $K_{p,q} = 1.46$
q-axis current controller integral gain: $K_{i,q} = 190.5$
Speed controller gain: $K_{p,n} = 65.1$
Speed controller integral gain: $K_{i,n} = 2983$
current controllers crossover frequency: $\omega_{c,i} = 1563 rad/s$
Speed controller crossover frequency: $\omega_{c,n} = 91.7 rad/s$

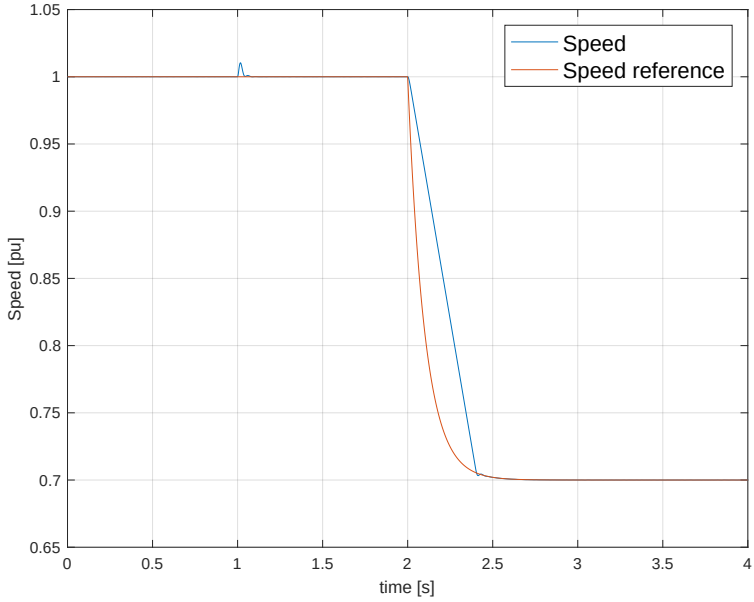

Figure F.22: Speed and speed reference

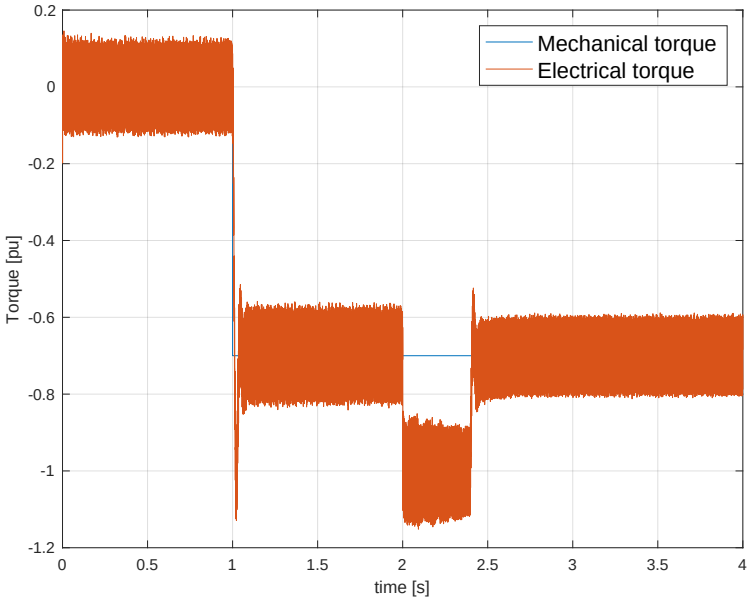

Figure F.23: Electrical and mechanical torque

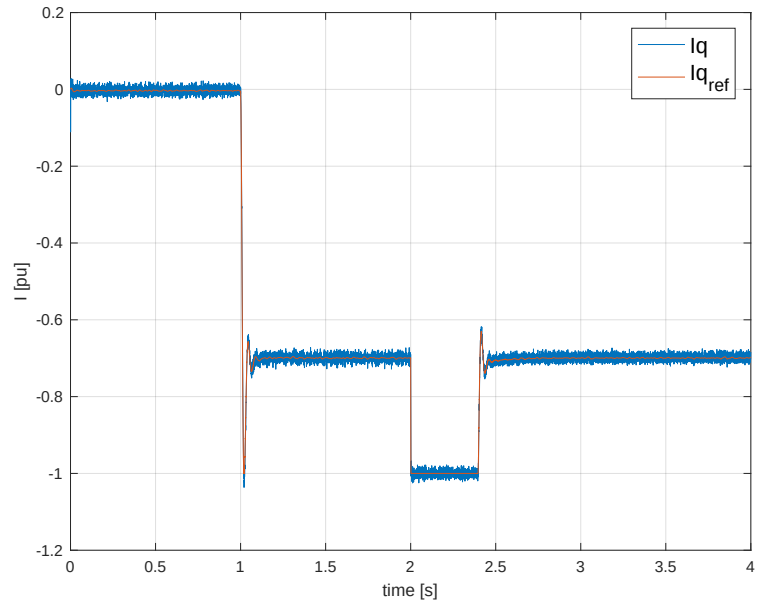

Figure F.24: q-axis current i_q and its reference

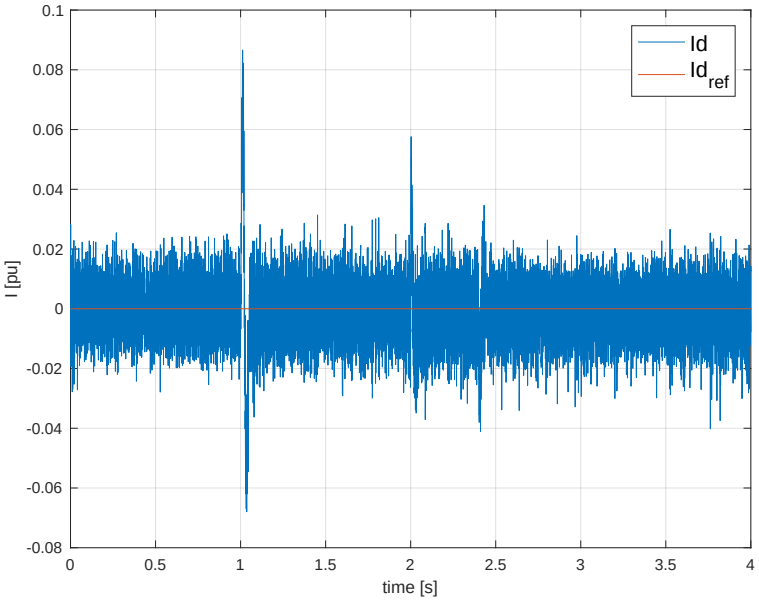

Figure F.25: d-axis current i_d and its reference

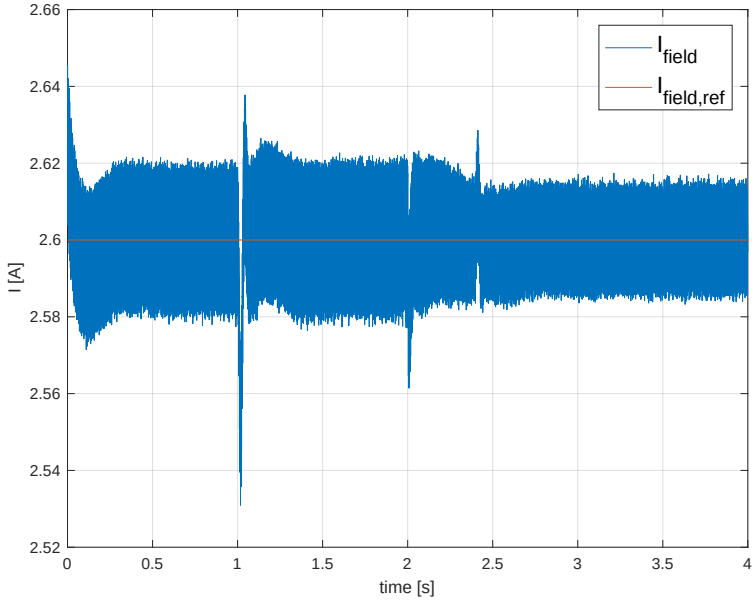

Figure F.26: Field curren I_f and its reference